



# Interactions are important: Linking multiphysics mechanisms to the performance and degradation of solid-state batteries

Mei-Chin Pang <sup>1,1</sup>, Kai Yang <sup>2,1</sup>, Rowena Brugge <sup>3</sup>, Teng Zhang <sup>4</sup>, Xinhua Liu <sup>5,6</sup>,\*, Feng Pan <sup>2</sup>, Shichun Yang <sup>5</sup>, Ainara Aguadero <sup>3</sup>, Billy Wu <sup>6</sup>, Monica Marinescu <sup>1</sup>, Huizhi Wang <sup>1</sup>, Gregory J. Offer <sup>1</sup>

The behaviour of solid-state batteries to many application-relevant operating conditions is intrinsically multiphysical and multiscale, involving the electrochemical performance and chemical stability coupled with the thermal and mechanical properties of multiple components. This review presents a holistic approach to discussing the multiscale physical-electro-chemical interactions and degradation mechanisms in solid-state batteries. While the propagation of lithium filaments depends strongly on the critical current densities, we show that effective prevention of excessive Li plating and stripping requires a combined understanding of solid-state electrochemistry, microstructure, mechanics, operating conditions, and their interactions. A review of how multiphysical interactions affect the optimum design of thin-film, three-dimensional and composite solid-state cell architectures is also included. Although the use of lithium metal as negative electrodes could improve the energy densities of solid-state batteries, we show that its high homologous temperature could cause cell failure during manufacturing. By comparing published model predictions with experimental observations, we present a critical analysis of the strengths and limitations of state-of-the-art models and characterisation techniques in solid-state battery research. This comprehensive mechanistic analysis provides an insight into the interplay among the multiple complex multiphysical mechanisms, shedding light on the process of cell design for next-generation solid-state batteries.

Keywords: Solid-state battery; Interaction; Multi-physics mechanisms; Simulation; Characterization

## 1. Introduction

Solid-state batteries show potential to replace conventional Liion batteries based on liquid, or liquid aprotic electrolytes due

to their lower risk of flammability [1,2]. While it is difficult to employ Li metal in conventional liquid-based batteries due to a higher risk of internal short-circuit [3], replacing the liquid electrolyte with a Solid Electrolyte (SE) could enable the use of Li metal in next-generation batteries. Li metal has a higher gravimetric and volumetric capacity (e.g., 3860 mAh g $^{-1}$  and 2060 mAh cm $^{-3}$ ) compared to graphite (372 mAh g $^{-1}$  and 837 mAh cm $^{-3}$ ) [4]. As a result, replacing graphite and liquid

<sup>&</sup>lt;sup>1</sup> Department of Mechanical Engineering, Imperial College London, Exhibition Road, South Kensington Campus, London, United Kingdom

<sup>&</sup>lt;sup>2</sup> School of Advanced Materials, Peking University, Shenzhen Graduate School, United Kingdom

<sup>&</sup>lt;sup>3</sup> Department of Materials, Imperial College London, Exhibition Road, South Kensington Campus, London, United Kingdom

<sup>&</sup>lt;sup>4</sup> Department of Mechanical Engineering Sciences, University of Surrey, Guildford, Surrey, United Kingdom

<sup>&</sup>lt;sup>5</sup> School of Transportation Science and Engineering, Beihang University, 100191 Beijing, China

<sup>&</sup>lt;sup>6</sup> Dyson School of Engineering, Imperial College London, Exhibition Road, South Kensington Campus, London, China

<sup>\*</sup> Corresponding author.

E-mail addresses: Liu, X. (liuxinhua19@buaa.edu.cn), Offer, G.J. (gregory.offer@imperial.ac.

<sup>&</sup>lt;sup>1</sup> These authors contributed equally to the analysis of the literature and writing of this manuscript.

#### **Nomenclature** Greek Symbols $Q_{conv}$ Heat dissipation by convection (W) Interfacial potential drop (V) Heat dissipation by radiation (W) $\Delta \phi$ $Q_{\text{rad}}$ Critical pressure (kPa) In-plane/cross-plane thermal conductivity $(W m^{-1} \Delta p_c$ $k_{x/y/z}$ $K^{-1}$ Critical pressure (kPa) $\Delta p_c$ $C_{p}$ Specific heat capacity at constant pressure $\Delta V$ Potential difference (V) Effective thermal conductivity $(W m^{-1} K^{-1})$ Oxidation/reduction charge transfer coefficient $k_{\rm eff}$ (-) $\alpha_{ox/red}$ Thermal expansion coefficient Ē. Young's modulus (GPa) $\Delta x/y/z$ Change in lengths G Shear modulus (GPa) Strain K Bulk modulus (GPa) (-)permittivity Absolute the vacuum $H_{x}$ Hardness (GPa) $(\epsilon_0 = 8.85 \times 10^{-12} \,\mathrm{F m^{-1}})$ $P_{v}$ Indentation force (N) Relative permittivity Indentation length $a_{v}$ $\epsilon_{r}$ Thermal strain Crack length (nm) $\epsilon_{\mathrm{T}}$ $C_{xy}$ $\eta^{ct}$ Charge-transfer overpotential $(MPa m^{1/2})$ (V) Fracture toughness $K_{c}$ $\eta^{\text{diff}}$ Diffusion overpotential Flaw size $a_{\rm c}$ (um) $\eta^{\mathrm{mt}}$ Mass-transport overpotential Transference number (-) $I^0$ Geometric factor of the surface crack shape Initial current γ Is Debye length Steady-state currents (nm) (mA) $R_1^0$ Poisson's ratio Initial resistance $(\Omega)$ (-)(V) $R_1^{\bar{s}}$ φ Electric potential Steady-state resistance $(kg m^{-3})$ Material density Exchange current densities $(mA cm^{-2})$ $i_{0,\text{neg/pos}}$ $(S cm^{-1})$ $(mol \ m^{-2} \ s^{-1})$ Electrolyte conductivity Oxidation or reduction rate-constant $\sigma_{ m elec}$ $k_{\rm ox/red}$ $(N m^{-2})$ $(mol \ m^{-3})$ Concentration of mobile cations Stress $\sigma_{ m st}$ $c_{+}$ Electronic conductivity $(S \text{ cm}^{-1})$ Flux $(\text{mol } \text{m}^{-2} \text{ s}^{-1})$ $\sigma_{\mathrm{e}}$ Volume strain $i_{ct}$ Faradaic current due to charge-transfers at the interfaces $(mA cm^{-2})$ Double layers current $(mA cm^{-2})$ $i_{ m DL}$ Lattin Symbols $(mA cm^{-2})$ Interfacial current Interfacial characteristic frequency $i_{ m int}$ $f_{\rm int}$ IJ Open-circuit Potential Interfacial capacitance $(\mu F \text{ cm}^{-2})$ $C_{\rm int}$ $(\Omega \ cm^{-2})$ V Cell voltage (V) Interfacial areal resistance $R_{\rm int}$ $(A m^{-2})$ $A_{\rm f}$ Footprint area of the cell on the substrate $(cm^2)$ Critical current density True internal surface area $(cm^2)$ Q Charge of the bodies $A_{\rm int}$ $d_{\mathrm{elec}}$ Electrolyte thickness $(\mu m)$ $F_{c}$ Coulombic force $A_{\text{elec}}$ Active surface area $(cm^2)$ Distance between the center of the charges $d_{int}$ (nm) $(\Omega \text{ cm}^2)$ $R_{\rm elec}$ Electrolyte resistance Number of proton charges Residual current (mA) $I_{\rm res}$ T **Temperature** Total mass of a cell Universal gas constant ( $R_{gas} = 8.314 \,\mathrm{J \, mol^{-1} \, K^{-1}}$ ) $m_{\rm cell}$ $R_{\rm gas}$ Total thickness of a cell (µm) $l_{\rm cell}$ Faraday's constant ( $F = 96485 \text{ C mol}^{-1}$ ) $x_0/y_0/z_0$ Original lengths $(\text{mol m}^{-3})$ Bulk concentration of the species $c_{\text{bulk}}$ Heat generation (W) $Q_{\text{gen}}$

electrolytes with Li metal and SE could potentially increase the gravimetric density by 40% and volumetric density by 70% [5].

Many signs of progress have been achieved in this field to improve the ionic conductivity of the SE [6–8], reducing the interfacial impedance by the use of coatings [9,10] and suppressing the Li filamentary growth [11–14]. Despite these advances, there is a lack of holistic understanding of the underlying interactions between different multiphysical mechanisms. A real solid-state cell has multiple components. The operations of solid-state batteries are inherently multiphysical and multiscale, involving different electrochemical and chemical reactions coupled with unique thermal and mechanical behaviour. Little attention has been given to discussing how the interplay of these mechanisms affects the overall cell performance and degradation behaviours under different operating conditions.

Different works focusing on sulfide-based SEs have been reported due to their high ionic conductivity [26–30]. Whilst sulfide-based SEs have the highest ionic conductivity compared to other SEs, this class of SE also has other significant drawbacks

such as the generation of toxic H<sub>2</sub>S gas upon exposure to moisture and a higher risk of cell failure due to Li filaments propagation. A comparative analysis in terms of quantitative multiphysical properties between different classes of SEs and cell components has not been discussed in the literature. In the case of cell failure such as excessive Li plating and stripping, the nucleation and propagation of Li filament in solid-state batteries depends strongly on the Critical Current Density (CCD). However, the CCD is also a function of operating temperatures and critical pressures [11,31–33]. Therefore, effective prevention of excessive Li plating and stripping requires a combined understanding of solid-state electrochemistry, microstructure, mechanics, operating conditions, and their interactions.

This review's main objective is to critically analyse the underlying multiphysical mechanisms governing the performance and degradation behaviour of solid-state batteries under different operating conditions. By reviewing the recent progress from experimental and computational studies of solid-state battery

electrochemistry, we aim to address the following questions and their implications for determining future research directions:

- 1. What are the impacts of electrochemical, chemical, thermal and mechanical properties of different inorganic SEs on the performance of solid-state batteries? How do the properties of other cell components such as electrodes, additives and current collectors influence the overall cell behaviour?
- 2. Which degradation mechanisms are dominant in solid-state batteries? What are the impacts of different operating conditions on the failure modes of solid-state batteries?
- 3. How do solid-state physical properties such as the low melting temperature of Li metal or phase change and Li-ion diffusion in the non-porous Positive Electrode (PE) affect the engineering of different solid-state cell architectures?

As shown by Fig. 1, we primarily focus on the multiphysical interactions between different mechanisms governing the overall performance of solid-state batteries. We explore and discuss these interactions *via* an array of modelling and characterisation techniques. Although interfacial stabilities play an essential role in determining the cell performance, we highlight the importance of a holistic mechanistic review of different cell components and their multiphysical interactions. A comprehensive summary of different degradation mechanisms will be especially useful for the future development of smart sensors for solid-state

batteries, where the mechanistic understanding of different degradations and their trigger conditions is critical to detect potential fault behaviours before a complete failure. In this work, we discuss individual aspects of cell performance such as the interfacial phenomena in brief as these topics are covered in details by Cheng et al. [35], Famprikis et al. [36], Banerjee et al. [37] and Xiao et al. [38].

## 2. Multiphysical properties of solid-state cells

The behaviour of solid-state batteries under a wide range of conditions is inherently multiphysical, involving electrochemical and chemical reactions as well as thermal and mechanical responses. Han et al. have compared the properties for three representative classes of inorganic SEs (Lithium Phosphorus OxyNitride (LiPON), Li $_7$ La $_3$ Zr $_2$ O $_{12}$  (LLZO) and Li $_2$ S-P $_2$ S $_5$  (LPS)) [12]. Their works are extended in this review to consider the multiphysical properties of inorganic SEs and interactions between different cell components, in order to illustrate the complex interplay between electrochemical, chemical, thermal and mechanical mechanisms.

## 2.1. Electrochemical and chemical properties

**Ionic and electronic conductivity.** An ideal SE should have a high ionic conductivity ( $> 10^{-3} \text{ S cm}^{-1}$ ) and a low electronic conductivity ( $< 10^{-9} \text{ S cm}^{-1}$ ) [7,12,34]. Compared to the

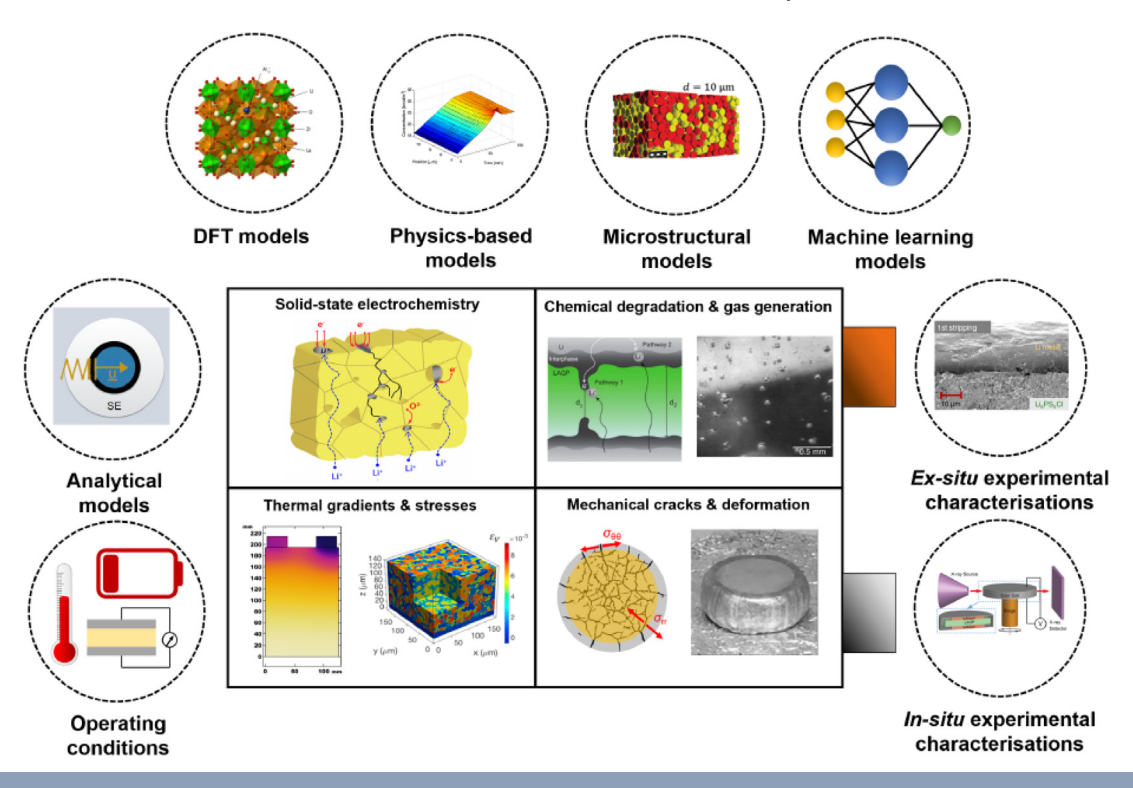


#### FIGURE 1

Schematic illustration of the multiphysical interactions between electrochemical (Reprinted with permission from Ref. [15]), chemical (Reprinted with permission from Ref. [16] and Ref. [17]), thermal (Reprinted with permission from Ref. [18] and Ref. [19]) and mechanisms (Reprinted with permission from Ref. [20] and Ref. [21]), and the effects of operating conditions on these mechanisms. Here, we present a combined review of state-of-the-art modelling approaches and experimental characterisation techniques. The modelling techniques include analytical models (Reprinted with permission from Ref. [22]), Density Functional Theory (DFT) models (Reprinted with permission from Ref. [23]), physics-based models (Reprinted with permission from Ref. [24]), microstructural models (Reprinted with permission from Ref. [25]) and machine learning models. The right panel illustrates state-of-the-art characterisation categories reviewed in this work to understand the multiphysical interacting mechanisms in solid-state batteries (Reprinted with permission from Ref. [13] and Ref. [20]).

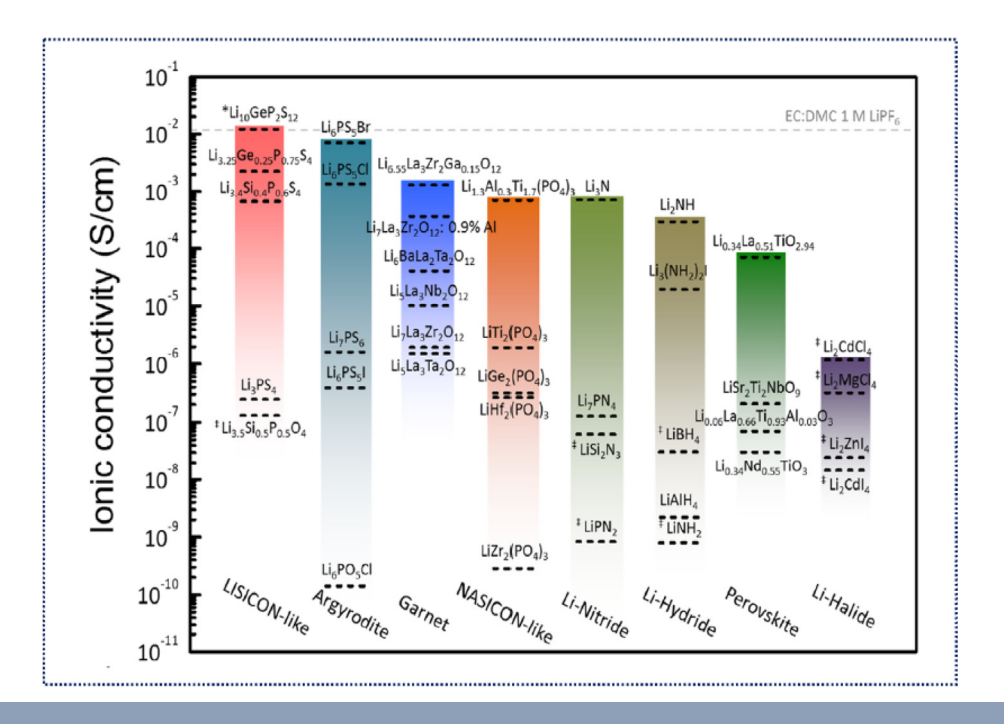


FIGURE 2

A comparison of total ionic conductivity for different classes of inorganic solid electrolytes such as LISICON, argyrodite, garnet, NASICON, Li-Nitride, Li-Hydride, perovskite and Li-halide. Reprinted with permission from Ref. [34], Copyright (2016), American Chemical Society.

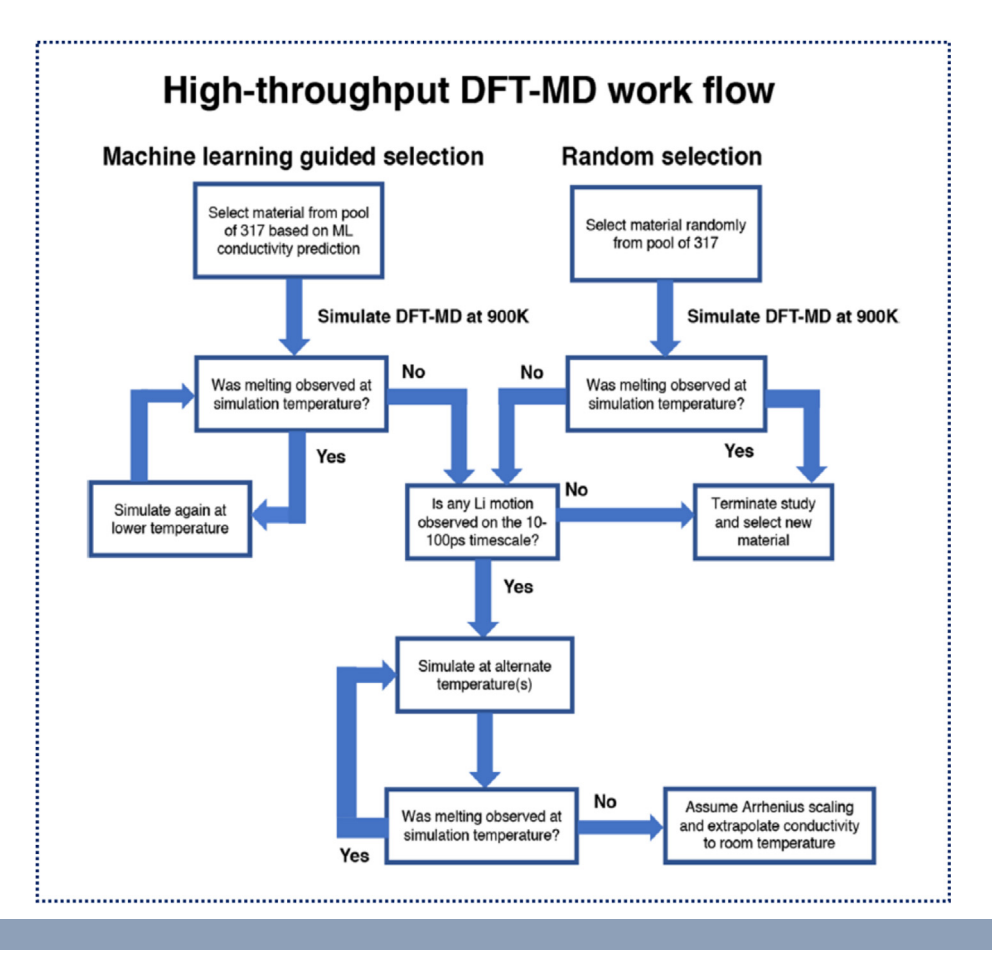
area specific impedance of liquid electrolytes (in the range of  $m\Omega \text{ cm}^2 - \Omega \text{ cm}^2$ ) [40–43], inorganic SEs usually have an impedance several orders of magnitude higher ( $\gg 200 \,\Omega\,\text{cm}^2$ ) due to the low electrolyte conductivity [6,7,32,44–46]. The resistance of grain boundaries is often cited as a major reason causing the low ionic conductivity in inorganic SEs [7,34]. Various research efforts have been dedicated to reducing the electrolyte resistance via optimising the processing conditions, doping, reducing the electrolyte thickness and increasing the operating temperatures [6-8,46-48]. Among all the representative classes of inorganic SEs reviewed in this work, sulfide-based SEs have the highest ionic conductivity  $(10^{-3} - 10^{-2} \,\mathrm{S\,cm^{-1}})$  comparable to that of the liquid electrolyte such as Ethylene Carbonate/DiMethyl Carbonate (EC/DMC) 1 M LiPF<sub>6</sub> (10<sup>-2</sup> S cm<sup>-1</sup>), as shown by Fig. 2 [34]. However, their stability against Li and PE is a challenge and limits their lifetime.

The experimental trial-and-error searches for promising new materials that satisfy a high-performance SE requirements are time and cost-consuming. Sendek et al. [49] have developed a data-driven ionic conductivity classification model using logistic regression machine learning algorithms to distinguish between potential solid electrolytes with superionic structures  $(\sigma_{\rm elec} \ge 10^{-4} \, {\rm S \, cm^{-1}})$ and non-superionic structures  $(\sigma_{\rm elec} < 10^{-4} \, {\rm S \, cm^{-1}})$ . They further performed Density Functional Theory (DFT)-Molecular Dynamics (MD) simulations on the most promising materials screened by the machine learning models to study the structure-property relationships of these superionic solids [39]. Fig. 3 illustrates the workflow of a combined machine learning and DFT-MD approaches.

Compared to the progress achieved in improving ionic conductivity, the study of the role of the electronic conductivity of inorganic SEs is often overlooked. Recently, Han and co-

workers [12] demonstrated the critical role of the electronic conductivity in determining the growth of Li filaments. In general, the term "Li dendrite" loosely describes "the formation of a wide range of nonplanar/branched metal morphologies and may not accurately describe the complex mechanisms involved in SEs."[50] For this reason, the term Li filament is used throughout this review to describe these Li metal features. The current-time behaviour, from a potentiostatic hold, of Cu-LLZO-Cu and Cu-Li<sub>3</sub>PS<sub>4</sub>--Cu cells were measured and both SEs shown to have electronic conductivities of  $5.5 \times 10^{-8} \, \text{S cm}^{-1}$  and  $2.2 \times 10^{-9} \, \text{S cm}^{-1}$  respectively, which is much higher than the electronic conductivity of LiPON (10<sup>-14</sup> S cm<sup>-1</sup>) [12,48]. By correlating the electronic conductivity to the time-resolved Li concentration profiles of Li<sub>3</sub>PS<sub>4</sub>, LLZO and LiPON measured using operando Neutron Depth Profiling (NDP), they concluded that the high electronic conductivity of LLZO and Li<sub>3</sub>PS<sub>4</sub> was the reason for promoting the formation of Li filaments within the SE. A high electronic conductivity lowers the critical overpotential of the SE and causes the reduction of Li<sup>+</sup> into Li within the bulk SE [12].

**Critical Current Density (CCD).** CCD can be defined as the current density, at which Li filaments propagate through the SE to cause an internal short-circuit and an immediate voltage drop [11]. The CCD could be further distinguished as the critical current for stripping and the critical current for plating. The stripping critical current denotes "the current density, above which Li is stripped faster than it is replenished at the Li/SE interface, resulting in void formation."[13] The rate of Li transport to the interface is governed predominantly by the diffusion of Li atoms within Li metal and Li metal creep [13]. In reality, the CCD for plating and stripping are interrelated: When the local current density at the Negative Electrode (NE)-SE interface



A combined machine learning and Density Functional Theory (DFT)-Molecular Dynamics (MD) work flow, where the materials are chosen for the DFT-MD simulations based on the predicted superionic conductivities from the logistic regression machine learning model. Reprinted with permission from Ref. [39], Copyright (2019), American Chemical Society.

exceeds the CCD for stripping, the void formation will increase the local plating current density. As a result, more Li filaments will be formed until a short-circuit and cell failure occurs (see Section 3.5) [13].

The CCD is usually measured using galvanostatic cycling with stepped current densities on a non-blocking symmetrical cell [10-12,32,45]. As solid-state Li-metal cells can be cycled safely below the limit of CCD, this parameter reveals the capability of inorganic SEs to suppress the nucleation and propagation of Li filaments [11,13]. Fig. 4a shows the influence of temperature on applied current densities: the higher the operating temperature, the larger is the current density [11,32,33]. As shown by Table 1, LiPON has the largest CCD (> 10 mA cm<sup>-2</sup>) followed by LPS  $(0.3 - 1.0 \text{ mA cm}^{-2})$  and LLZO  $(0.05 - 0.9 \text{ mA cm}^{-2})$ [10–12,32,45]. The high CCD of LiPON can be attributed to the more homogeneous film morphology with fewer grain boundaries and its lower electronic conductivity compared to LLZO and LPS SEs [12,51]. LiPON films are synthesised using the sputtering method, whereas other inorganic SEs such as LLZO and LPS films are usually made via powder processing routes such as cold-pressing, hot-pressing, tape casting and sintering. These powder processing methods result in the formation of grain boundaries, small intergranular pores and surface scratches due to polishing, which subsequently cause the SEs to be more susceptible to Li filaments propagation during operation [51]. It is

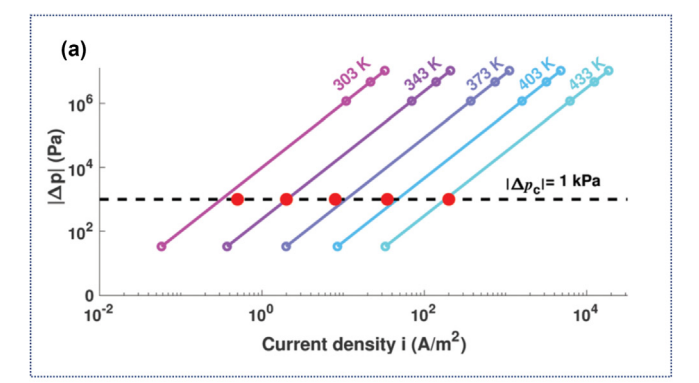
worth noting that liquid electrolytes such as fluoroethylene carbonate (FEC)-based electrolytes can be cycled at 2 mA cm<sup>-2</sup> for 1100 cycles without short-circuiting [52]. However, due to the large variability of reported CCD values in Li-metal solid-state cells, many factors could be at play influencing the reported value. Therefore, a standardised protocol in terms of cell architecture and operating conditions is urgently needed.

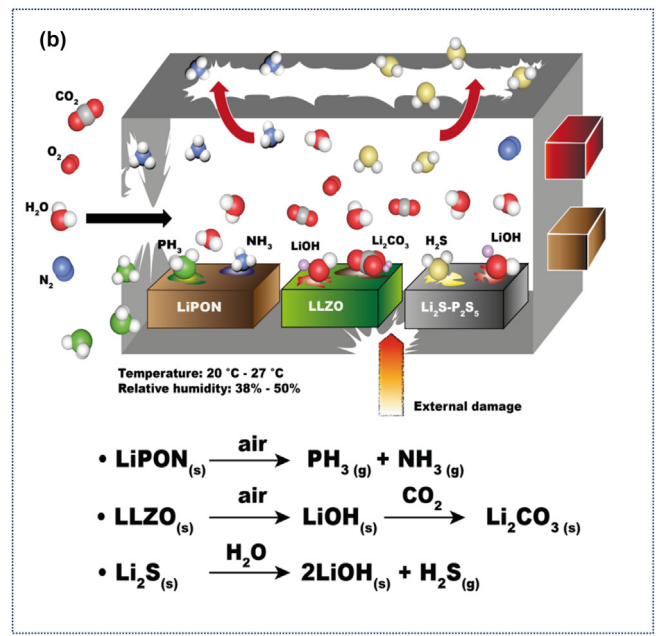
The CCD was also shown to be a function of the critical pressure,  $\Delta p_c$  [33]:<sup>2</sup>

$$i_{\rm c} = 2\pi f_{\rm int} \sqrt{6\epsilon_{\rm r} |\Delta p_{\rm c}|} = \frac{\sqrt{6\epsilon_{\rm r} |\Delta p_{\rm c}|}}{R_{\rm int} C_{\rm int}}. \eqno(1)$$

According to this model, filaments nucleate at the grain boundaries whenever the current induces a particular critical pressure described by the difference between the pressure in the electrolyte interior and its interface with the NE. The critical pressure is thus a material property containing information about the SE mechanical properties, grain structure and Li-wetting energetics. Interfaces between conductive ceramics and Li are typically capacitive, and therefore sustain space-charge layers under pressure. Since the NE resides at a higher voltage, it supports a positive space charge, inducing compressive stress in the bulk SE relative to the interface with the NE. In the case of LLZO, filaments form when the compressive energy at the Li/LLZO interface increases the free-energy cost of interfacial deposition such

<sup>&</sup>lt;sup>2</sup> The definitions of symbols given in equations of this manuscript can be found in the Appendix.





(a) The dependence of relative pressures on applied current densities and operating temperatures for Li—LLZO—Li: Although the current density was shown to increase with increasing operating temperatures from 303 K to 433 K, Li filaments nucleate whenever the current induces a critical pressure, which is far below the fracture stress for LLZO. Red dots indicate experimental critical currents. Reprinted with permission from Ref. [33], Copyright (2019), PCCP Owner Societies. (b) The chemical stability of LiPON, LLZO and LPS in air: LiPON generates toxic PH<sub>3</sub> and NH<sub>3</sub> gas [53], whereas LPS forms LiOH solid and harmful H<sub>2</sub>S gas [54]. Only LLZO was shown to form LiOH solid and Li<sub>2</sub>CO<sub>3</sub> solid upon exposure to air [55].

that it becomes more favourable to deposit Li in the grain boundaries [33].

Sakamoto and co-workers also highlighted the pressure-dependence of CCD, in creating a new terminology - critical stack pressure. At low external stack pressures, the Li stripping rate is more dominant than the mechanical deformation at the interface, inducing the formation of voids and ultimately increasing resistance of the Li/LLZO interface [56]. However, the different processes occurring during plating and stripping, especially in full cells, need further investigation.

**Electrochemical stability.** A wide electrochemical stability window of the inorganic SE is desirable. Beyond the stability window, SEs decompose at the interface, which could cause high interfacial resistance and cell failures [57,58]. Cyclic Voltammetry (CV) measurements have been shown to overesti-

mate the stability window of SEs and thus their stability with Li metal or high-voltage PE compared to the electrochemical stability window calculated from DFT [57,59-61]. For instance, it was reported that sulfide-based SEs such as Li<sub>10</sub>GeP<sub>2</sub>S<sub>12</sub> (LGPS) have a wide stability window of 0 - 5 V [1]. The apparent wide electrochemical stability window is caused by the very small decomposition current within the voltage window 0-5 V in the CV measurement and limited kinetic reactions measured with a semi-blocking cell configuration (Li-LGPS-Au) [1,57]. The measurement of the stability window using a semiblocking cell also does not reflect the solid-state composite electrode configuration, in which carbon black is often added as an additive to the SE and Active Materials (AM) to facilitate better electronic transport [47,57,62]. If the electrochemical stability window is measured with a Li-LGPS-LGPS-C-Pt cell configuration, LGPS was shown to have a limited stability window from 1.7 - 2.1 V [57]. The decomposition products for LGPS include Li<sub>15</sub>Ge<sub>4</sub>, Li<sub>3</sub>P, Li<sub>2</sub>S, GeS<sub>2</sub>, P<sub>2</sub>S<sub>5</sub> and S [57,59].

Although most oxide- and nitride-based SEs have a wider stability window than the sulfide-based electrolytes, it is worth noting that all oxide SEs form oxygen gas at high voltages (5V) [59]. Yu et al. [17] observed the formation of oxygen gas bubbles at the interface between LiPON and Pt during an anodic voltage scan to 6 V, where the possible decomposition reaction was expressed as

$$2\text{Li}_3\text{PO}_4 \longrightarrow \text{Li}_4\text{P}_2\text{O}_7 + 1/2\text{O}_2 + 2\text{Li}^+ + 2\text{e}^-.$$
 (2)

**Chemical stability.** The chemical stability of the SE with the NE and PE at open circuit conditions is also important. The stability depends on the interplay between thermodynamic driving forces and available kinetics at the reaction temperature, which is difficult to predict. Instead, computational methods are used to find the maximum chemical driving force at an interface and the possible reaction products. It can be assessed from the grand potential phase diagram that contains all chemical species in both phases [38]. Further discussions on multiphysical degradation mechanisms due to interfacial stability of SEs with NEs and PEs can be found in Section 3.

The chemical stability in the atmosphere is also a significant feature. On exposure to ambient humid air (temperature: 20°C, relative humidity: 50%), LiPON thin films were shown to react with air to form toxic PH<sub>3</sub> and NH<sub>3</sub> gas. As a consequence of this reaction, the surface RMS roughness increased from 28.8 nm to 612.8 nm and the ionic conductivity decreased from  $2.8 \times 10^{-6} \text{ S cm}^{-1}$  to  $9.9 \times 10^{-10} \text{ S cm}^{-1}$  [53]. Oxide-based SEs such as LLZO also react readily with humid air to form LiOH and Li<sub>2</sub>CO<sub>3</sub>, as shown by DFT calculation and X-ray Photoelectron Spectroscopy (XPS) analysis by Sharafi et al. [55]. The formation of Li<sub>2</sub>CO<sub>3</sub> on the surface of LLZO causes a significant increase in the Li-LLZO interfacial resistance [10,64–67]. Muramatsu et al. [54] investigated the stability of LPS SE after air exposure with Raman spectroscopy and an H<sub>2</sub>S sensor. Sulfide-based SEs were shown to be hygroscopic and formed harmful H<sub>2</sub>S gas on exposure to water molecules in the air (temperature: 26 °C-27 °C, relative humidity: 38–39%) [54]. The formation of these harmful gases due to the reactivity of the SEs with air has two significant implications. Firstly, all-solid-state batteries must be manufactured and assembled under a controlled environment such as a dry room. Secondly, mechanical damage of the batteries in real-

TABLE 1

Multiphysical properties of three representative classes of inorganic SEs

| Properties  | LiPON  | LLZO  | LPS                         | Method  | Ref.       |
|---|--|---|-----------------------------|---|------------|
|   |  | Electrochemical/                              |                             |   |            |
|   |  | Chemical properties                           |                             |   |            |
| lonic conductivity, $\sigma_{\rm elec}^*$ [S cm <sup>-1</sup> ]     | $10^{-6}$  | $10^{-4}$                                     | $10^{-4} - 10^{-3}$         | EIS   | [29,32,48] |
| Electronic conductivity, $\sigma_{e^-}^*$ [S cm <sup>-1</sup> ]     | $10^{-14}$   | $10^{-8}$                                     | $10^{-9}$                   | Hebb-Wagner DC polarisation                   | [12,48,96] |
| Electrochemical stability window vs. $\text{Li/Li}^+$ [V]           | 0.68 - 2.63  | 0.05 - > 5.0                                  | 0 - 2.01                    | DFT   | [57,59,97] |
| Relative permittivity, $\epsilon_{\rm r}$ [-]                       | 19.98 (thin-film)                                  | 40 (bulk) 152 (thin-film)                     | -                           | EIS   | [6,46,48]  |
| CCD, $i_c^{**}$ [mA cm <sup>-2</sup> ]                              | > 10   | 0.05 - 0.9                                    | 0.3 - 1.0                   | Step-increased DC cycling                     | [10-       |
| , , , ,   |  |   |                             | ,   | 12,32,45]  |
| Exposure to moisture  | Form toxic PH <sub>3</sub> and NH <sub>3</sub> gas | Form LiOH and Li <sub>2</sub> CO <sub>3</sub> | Form toxic H <sub>2</sub> S | DFT, XPS, H <sub>2</sub> S sensor             | [53–55]    |
|   |  | Thermal properties                            |                             |   |            |
| Specific heat capacity, $C_{ m p,SE}$ [J kg $^{-1}$ K $^{-1}$ ]     | 1400   | 553   | -                           | DSC, Neumann–Kopp calculation                 | [80,81]    |
| Thermal conductivity, $k_{SE}$ [W m <sup>-1</sup> K <sup>-1</sup> ] | 1.4  | 0.47  | -                           | MTRM  | [80,85]    |
| Activation energy, $E_{A,SE}$ [eV]                                  | 0.51   | 0.42  | 0.39 - 0.52                 | Arrhenius                                     | [32,44,98] |
| Density, $\rho_{\rm SE}$ [g cm <sup>-3</sup> ]                      | 2.68   | 5.08 - 5.34                                   | 1.45 - 1.91                 | PUS, Mass and length                          | [23,80,99] |
| Thermal expansion coefficient, $\epsilon_{\rm T} \ [{\rm K}^{-1}]$  | _  | $1.55 \times 10^{-5}$                         | -                           | XRD   | [19,89]    |
|   |  | Mechanical properties                         |                             |   |            |
| Young's modulus, E [GPa]  | 77   | 147–150                                       | 8.8–25                      | Nanoindentation, impulse excitation, DFT, USV | [23,91,99] |
| Poisson's ratio, v [-]  | 0.25   | 0.26  | 0.27 - 0.33                 | Assumption, RUS, USV                          | [91,94,99] |
| Shear modulus, G*** [GPa]   | 31   | 58 - 60                                       | 3.4 - 9.5                   | USV   | [23,91,99] |
| K/G-ratio [-]   | 1.66****   | 1.59 - 1.74                                   | 1.88 - 2.58****             | DFT   | [23]       |
| Fracture toughness, $K_c$ [MPa m <sup>1/2</sup> ]                   | -  | 1.25  | 0.23                        | Vickers indentation                           | [93,100]   |
| Hardness, $H_{\rm v}$ [GPa]   | 3.9  | 6.3   | 1.9                         | Vickers indentation                           | [91,93,94] |

 $<sup>\</sup>dagger$  The definition of these metrics, acronyms and symbols can be found in the Appendix.

world applications leading to exposure of the components to air could potentially cause health hazards to anyone nearby (see Fig. 4b). It is worth noting that the amount of  $H_2S$  gas released was recorded for a pelletised cell in a controlled environment after exposure to air for a minimal period [54]. If solid-state batteries would be scaled up, in which each battery pack has hundreds of cells, and each unit cell has hundreds of layers, the impacts of harmful gas release due to mechanical damage such as battery crash cannot be neglected. This safety evaluation aspect is urgently needed before solid-state batteries can be employed for large-scale applications in electric vehicles or aircraft.

**Relative permittivity.** The relative permittivity is a physical property that characterises the strength of the electrostatic force acting between the electrodes and the SE in the space-charge layers. The relative permittivity of any given medium is inversely proportional to the electrostatic force,  $F_c$ , as shown by Coulomb's law:

$$F_{\rm c} = \frac{Q_1 Q_2}{4\pi\epsilon_0 \epsilon_{\rm r} d_{\rm int}^2}. \tag{3}$$

The square root of the relative permittivity is directly proportional to the Debye length,  $\lambda$ , at the interface [68,69]:

$$\lambda = \sqrt{\frac{\epsilon_{\rm r}\epsilon_{\rm 0}R_{\rm gas}T}{F^2\sum_{i}z_{i}^2c_{\rm bulk}}}.$$
 (4)

The Debye length denotes the characteristic length scale of the space-charge layer and usually has a thickness in the range of nm [70–72]. As shown by Table 1, the relative permittivity is different for LiPON and LLZO. It should be noted that the relative permittivity is also a function of frequency and temperature [48,73]. By using the zero-frequency limit of the relative permittivity, Braun et al. computed the thickness of the space-charge layers and showed that the fraction of cations at the interfaces depend strongly on the thickness of the space-charge layers [70]. A large relative permittivity indicates a thicker space-charge layer but a weaker electric field [72]. The implications of the space-charge layers on the cell performance will be further discussed in Section 4.1.3.

## 2.2. Thermal properties

**Effects of operating temperatures.** The operating and storage temperatures are critical parameters that affect the performance and lifespan of solid-state batteries. Temperature-dependent properties such as the ionic conductivity and the activation energy are usually described with the Arrhenius law [6,32,44,46,48]. High operating temperatures can facilitate better

<sup>\*</sup> Measurement at room temperature.

<sup>\*\*</sup> The CCD of fluoroethylene carbonate (FEC)-based electrolyte solution is 2mA cm<sup>-2</sup> (1100 cycles) [52].

<sup>\*\*\*</sup> The shear modulus of Li metal is 4.25GPa [23].

<sup>\*\*\*\*</sup> Calculated in this work.

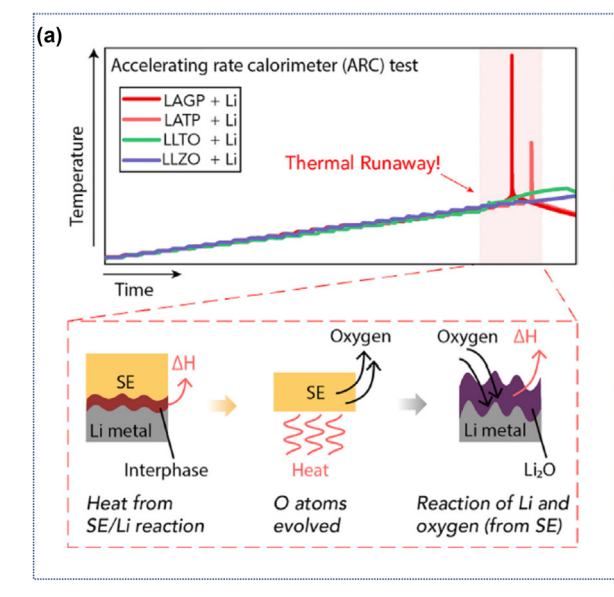
interfacial kinetics and ionic diffusion in the PE, but also accelerate the decomposition reactions. For example, Larfaillou et al. [48] showed that the LiPON SE had an electrolyte resistance up to 2000  $\Omega$  at -10 °C but dropped to  $100 \Omega$  at 30 °C. However, the lifespan of the cell also decreases significantly with increasing operating temperature. Wang et al. [74] showed that a cell cycled at 80  $^{\circ}\text{C}$  loses about 35% of the initial capacity while a cell cycled at 25 °C retains the same initial capacity. The loss of cell capacity at high operating temperatures was attributed to the decomposition reaction in the disordered LiCoO2 (LCO) layer at the electrode-electrolyte interface. Although a low operating temperature such as 0 °C could potentially reduce the rate of interfacial decomposition, studies in conventional Li-ion batteries show that other degradation mechanisms such as nonuniform Li plating could be significant under fast-charging at low temperature [75]. Moreover, the significant electrolyte resistance at low temperature indicates that sluggish ionic mobility in the SE would impede the overall cell performance [48]. However, the lack of reports on low-temperature performance and degradation in solid-state batteries highlights a gap for future studies.

**Thermal stability.** While safety is a concern for conventional Li-ion batteries due to flammable esters and ethers [76], Chen et al. [63] demonstrated recently that the oxygen generation from oxide-based SEs at elevated temperature cause thermal runaway with highly reactive Li metal. By using Accelerating Rate Calorimeter (ARC) combined with first-principles calculations, they compared the thermal stability of Li metal with different SEs (LAGP, LATP, LLTO and LLZO). In SEs such as LAGP, LATP and LLTO, decomposition interphases formed after the Ti/Ge electrolytes contacted with the metallic Li. The release of oxygen from the SEs at elevated temperatures was shown to initiate a

highly exothermic reaction with molten Li metal, leading to thermal runaway. However, LLZO was shown to have the highest onset temperature of  $\rm O_2$  release, indicating the thermal stability of LLZO with Li metal at elevated temperature (Fig. 5a) [63].

On the other hand, the thermal stability of NMC-LPS composite PE was investigated by Tsukasaki et al. [77]. By using a combination of experimental techniques such as Differential Scanning Calorimetry (DSC), *in-situ* X-ray Diffraction (XRD), *ex-situ* Transmission Electron Microscopy (TEM) and Scanning Electron Microscopy (SEM), they showed a significant morphological change occurring in the NMC-LPS composite PE after heating above 300°C. NMC decomposed into transition metal sulfides and generated  $O_2$  gas, further causing LPS to oxidise to  $Li_3PO_4$  [77]. When the LPS SE in the composite PE was replaced with  $Li_4SnS_4$  (LSS) SE, the reactivity of LSS and NMC was shown to be much lower than that of LPS-NMC due to the stability of  $O_2$  gas with LSS SE [78].

Heat generations and transport. Because of the strong temperature-dependent cell behaviour, it is essential to analyse the heat generation mechanism inside the cell. The heat generation in a single-layer cell is insignificant because the surface-to-volume ratio is large [18]. However, for a cell stack with many units, the heat generation can be significant, especially for operating conditions at high current densities. In solid-state batteries, heat is generated due to irreversible heat sources such as ohmic transport across the SE, activation overpotential at both interfaces and species transport due to concentration gradients in the electrodes. Simultaneously, the reversible heat generation can also occur due to the structural change of the PE and NE. The generated heat is predominantly transferred to the surface through the heat conduction mechanism and is subsequently



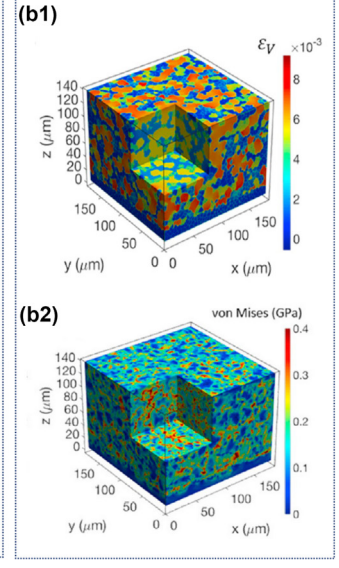


#### FIGURE 5

(a) Thermal stabilities of oxide-based SEs with Li metal: While thermal runaway behaviours could be observed with LAGP + Li, LATP + Li and LLTO + Li, LLZO SE exhibits no thermal runaway at elevated temperature. Reprinted with permission from Ref. [63], Copyright 2020, Elservier. (b) The impacts of a thermal contraction from 750°C to 27°C on the (b1) fractional volume change and (b2) von Mises stresses of the composite PE. The composite PE consists of NMC as AM, LLZO as SE and Ni as the electronic conductor. The fractional volume change indicates the volumetric contraction or expansion of the constituent particles relative to LLZO, whereas the von Mises stress quantifies the local combined thermal stress state of the composite particles. Reprinted with permission from Ref. [19], Copyright (2019), Elsevier.

dissipated to the surroundings through convection and radiation [18]. Therefore, the heat generation and heat transfer mechanisms can be described by the energy balance as follows [18,79]:

$$\underbrace{\rho_{\text{eff}} C_{\text{p,eff}} \frac{\partial T}{\partial t}}_{\text{thermal energy storage}} = \underbrace{\frac{\partial}{\partial x} \left( k_x \frac{\partial T}{\partial x} \right) + \frac{\partial}{\partial y} \left( k_y \frac{\partial T}{\partial y} \right)}_{\text{in-plane heat conduction}} + \underbrace{\frac{\partial}{\partial z} \left( k_z \frac{\partial T}{\partial z} \right)}_{\text{cross-plane heat conduction}} + \underbrace{\frac{Q_{\text{gen}}}{Q_{\text{gen}}} - \frac{Q_{\text{conv}} - Q_{\text{rad}}}{Q_{\text{heat dissipation}}}}_{\text{heat generation}}.$$
(5)

**Specific heat capacity.** A high effective specific heat capacity indicates a better storage of thermal energy and a smaller temperature increment for unit heat input. LiPON has a higher specific heat capacity  $(1400\,\mathrm{J\,kg^{-1}\,K^{-1}})$  than LLZO  $(553\,\mathrm{J\,kg^{-1}\,K^{-1}})$  (see Table 1) [80,81]. In contrast, the current collector such as copper has a specific heat capacity of only  $390\,\mathrm{J\,kg^{-1}\,K^{-1}}$ . Such a low magnitude of specific heat capacity means that the temperature increase around the tabs and current collectors will be higher than the other cell components.

Thermal conductivity. In general, the thermal conductivity of a conventional Li-ion cell is highly anisotropic for cylindrical, pouch and prismatic configurations due to the layered arrangement of each component. Depending on the cell layer configuration, the effective thermal conductivity of a cell can be estimated from the thermal conductivity of each material by assuming parallel or series resistances for each cell layer (see Table A.1 in Appendix A) [82,83]. While the difference between the cross-plane and in-plane specific heat capacity is negligible, the in-plane thermal conductivity of each cell component can be larger than the cross-plane thermal conductivity by a factor of 6-13 [18,84]. Xu et al. showed that LiPON has a cross-plane thermal conductivity of 1.4 W m<sup>-1</sup> K<sup>-1</sup> [80]. Different cell manufacturing processes were also shown to affect the thermal conductivity. Bock and co-workers showed that a non-sintered a cross-plane thermal conductivity  $0.22 - 0.23 \text{ W m}^{-1} \text{ K}^{-1}$ , whereas a sintered LLZO has a thermal conductivity higher by a factor of two  $(0.47 \text{ W m}^{-1} \text{ K}^{-1})$  [85]. However, none of these reports have studied the effects of plane orientations on the measured thermal conductivity of the SE. For a layered PE such as LCO, Yang et al. showed from the firstprinciples calculation that the in-plane thermal conductivity is 53.6 W m<sup>-1</sup> K<sup>-1</sup>, whereas the cross-plane thermal conductivity is only 8.4 W m<sup>-1</sup> K<sup>-1</sup> [86]. This difference in the material thermal conductivity can be attributed to the higher mobility of the heat-carrying phonon modes in-plane compared to crossplane [84,86]. Compared to the thermal conductivity of the SE or PE, Li metal has a higher thermal conductivity of 81.8 W m<sup>-1</sup> K<sup>-1</sup> [83], though it is not clear whether this value refers to the thermal conductivity of a single crystal Li or polycrystalline bulk Li. Although no studies have demonstrated the impacts of void formation on the interfacial thermal resistance of a solid-state cell, contact loss between the SE and the Li metal could potentially create additional thermal resistance to affect the effective heat transport. For a cell stack consisting of many unit cells, the smaller effective cross-plane thermal conductivity means a higher magnitude of heat accumulation across the stack thickness. Therefore, optimising the stack thickness and designing cells for effective thermal management are essential for largeformat solid-state batteries [18,87,88].

**Thermal expansion coefficient.** Recently, Yu et al. [19] evaluated the thermal stress in composite PEs due to cooling from the sintered temperature at 750°C. The misfit strain resulting from the temperature change,  $\epsilon_T$ , can be calculated by

$$\epsilon_{\rm T} = (\alpha_{\rm T1} - \alpha_{\rm T2})\Delta T,\tag{6}$$

where  $\alpha_{T1}$  and  $\alpha_{T2}$  are the thermal expansion coefficients of bonded materials in the composite PE. LLZO has a thermal expansion coefficient of  $1.5\times 10^{-5}~\text{K}^{-1}~$  [19,89]. Fig. 5b shows the simulated microstructures to assess the impacts of sintering and cooling on the thermal stresses in the composite PEs. By comparing the fractional volume change and dilatational stresses of the constituent particles in the composite, they found that NMC and Ni particles are under compression, whereas LLZO particles are under tension. The von Mises stresses were shown to concentrate on the boundaries between grains of two different materials in the composite. Therefore, intergranular cracks are more likely to occur than intragranular ones [19].

#### 2.3. Mechanical properties

**Elastic moduli.** In solid mechanics, the material's elastic, plastic and fracture behaviour can be described by the stress–strain relationship of a material. From the stress–strain measurements, mechanical properties such as the elastic moduli, yield strength, ultimate tensile strength and ductility, can be inferred [90]. An elastic solid will return to its original shape and size after the forces deforming the solids are removed. This elastic behaviour can be described by the linear relationship between the applied stresses and strains. Depending on the directions of the applied forces, the elastic moduli can be described with the Young's modulus (E), shear modulus (G) or the bulk modulus (K).

The Young's modulus can be measured with the nanoindentation, acoustic impulse excitation technique, load frame tensile or compression testing or Resonant Ultrasound Spectroscopy (RUS) [21,23,91–94]. Masias et al. measured the Young's modulus of polycrystalline Li with the pulse-echo acoustic method and showed that the bulk polycrystalline Li has a Young's modulus of 7.8 GPa [21]. Unlike the polycrystalline Li, the elastic moduli of a single crystal Li were shown to vary significantly with the crystallographic orientations due to the high Zener anisotropy factor, A, of the body-centred cubic Li (A = 8.52) [21,95]. It is worth noting that an isotropic material has an A-value of 1 [21,23]. A high anisotropy factor of the single crystal Li implies that the local mechanical properties of Li grain may differ significantly from grain to grain, which causes different propensity for the propagation of Li filaments [95]. By conducting micro-pillar compression experiments in an operando SEM, Xu et al. [95] showed that Li exhibits an E value of approximately 5 GPa in the [100] orientation, whereas the E value is around 20 GPa in the [111] orientation.

Due to variances in the experimental setup (*i.e.*, a load frame tensile testing with and without the extensometer), the reported Young's modulus of the polycrystalline Li varies significantly between 1.9-7.8 GPa [21]. Besides, a clear differentiation should be made between engineering and true strain measurements when measuring the stress–strain relationship. The stress and strain calculated with the original cross-section areas are known as the engineering stress and strain. In contrast, the stress

and strain calculated with the cross-sectional area's instantaneous change are denoted as the true stress and strain. Both measurements of the same sample can yield very different results, as shown by Masias et al. [21] in Fig. 6a. Nevertheless, it should be noted that for compression testing, the true stress should be smaller than the engineering stress due to the increase in the cross-sectional area with compression. LePage and co-workers showed that the instantaneous change of a cross-sectional area could be measured with the glove-box integrated digital-image correlation (DIC) (Fig. 6b), in order to determine the true stress and strain of bulk Li metal [101].

Compared to Li metal, SEs such as LiPON and LLZO have a high Young's modulus of 77 GPa and 150 GPa respectively [23,91]. In contrast, sulfide-based SEs have a low Young's modulus of only 8.8 – 25 GPa [93,99]. A lower Young's modulus also corresponds to a lower shear modulus and therefore a weaker ability to suppress the Li filaments, according to the Monroe and Newman's linear elasticity analysis [102]. Yu and coworkers calculated the anisotropy ratio of LLZO and showed that Al- and Ta-doped LLZO have an anisotropy ratio of 1.27 and 1.32, respectively. Compared to the anisotropy ratio of Li metal, the elastic properties of LLZO can be considered as isotropic [23].

The pioneering work by Monroe and Newman [102] proposed the linear elasticity analysis and derived the interfacial stability parameter from a modified Butler–Volmer (BV) equation. If the total interfacial stability parameter is positive, the roughness of the Li electrode tends to cause an unstable deposition due to a

faster deposition on the peaks of the deformed electrode surfaces than on the undeformed electrode surfaces. Therefore, a negative stability parameter favours a stable deposition. When the shear modulus of the SE is lower than twice the shear modulus of the Li electrode, the total interfacial stability parameter becomes positive, indicating a faster deposition of Li on the local peaks. As a result, they suggested that a SE should have a shear modulus at least two times larger than the shear modulus of Li metal to prevent the Li filaments initiation [102]. The shear modulus of LiPON and LLZO are 7 - 14 times larger than the shear modulus of Li respectively, whereas the LPS SE is just sufficiently compliant [23,91,99]. Yet, despite the high shear modulus of LLZO, the growth of Li filaments are still observable in LLZO [14,103]. Besides the shear modulus, the formation of Li filaments also depends on the critical plating and stripping current densities, grain morphologies of the SEs and the surface flaws [12,13,32,51,104]. Therefore, meeting Monroe's criterion should be a necessary criterion, but not an absolute sufficient condition to prevent an internal short-circuit [23,102].

**Plastic deformation.** If the shear stress exceeds the critical shear stress in the slip plane and directions (*i.e.* a slip system with the largest Schmid factor), the lattice planes begin to slip, and an irreversible plastic deformation begins.

The Critical Resolved Shear Stress (CRSS) of metallic Li was shown to depend on the Li pillar diameters and temperatures [95]. Based on the micro-pillar compression measurements, Xu et al. [95] showed that the CRSS of Li decreases from about

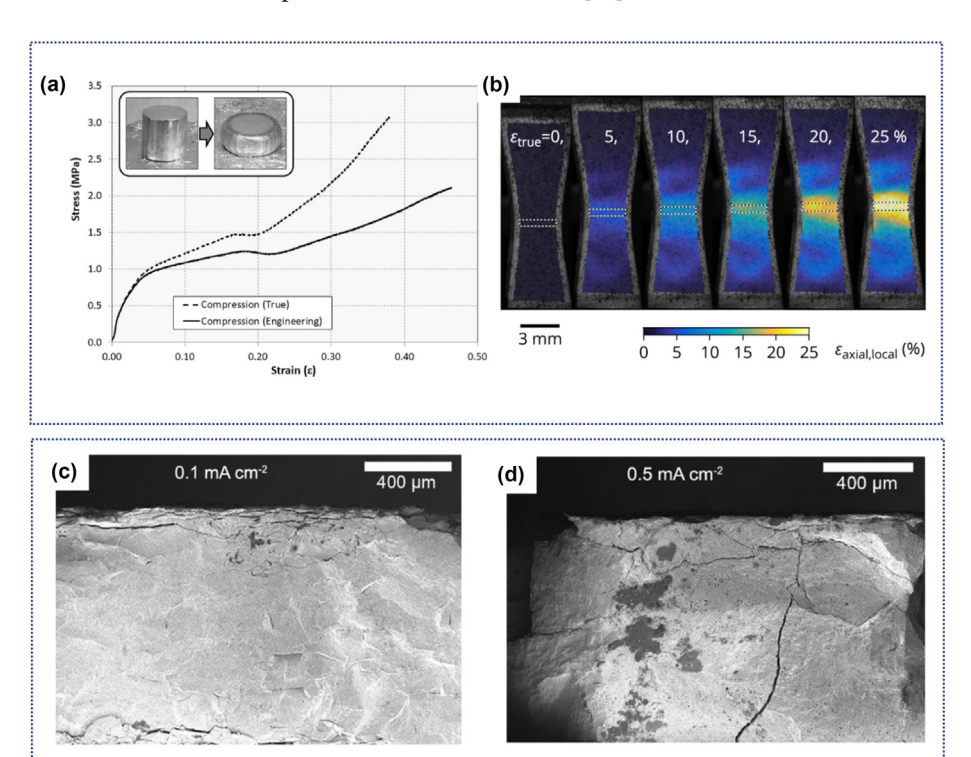


#### FIGURE 6

A contrast in the mechanical behaviour of a solid Li and a SE: A solid Li NE demonstrates a significant time-dependent deformation at room temperature under both (a) compressive (Reprinted with permission from Ref. [21], Copyright (2019), Springer) and (b) tensile testings (Reprinted with permission from Ref. [101], Copyright (2019), The Electrochemical Society). In Figure (b), the changes in the axial strain maps were obtained by using 3D digital image correlation [101]. Low-magnification cross-sectional Scanning Electron Microscopy (SEM) images of Li<sub>1+x</sub>Al<sub>x</sub>Ge<sub>2-x</sub>(PO<sub>4</sub>)<sub>3</sub> (LAGP) cycled until failure at (c) 0.1mA cm<sup>-2</sup> and (d) 0.5mA cm<sup>-2</sup>. Brittle cracks through the SE are observed at high current densities due to reaction processes at the LAGP—Li interface (Reprinted with permission from Ref. [16], Copyright 2019, American Chemical Society).

30MPa to about 6MPa when the pillar diameters increase from 1μm to 10μm. These measurements imply that the deformation behaviour of Li filaments is highly dependent on the size of the filaments that form at the interface. They also showed that the CRSS decreases with increasing operating temperature. Li has a low melting point and a high homologous temperature (i.e. the ratio of absolute operating temperature to the absolute melting temperature). The homologous temperature of Li corresponds to 0.65 at 298.15K and 0.8 at 363K. Due to thermally activated processes such as cross-slip and dislocation climb, the dislocation movement is not limited to slip planes with the largest resolved shear stress when the homologous temperatures increase. Therefore, plastic deformation occurs more easily to induce more in-plane growth of Li, causing a smoother surface at the top of the deposit. As a result, they suggested that higher operating temperatures are more favourable in suppressing the Li filaments [95]. While a certain degree of plastic deformation is desirable to smoothen the local filament peaks, a high homologous temperature of Li also triggers Li creep (see Section 3.3) [21,101]. An unrestrained creep could eventually cause an internal short-circuit against the PE [21].

Compared to Li NE, a SE should exhibit minimal plastic deformation to withstand the propagation of Li filaments through the SE. The resistance of the SE to plastic deformation can be described by the parameter Vickers Hardness ( $H_v$ ), and  $H_v$  was shown to decrease with increasing porosity [94]. For a volume fraction porosity of 0.03, LLZO has a  $H_v$ -value of 6.2 – 6.4 GPa. As the volume fraction porosity increases to 0.06, the  $H_v$ -value decreases to 5.2 – 5.3 GPa [94]. A SE with a higher porosity has more pores and less denser microstructures, which could cause more Li filaments to penetrate through the pores (see Fig. 7).

On the other hand, the LPS SE has a  $H_{\rm v}$ -value of 1.9 GPa, which implies a lower resistance to plastic deformation compared to oxide-based SE [93].

Fracture behaviour. The brittle nature of the ceramicbased SEs suggests that these SEs are more susceptible to cracks [104,105]. A crack will grow when the crack tip stresses exceed the critical stress threshold (fracture toughness,  $K_c$ ) [105]. Qi et al. [106] suggested that local residual tensile stresses promote Li filament penetration via crack propagation in SEs, in analogy to the stress corrosion cracking seen in the corrosion field. Stress corrosion cracking occurs when a component's surface is (electro) chemically attacked at a defect or heterogeneity. The result is the formation or growth of a developing crack that can only grow if the crack tip is in a sufficiently high state of tension. Therefore, they proposed putting the surface of the SE into a state of compressive stress, for example with ion implantation [106]. In principle,  $K_c$  can vary depending on the crack mode (opening mode, sliding mode and tearing mode) [107]. LLZO has a fracture toughness of 1.25 MPa m<sup>1/2</sup>, whereas LPS has a fracture toughness of 0.23 MPa m<sup>1/2</sup> [93,100]. A current collector made of aluminium has a fracture toughness of 25 - 35 MPa m<sup>1/2</sup> [23]. A detailed discussion on the degradation mechanisms of electrode particles and SE cracking can be found in Section 3.1.

In contrast to the liquid electrolyte, which can penetrate through the pores and wet the solid electrodes, the problems of contact loss and voids are more apparent for a solid–solid interface [13,108]. Therefore, some degree of ductility is essential to maintain good interfacial contacts for a solid-state cell. The ratio of bulk modulus to the shear modulus (K/G) indicates the ductile/brittle nature of a solid [23,109]. According to the Pugh's criterion, the critical K/G ratio for a transition from brittle to ductile

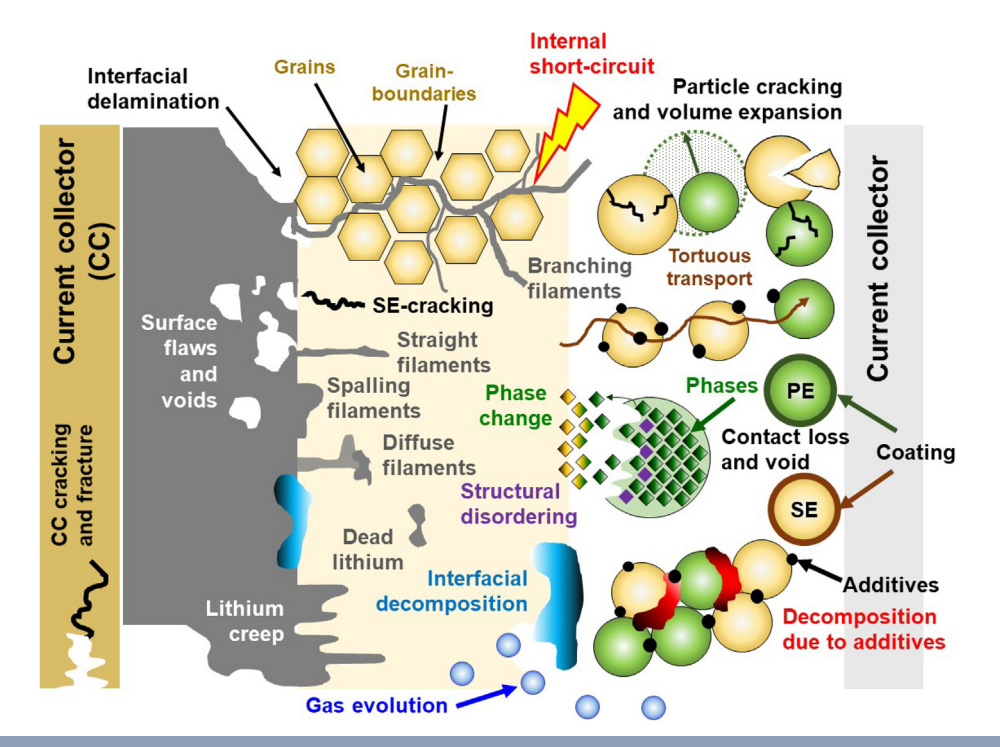


### FIGURE 7

A summary of degradation mechanisms in a solid-state Li-metal cell, which include interfacial delamination, Li filaments propagation, surface voids and flaws, SE cracking, electrode particle cracking and volume expansion, tortuous transport, contact loss and void, interfacial decomposition, Li creep, decomposition due to additives, phase change, structural disordering, gas evolution, CC cracking and fracture.

behaviour is 1.74 [23,109]. This transition criterion was determined by grouping a wide range of brittle as well as ductile metals into groups according to their lattice structure and comparing their elongation percentage and Poisson's ratio at room temperature. A low K/G ratio corresponds to a brittle material, in which the stress concentration at the root of a crack will be high due to a negligible plastic flow [109]. LLZO has a K/G-ratio of 1.59 - 1.74, which implies the brittle nature of the SE [23]. In contrast, the LPS SE has a K/G-ratio between 1.88 and 2.58 (see Table 1), and the current collectors such as copper and aluminium have a K/G-ratio of 3 and 2.74 respectively [109]. However, the mechanical properties of pure copper foils were also shown to depend on the thickness of the foils [110]. By investigating the effects of different thickness on mechanical properties of pure copper foil during cold rolling, Song et al. [110] showed that the ultimate strength of pure copper foil first increases from 310 MPa to 390 MPa when the foil thickness decreases from 300 μm to 100 μm. The further reduction of the foil thickness to 25µm causes the ultimate strength to drop to 300 MPa due to the decrease in the dislocation density and micro-strain. Despite the high K/G ratios of copper, this experimental observation suggests that thinner copper foils are more brittle and susceptible to fracture and cracks [110].

## 3. Multiphysical degradation and failure modes

The complex interplay of different mechanisms in solid-state batteries induces various degradations and failure modes. For instance, although the addition of carbon black in the composite electrode improves electronic transport, it also causes an increase in the interfacial resistance and a faster capacity fade [62,111,112]. The irreversible capacity loss in solid-state batteries could also be caused by the formation of a passivating PE/electrolyte interface layer due to the decomposition of the electrolyte and the phase change/structural disordering of electrodes [59,74,113]. On the other hand, surface flaws and voids at the SE-NE interface can cause the nucleation of Li filaments and reduce the lifespan of solid-state batteries as a result of an internal short-circuit [13,104,105]. While we have discussed the multiphysical properties of different cell components in Section 2, we analyse the degradation and failure mechanisms in this Section and review the effects of different operating conditions on the solid-state battery degradation (see Table 2). Many efforts have been made using experiments to understand the degradation of solid-state batteries. By coupling experimental observations with calculations, it is hoped that a clearer understanding of degradation can be achieved. The development of in-situ techniques, such as in-situ XPS, Raman and STEM, are being developed for characterisation of often-buried and air-sensitive interfaces. Table 3 summarises the experimental tools and techniques which are used for characterising degradation and referred to throughout this review.

## 3.1. Mechanical stresses

Due to the brittle nature of the inorganic SEs (see Table 1), as well as the rigid contact between the electrodes and the electrolyte, the accumulation of mechanical stresses in solid-state cells cause a more severe performance drop compared to liquid electrolytes.

The propagation of stresses causes particle cracking, which eventually impedes the ionic mobility and increases the cell resistance.

#### 3.1.1. Lithiation-induced stresses

The diffusion of Li-ions into and from the electrode host materials generates volume change [115,116]. This structural and morphological evolution can give rise to mechanical stress accumulation and significantly influence the cell performance.

Negative electrodes. The degradation mechanism of an intercalation electrode and a composite NE is different from that of a NE composed of pure metallic Li. A composite NE denotes an electrode composed of SE and NE (see Fig. 12c2)). The ionic diffusion in the electrode host such as graphite was shown to cause a structural change, as shown by Otoyama et al. [117]. They employed operando confocal microscopy to observe the dynamic thickness evolution of graphite-based solid-state cells. During cycling, the graphite underwent irreversible volume change, and the thickness of the graphite layer increases due to the formation of voids and cracks, which cause the capacity to decay. Significant volume change was also reported in Si-based solidstate cells. Chen et al. [118] employed an operando NDP method to investigate the degradation of thin-film Si-Li<sub>3</sub>PO<sub>4</sub>-LCO cells. They demonstrated that the Si electrodes underwent a significant volume change during cycling that resulted in the penetration of the SE. Bucci et al. [119] proposed a coupled electrochemical-m echanical model based on the cohesive zone formulation to investigate the intercalation-induced stresses in the composite NE. By assuming Young's modulus of 15 GPa, the model predicted that the fracture could be prevented if the electrode particle's expansion is lower than 7.5% and the SE fracture energy is higher than 4 J m<sup>-2</sup>.

Positive electrodes. The lithiation and (de)-lithiation in the composite PE also causes a volume expansion and contraction, which introduces internal stresses. These stresses lead to the formation of cracks in both AMs and SEs to affect cell integrity and lead to a severe increase in the interfacial resistance (Table 2). Liu et al. [120] revealed that the large volume change of LCO during cycling creates cracks in the electrodes of LCO/ LLZ-Ta. As a result, the accumulated cracks disrupt the ionic diffusion path, causing an increase in the cell resistance leading to degradation. The anisotropic plane orientations of the PE could also cause the formation of the concentrated stress within the particles. Jung et al. [114] investigated the volume change of LiNi<sub>0.8</sub>Co<sub>0.16</sub>Al<sub>0.04</sub>O<sub>2</sub> (NCA-80) with randomly oriented grains in Li<sub>6</sub>PS<sub>5</sub>Cl based cells. They demonstrated that the anisotropic volume changes of primary particles in NCA-80 collectively cause the severe cracking of secondary particles (Fig. 8a). However, in the  $Li(Ni_{0.75}Co_{0.10}Mn_{0.15})$   $O_2$  with radially oriented rodshaped grains, the volume change and stress can be accommodated, resulting in mechanical integrity and cycle stability.

In terms of physical modelling, Behrou and Maute [121] proposed an electrochemical–mechanical model, which describes diffusion-induced mechanical stresses in the PE. By modelling the electrode diffusion as a function of the damage parameter, they showed that damage evolution in the PE causes the cell's capacity to fade during discharge.

TABLE 2

Solid-state cell degradation mechanisms: The effects of operating conditions, causes and consequences.

| Degradation<br>mechanisms                        | High<br>SOC | Low<br>SOC | High<br>temp | Low*<br>temp | High<br>C-<br>rate | Low<br>stack<br>pressure | Causes   | Consequences  | Ref.                  |
|--|-------------|------------|--------------|--------------|--------------------|--------------------------|--|---|-----------------------|
| Electrodes and SE<br>cracking                    | т           | Т          |              |              | Т                  |                          | <ul> <li>Volume change of the AMs during charge/discharge;</li> <li>Interfacial reactions and the resulting growth of decomposition layers;</li> <li>Propagation of Li filaments through the SE.</li> </ul>  | <ul> <li>Disruption of the ionic diffusion path;</li> <li>Contact loss between electrodes and the SE;</li> <li>Increase in the interfacial resistance;</li> <li>Decrease in the mechanical strength of the SE;</li> <li>Faster and easier propagation of Li filaments.</li> </ul> | [120; 20; 124; 123]   |
| Phase change<br>and structural<br>disordering    | Т           | Т          | Т            |              |                    |                          | <ul> <li>Sluggish ionic diffusion due to poor interfacial contacts;</li> <li>Transition metal dissolution at the PE and SE interface.</li> </ul>   | <ul> <li>Capacity decay due to the loss of the AM; Disor-<br/>dered/rock-salt phases between electrodes and the<br/>SE; Increase in the interfacial resistance.</li> </ul>  | [74,120,139]          |
| Li creep   |             |            | Т            | Т            |                    |                          | <ul> <li>High homologous temperature of<br/>Li metal.</li> </ul>   | <ul><li>Severe deformation and volume change of the NE;</li><li>Higher risk of internal short-circuit.</li></ul>  | [21,101,140,141]      |
| Interfacial<br>decomposition                     | Т           | Т          | Т            |              | Т                  |                          | <ul> <li>Limited chemical stability of the SE towards Li metal or high voltage transition metal oxide PE;</li> <li>Carbon additives accelerate the decomposition of the SE.</li> </ul>   | <ul> <li>The growth of the decomposition layers increases the interfacial resistance;</li> <li>Loss of the AMs decreases the capacity;</li> <li>Produce localised pressure to trigger the formation of cracks in SE.</li> </ul>   | [16,20,63,74,142]     |
| Surface voids and<br>interfacial<br>delamination |             |            |              |              | T                  | Т                        | <ul> <li>Voids or defects produced during materials processing;</li> <li>Rigid contact between the electrodes and SE;</li> <li>Volume change of the AMs during charge/discharge;</li> <li>Li plating/stripping exceeding CCD.</li> </ul>   | <ul> <li>Poor contact causes insufficient ion diffusion and limits the rate performances;</li> <li>Localised high current and pressure accelerate the growth of Li filaments.</li> </ul>  | [13,108,137,143,144]  |
| Li filamentary<br>growth                         |             |            |              | Т            | T                  | Т                        | <ul> <li>Voids and flaws on the surface of<br/>SE trigger the heterogeneous diffusion of Li-ion;</li> <li>Localized high current at the grain<br/>boundaries of SE;</li> <li>Reduction of Li<sup>+</sup> within the SE due<br/>to high electronic conductivity of<br/>the SE.</li> </ul> | <ul> <li>Internal short-circuit;</li> <li>Loss of Li inventory.</li> </ul>  | [11,12,13,32,136,145] |

<sup>\*</sup>A low temperature in this table also includes the room temperature. The letter "T" indicates the operating condition that triggers the corresponding degradation modes.

TABLE 3

| Techniques         | Degradation mechanisms   | Challenges and limitations  | Ref.                                |
|--------------------|--|---|-------------------------------------|
| cv                 | <ul> <li>Electrochemical stability windows;</li> <li>Redox reaction analysis.</li> </ul>   | The absence of voltammetric currents may be caused<br>by passivation layers rather than indicative of lack of<br>a thermodynamically favourable reaction for electrolyte decomposition;   | [57,127,192<br>[177,193]            |
|                    |  | <ul> <li>Too high scan rates are often employed;</li> <li>The stability of SE should be measured with a non-blocking cell configuration.</li> </ul>   |                                     |
| DEMS               | <ul> <li>Measuring the gas release during the decomposition of SE and PE.</li> </ul>   | • Special cells are needed to monitor the gas release with the mass spectrometry.   | [135]                               |
| DSC and ARC        | Thermal stability and thermal runaway.   | <ul><li>Isotope labelling is needed to distinguish the isotopes.</li><li>Only heat generation is recorded.</li></ul>  | [63,194]                            |
| EIS                | SEI formation;   | <ul> <li>Convolution of electrochemical processes with similar</li> </ul>   | [58,195,196                         |
|                    | <ul> <li>Time-dependent charge-transfer or diffusion-controlled mechanisms.</li> </ul>   | resistance or capacitance;  • Separation of electrode and electrolyte behaviour   | [30,133,130                         |
|                    |  | requires a reference electrode.   |                                     |
| NDP                | <ul> <li>Tracking movement of Li-ions through measuring<br/>the Li content in SE.</li> </ul>   | <ul> <li>NDP is sensitive only to the <sup>6</sup>Li isotopes;</li> <li>Neutron generation and handling on the laboratory scale is difficult;</li> </ul>  | [12,118,197                         |
|                    |  | NDP analysis is time-consuming due to the small neutron fluxes;   |                                     |
|                    |  | <ul> <li>Samples with magnetic properties cannot be tested;</li> </ul>  |                                     |
|                    |  | Special cells are needed during <i>in-situ</i> tests.   | [4.00]                              |
| NMR-MRI            | <ul> <li>3-dimensional spatial tracking of Li filament growth<br/>during cycling, microstructural growth.</li> </ul>                                     | <ul> <li>Imaging dimensions limited to 300μm.</li> </ul>  | [198]                               |
| Optical            | <ul> <li>Morphological evolution: Volume change, crack</li> </ul>  | $\bullet$ Limited resolution ( $\approx 200~nm$ ), only macro-structural  | [14,117,183                         |
| microscope         | and voids formation; • Li-filaments growth;  | changes can be observed.  | [104,199]                           |
| Da                 | Colour change during cycling.  | Considius to montials size and mustaneoutial amendalities   | [200, 202]                          |
| Raman              | <ul> <li>Reaction products at the surface of SE, probing<br/>compatibility of electrode and electrolyte and their<br/>decomposition products;</li> </ul> | <ul> <li>Sensitive to particle size and preferential crystallite orientations;</li> <li>Need to tune the laser specific power to achieve reli-</li> </ul>   | [200–202]<br>[190,203,20            |
|                    | <ul> <li>SEI formation during Li deposition;</li> <li>Phase change and the SOC distribution.</li> </ul>  | able signal-to-noise ratios, whilst avoiding laser-induced sample transformations;  |                                     |
|                    | -  | <ul> <li>Samples must have Raman-active vibrational modes;</li> </ul>   |                                     |
|                    |  | <ul> <li>Proper selection of laser source wavelength, power<br/>and exposure time to optimize the resolution.</li> </ul>  |                                     |
| SEM and EDX        | <ul> <li>Interfacial and sub-surface decomposition, particle<br/>cracking, Li filament formation in the bulk SE.</li> </ul>                              | <ul> <li>Samples must be representative for different<br/>measurements:</li> </ul>  | [114,177,20<br>[15,104,120          |
|                    | cracking, in manneric formation in the burk 3E.  | <ul> <li>Strict operating conditions such as high vacuum and conductive samples;</li> </ul>   | [13,104,120                         |
|                    |  | <ul> <li>High electron energy may damage the sample.</li> </ul>   |                                     |
| SIMS               | <ul> <li>Interlayer formation, possible to follow isotopically<br/>labelled species.</li> </ul>  | <ul> <li>Destructive technique, matrix effects limits the interfacial quantification;</li> </ul>  | [66,206,207<br>[208,166]            |
|                    | abeliea species.   | <ul> <li>Only thin layers near-surface of the sample are accessible;</li> </ul>   | [200,100]                           |
|                    |  | <ul> <li>High energy ion beam may damage the sample and<br/>trigger side reactions;</li> </ul>  |                                     |
| Callal akar        | Communities analysis (C)   | The quantification of SIMS needs standard samples.  Provide interpretable and the control of the control o | [200 240 1                          |
| Solid-state<br>NMR | <ul> <li>Composition analysis of (amorphous) decomposition products at the interface and their impact on</li> </ul>                                      | <ul> <li>Reactive intermediate products could not be captured<br/>in ex-situ experiments;</li> </ul>  | [209,210,15<br>[198,211]            |
|                    | Li <sup>+</sup> transport;  ■ Li microstructural growth and Li <sup>+</sup> dynamics.  | <ul> <li><sup>7</sup>Li is used as the probe nucleus, which may be difficult<br/>to distinguish from the similar Li content in electrodes<br/>and electrolytes;</li> </ul>  |                                     |
|                    |  | • Challenging to separate the resonances from the dif-<br>ferent components and to determine what signal cor-   |                                     |
|                    |  | responds to which part of the cell.   |                                     |
| TEM and EELS       | <ul> <li>Phase change and the formation of disordered interface;</li> </ul>  | <ul><li>Samples must be electrically conductive;</li><li>The sample preparation is complicated due to FIB</li></ul>   | [16,148,201<br>[74,212,213<br>[210] |

TABLE 3 (CONTINUED)

| Techniques | Degradation mechanisms   | Challenges and limitations  | Ref.                   |
|------------|--|---|------------------------|
|            | <ul> <li>Atomic scale structural and chemical analysis;</li> <li>Observation of interfacial chemical and structural<br/>changes, Li filaments formation during cycling.</li> </ul> | <ul> <li>In-situ TEM experiments need special sample holders and fabrication of nano-cells, with an air-sensitive sample transfer.</li> <li>High energy electrons can destroy the sample.</li> </ul>  |                        |
| XPS        | • Ex-situ composition analysis of reaction/decomposi-  | Surface sensitive with shallow detection depth;   | [111,150,201]          |
|            | tion products at the interface; • <i>In-situ</i> observation of SEI formation, onset voltages  | <ul> <li>High energy ion flux during etching process may affect<br/>the chemical component and bring side reactions;</li> </ul>   | [147,214,212]          |
|            | for redox products, SE chemical decomposition pathways (chemical information with time).   | <ul> <li>Li is supplied to the SE surface through physical means<br/>instead of electrochemical cycling during in-situ tests.</li> </ul>  |                        |
| XCT        | <ul> <li>Correlate pores, voids, defects with CCD for Li fila-</li> </ul>  | <ul> <li>Need a synchrotron source;</li> </ul>  | [136,182,215]          |
|            | ment formation; • Interfacial growth and cracking of SE.   | Differentiating between voids (air) and Li metal is challenging;  Leader of the mind accompany to the desired accomp | [20,124,144]           |
| XRD        | • Ex-situ rudimentary studies of chemical stability/compatibility, decomposition products of mix-  | <ul> <li>Lack of chemical component analysis.</li> <li>Sensitive to bulk only, Li has a low electron scattering factor.</li> </ul>  | [193,216,217]<br>[218] |
|            | <ul> <li>ing reactions;</li> <li>In-situ monitoring of local structural changes as a function of current and potential.</li> </ul>   | <ul> <li>During in-situ XRD testing, X-rays may be scattered by<br/>non-targeted materials (such as current collector)<br/>resulting in a decreased intensity and data quality.</li> </ul>  |                        |

 $\dagger$  The list of acronyms and symbols in this work can be found in the Appendix.

#### 3.1.2. Solid electrolyte cracking

Cracks can be formed in the SEs during cycling due to the interfacial decomposition or the growth of Li filaments.

NASICON-type Li conductors (general composition:  $Li_{1+x-y}Al_x^{3+}M_y^{5+}M_{2-x-y}^{4+}(PO_4)_3,$  where  $M^{4+}$  and  $M^{5+}$  are metal ions such as  $Ge^{4+}$  or  $Ti^{5+}$ ) are unstable in contact with Li metal [122]. The electrolyte decomposes to form a new interface (a mixed ionic-electronic conducting interphase) between the electrolyte and the Li metal [123]. For example, Tippens et al. [20] investigated the evolution of mechanical damage within  $Li_{1+x}Al_xGe_{2-x}(PO_4)_3$  (LAGP) by operando Xray Tomography (XCT) (see Fig. 8b). The growth of a decompositon interphase with expanded volume introduce stresses on the electrolyte, resulting in the crack formation. The continuous reactiondriven degradation, rather than the interphase formation itself, was claimed to be the main cause for the observed increase in impedance [38]. Wu and co-workers [124] monitored the morphological dynamics in LPS by Synchrotron Radiation X-ray Tomographic Microscopy (SRXTM). Horizontal cracks within the LPS electrolytes could be observed, which impede the Liion mobility, thus increasing the cell resistance.

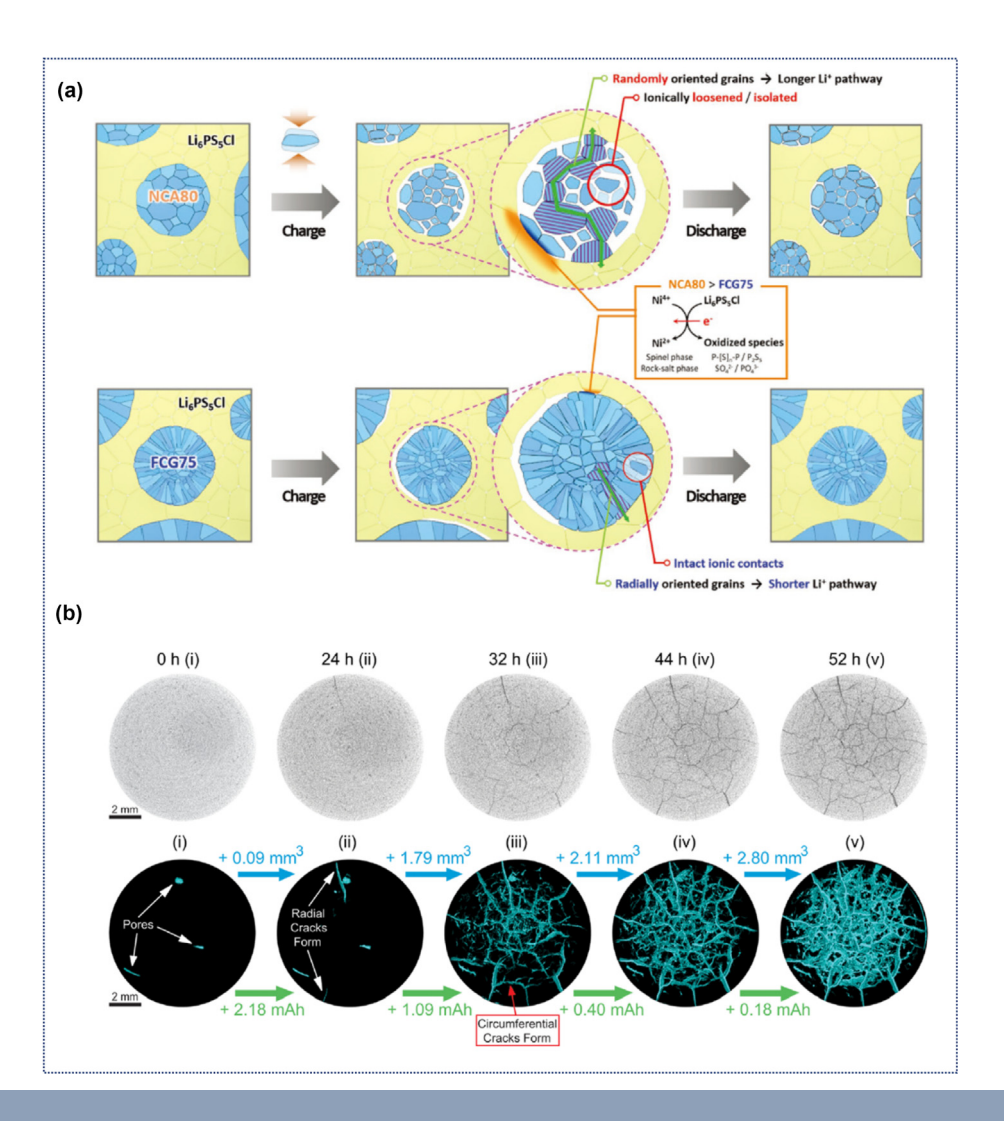
The growth of Li filaments within the electrolytes also introduce severe localised stresses during cycling. Porz et al. [104] studied the Li deposition on four different SEs (LPS,  $\beta$ -Li<sub>3</sub>PS<sub>4</sub>, polycrystalline and single-crystalline LLZTO garnet). Li-plating in pre-existing flaws would produce crack-tip stresses, which drive crack propagation in the SEs. Li et al. [125] directly observed the Li filament growth in LLZTO at the microscale by using *in-situ* NDP. The large volume changes due to Li plating and the mechanical stress would accelerate the crack propagation within LLZTO. However, they found that a well-designed 3D framework of the NE can accommodate the huge volume expansion during Li plating and regulate the Li deposition behaviour to inhibit Li filaments growth. Klinsmann and colleagues [126]

demonstrated *via* modelling that the insertion of Li filaments into pre-existing electrolyte cracks lead to increased pressure, which would lead to further cracking and finally, an internal short-circuit (Fig. 9a).

#### 3.2. Phase change and structural disorder

Many electrodes undergo phase changes during lithiation and de-lithiation, aggravated in solid-state cells due to the sluggish diffusion. Xia et al. [127] demonstrated that disordered LMO would form during cycling in LiPON-based thin-film cells. The formation of disordered LMO could reduce the accessible capacity and increase cell resistance. Subsequently, they developed a 3-dimensional LMO electrode with a vertically aligned nano-wall array architecture, which increases the contact area at the interface and mitigates the formation of disordered LMO. In another study, Jung et al. [114] monitored the phase evolution of FeS<sub>2</sub>/  $\text{Li}_7\text{P}_3\text{S}_{11}$  cells by using *operando* synchrotron X-ray nanotomography. They showed that the pristine FeS<sub>2</sub> phase transforms into the Fe phase, which subsequently penetrates the particle, resulting in a large volume expansion and cracking.

High operating temperatures, overcharge and overdischarge could accelerate the phase changes in electrodes [74,128,129]. Wang et al. [74] used *in-situ* Scanning Transmission Electron Microscopy (STEM) coupled with Electron Energy Loss Spectroscopy (EELS) to elucidate the structural evolution in LCO/LiPON cells under different operating temperatures. As shown by Fig. 9b, when cycled at 80 °C, LCO decomposed into disordered rocksalt phase comprising of cobalt oxide, Li<sub>2</sub>O and Li<sub>2</sub>O<sub>2</sub>. The disordered LCO interphase consumed the AMs and increased the interfacial resistance, reducing the overall capacity and cycle life [74]. In addition, over-delithiation in overcharged batteries is reported to cause the phase transition and structural distortion of PEs in liquid electrolytes [130,131]. During deep overdischarge processes, overlithiation can also trigger phase



(a) Schematic depiction of the structural evolution in the NCA80 and FCG75 PE in all-solid-state cells. Reprinted with permission from Ref. [114], Copyright (2020), John Wiley and Sons. (b) *Operando* X-ray Tomography (XCT) observations of the crack formation within the LAGP SE. Reprinted with permission from Ref. [20], Copyright (2019), American Chemical Society.

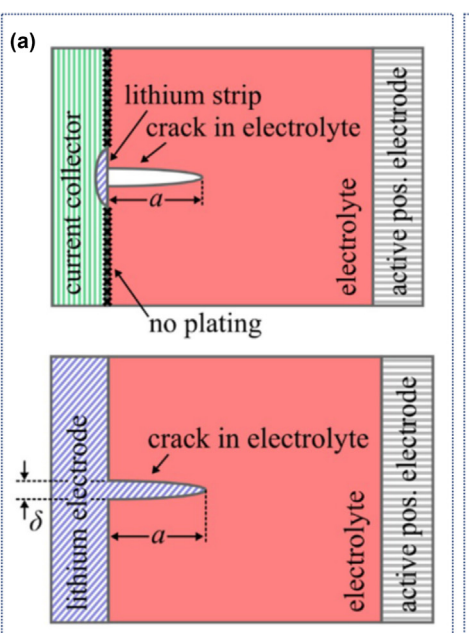
changes and destroy the host structure [132,133]. It was also found that a severe phase change and structure disordering under high potential in Ni-rich NMC PE would accelerate the gas release  $(O_2)$  from the NMC lattice [134,135].

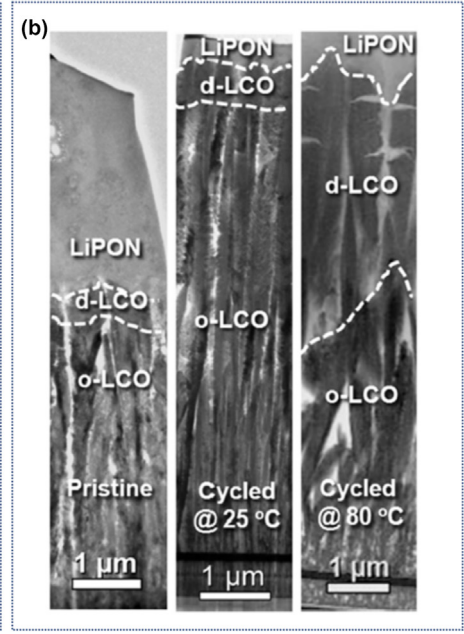
## 3.3. Creep behaviour of Li metal

The unique mechanical properties (elastic, plastic and creep properties) of Li metal greatly influence Li metal's dynamic evolution during cycling under different operating conditions. The term creep describes the material behaviour to exhibit continuing deformation even though the stress is held constant [107]. The creep characteristics can be divided into three regions: primary creep, in which the material hardens and the creep-rate diminishes with time; secondary creep or steady-state creep, in which the hardening and softening mechanisms counteract to cause a constant creep rate; and tertiary creep, where the material softens until creep failure occurs [107].

Although the permanent plastic deformation usually occurs above the yield strength, deformation can also occur below the yield strength for metallic Li [21,101]. Due to the high homolo-

gous temperature of Li, Li exhibits temperature, strain-rate and pressure-dependent creep behaviour [101]. Therefore, the deformation of Li at stresses below the yield strength is caused by both elastic and creep strains [101]. Although the creep behaviour of Li metal is aggravated under high operating temperature, creep was also observed to be the dominant deformation mechanism over a wide range of temperature conditions (248K - 398K) [101]. While a high external stack pressure such as 5MPa is necessary to reduce voids and interfacial contact losses (see Section 3.5), Li creeps through the pores and grain boundaries of the SE to induce the propagation of Li filament if the stack pressure becomes too high. Doux et al. [136] showed that the cell shorted mechanically before cycling began when a high stack pressure of 75MPa was applied. The problem of Li creep becomes more critical if the relative density of the SE is low and the porosity of the SE is high [136]. Under high external pressure, Li creeps and flows through the pores and grain boundaries of the SE, forming an electronic percolation between the NE and the PE to cause an eventual internal short-circuit [136,137]. Due to the low yield strength of polycrystalline bulk Li metal (0.6MPa





(a) A SE analytical model predicts the stress propagation due to the growth of Li filaments. Reprinted with permission from Ref. [126], Copyright (2019), Elsevier. (b) The formation of disordered phases between LCO and LiPON. Reprinted with permission from Ref. [74], Copyright (2016), Elsevier.

- 0.8MPa) [21], a low stack pressure such as 5MPa could already trigger the Li creep behaviour [136]. However, as discussed in Section 2.3, it should be noted that the local mechanical properties of Li metal such as the CRSS and yield strength can be very different from that of the bulk polycrystalline Li metal [95]. Although the external stack pressure is higher than the yield strength of the bulk polycrystalline Li metal, the difference between the local and bulk mechanical properties of Li metal may account for the stability of Li metal under the DC cycling with an external stack pressure of 5MPa.

### 3.4. Electrode-electrolyte interfacial decomposition

In contrast to the widely-perceived idea of excellent stability of SEs [36,138], most of the SEs studied have a limited intrinsic electrochemical stability and are predicted to form thermodynamically favourable decomposition interphases either at low or high potentials (see Fig. 10f) [59,60]. In this section, we briefly describe the interfacial decompositions at the NE-SE interface, SE-PE interface and the decomposition due to carbon additives. The reader is directed to other, more comprehensive reviews on the topic of interfaces in all-solid-state batteries [36–38].

#### 3.4.1. Negative electrode - solid electrolyte interface

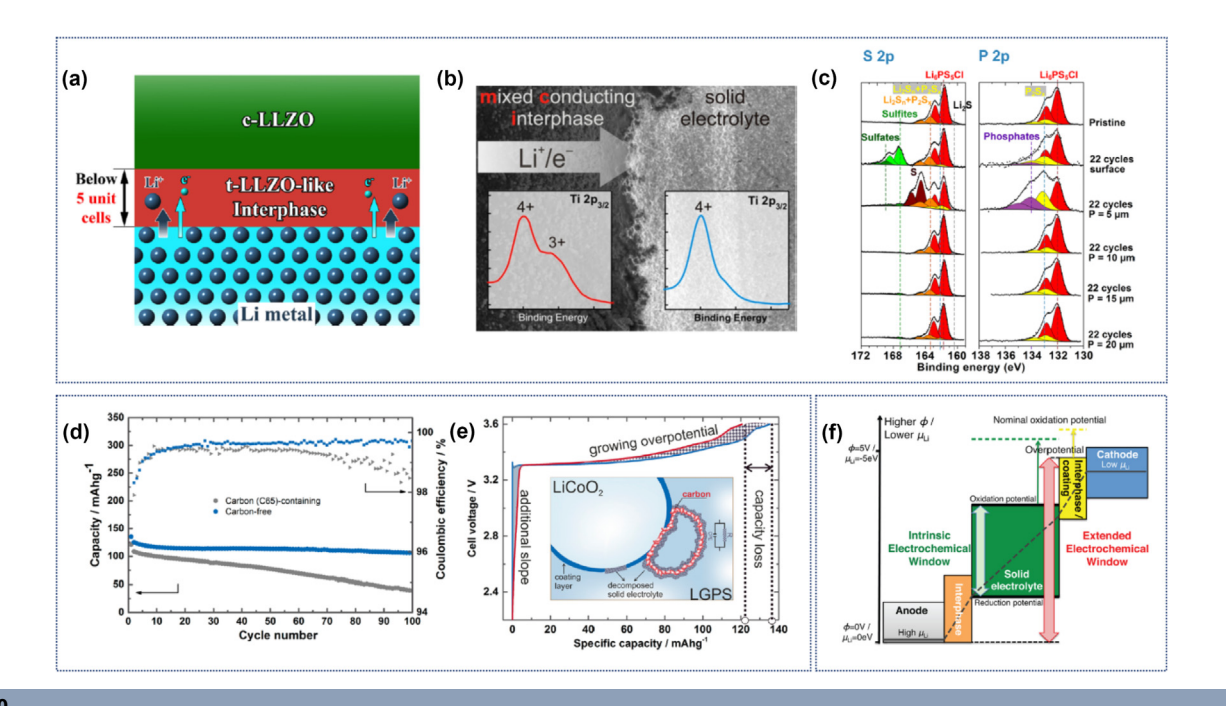
Although the use of Li metal as the NE could improve the energy density in solid-state cells, its strong reduction potential can cause interfacial reactions at the electrode–electrolyte interface [122]. In principle, there are three different types of interfaces classified as (1) interphase layers of mixed ionic and electronic conductors (MCIs), (2) stable interfaces with negligible decomposition, and (3) ionically conductive but electronically insulating interphase layers [60,122].

In contrast to the second and third types of interface, MCI is unstable (both thermodynamically and kinetically). In this type

of interface, both Li and electronic conductivity lead to continuous decomposition reactions at the electrode-electrolyte interface [122]. For example, amongst the NASICON-type SEs, all members of this class are unstable in contact with Li metal. As shown by Fig. 10b, the high valent state ions Ti<sup>4+</sup> and Ge<sup>4+</sup> can be reduced by Li metal to form a degradation interfacial layer, which decreases the Coulombic efficiency, increase the impedance and cause a capacity decay [16,60,142,146]. The decomposition interface layer comprises a mixture of Li<sub>2</sub>O, Li<sub>2</sub>O<sub>2</sub>, Li<sub>2</sub>CO<sub>3</sub> and the electronically conductive Ti<sup>3+</sup> and Li-Ge alloy, which demonstrated mixed electronic and ionic conductivity [60,146]. LGPS can also form an MCI in contact with Li metal. The decomposition of LGPS leads to the formation of an interface composed of Li<sub>2</sub>S, Li<sub>3</sub>P and Li-Ge alloy, leading to a further continuous detrimental decomposition of the SE owing to the mixed electronic-ionic conductivity of the interphase formed [147].

In the second type of interface (*e.g.*, stable interfaces with negligible decomposition), the SEs are thermodynamically and kinetically stable during cycling. However, due to the limited electrochemical window and the compatibility of the electrolyte/electrode interfaces, it is unrealistic to develop an intrinsically stable interface without decomposition over the entire cycling voltage range [122]. For example, LLZO is reported to have excellent stability against Li metal. Instead of triggering interfacial decomposition, the surface of cubic LLZO is slightly lithiated and undergoes a phase transition to its tetragonal phase (less than five cubic LLZO unit cells thick) when contacting the Li electrode (see Fig. 10a) [148].

As for the third ionically conductive but electronically insulating interface, decomposition happens spontaneously but not continuously as in the MCI interface. Once formed, the electrochemically insulating interphase layer passivates the electrolyte interface and remains stable during the further electrochemical



(a) The formation of the t-LLZO-like interface (Reprinted with permission from Ref. [148], Copyright (2016), American Chemical Society). (b) The reduction of  $\mathrm{Ti}^{3+}$  in the NASICON-type SEs and the resulting formation of the MCls. Reprinted with permission from Ref. [146], Copyright (2013), American Chemical Society. (c) Interfacial stability of  $\mathrm{Li}_6\mathrm{PS}_5\mathrm{Cl}$  toward NMC333. Reprinted with permission from Ref. [149], Copyright (2017), American Chemical Society. (d) Cycling performances with and without carbon additive in an all-solid-state cell consists of LGPS and LCO. (e) Illustration of the decomposition interaction between LCO and LGPS. Reprinted with permission from Ref. [111], Copyright (2017), American Chemical Society. (f) DFT calculation of the electrochemical and chemical stability of the SEs. Reprinted with permission from Ref. [59], Copyright (2015), American Chemical Society.

cycling [122]. When LiPON is exposed to Li metal, a chemical reaction occurs and LiPON decomposes to form an interphase consisting of Li<sub>3</sub>PO<sub>4</sub>, Li<sub>3</sub> P, Li<sub>3</sub>N and Li<sub>2</sub>O [150]. However, the reaction is intermittent, and the disrupted LiPON interface region is thin enough to allow the continuous migration of Liions, as well as being poorly electronically conducting. This characteristic demonstrates the high cycling stability of solid-state cells using LiPON, caused by the formation of this kinetically-stabilising layer [151–153].

Although the exact nature of the reaction products at the interface is difficult to predict, due to the interplay of thermodynamic and kinetic factors, computational methods have been useful in determining possible decomposition pathways, revealing trends in chemical reactivity, providing limits for electrochemical stability windows and guiding engineering of interfaces [38]. Three approaches have been adopted to evaluate the electrode-electrolyte interactions using first-principles methods: (1) electrochemical stability, (2) topotactic stability which provides the maximum voltage limits or widest electrochemical stability window in which there is maximum kinetic stabilisation and (3) chemical mixing reactivity [38,59,61,60,154,155]. Explicit interface calculations assess energetics of interfacial species directly by using DFT on supercells. A structural-relaxation method optimises the atomic coordinates at the interface but cannot account for any activated processes, such as atomic diffusion or the nucleation of new solids [38]. This type of simulation has a high computational cost and typically only captures the dynamics of the system at elevated temperatures and limited time scales (< 1 ns) [9,10,38].

Engineering of Li/SE interfaces has been pursued in the community in order to mitigate the aforementioned interfacial effects [156]. For example, alloying of the Li NE has been explored, both to improve the Li diffusion coefficient (e.g. the Mg-Li alloy studied by Krauskopf et al. [157]), and to improve the chemical stability for the interface, such as Li-In used with thiophosphate-based electrolytes [32,157,158]. In the latter case, the Li-In alloy acts to raise the voltage of the NE material and reduce the volumetric strain on the metal [158]. Requirements for interlayer coatings include chemical and electrochemical stability with both the SE and electrode over the voltage range for the relevant electrode [9,10,38,159]. Introduction of artificial SEI through physical [151,160], chemical [161] and electrochemical methods [162] is also an effective strategy to minimise the side reactions between Li metal and SE. Examples include the use of interlayers to act either as buffer layers preventing the reduction of SEs by alkali metals or used as mediators to improve wetting between two phases and subsequently lead to a reduction in Li filaments formation. For example, the use of binary layers such as LiF, Li<sub>2</sub>O, Li<sub>2</sub>S, Li<sub>3</sub>N and Li<sub>3</sub>P have been used as protective layers because of their intrinsic stability against Li metal [9,10,163,164].

#### 3.4.2. Solid electrolyte - positive electrode interface

Due to the strong oxidation of the transition metal species under high potential in the charged state, the interface between the PE and the SE is more complicated. The interactions between PEs and SEs include mutual diffusion of elements and the resulting phase change, the electrolytes decomposition and growth of interphase. Sakuda et al. [165] studied the LCO/LPS interface using TEM and EDX. The mutual diffusion of Co, P, and S elements on the interface was confirmed by EDX mapping. High-resolution TEM results revealed the growth of an interfacial layer between LCO and LPS after the initial charge process. Park et al. [139] investigated the elemental diffusion on the LCO/LLZO surface by Time of Flight - Secondary Ion Mass Spectrometry (ToF-SIMS). Three-dimensional elemental distribution revealed that Co migrated into the LLZO while the La/Zr migrated to the LCO PE during high temperature processing. The resulting formation of the tetragonal LLZO phase at the SE/PE interface, therefore, deteriorated the electrochemical properties.

In high performance batteries, layered PEs such as NMC and NCA have attracted great interest due to their high capacity. However, solid-state batteries using NMC or NCA PEs show a low Coulombic efficiency and a poor cycle stability [113,149,166]. In addition to the mechanical volume changes and resulting particle cracking and contact-loss (as discussed in Section 3.1.1), the interfacial side reactions and the growth of decomposition layer could also cause severe performance degradation. Koerver et al. [113] investigated the stability of thiophosphate-based SEs (Li<sub>3</sub>PS<sub>4</sub>) against NMC-811. The results of in-situ XPS indicate the polymerisation and possible formation of  $\text{Li}_2\text{P}_2\text{S}_6$ ,  $\text{Li}_4\text{P}_2\text{S}_7$  and  $\text{Li}_4\text{P}_2\text{S}_8$ .

The argyrodite electrolyte,  ${\rm Li_6PS_5Cl}$ , has been reported to possess a high ionic conductivity and an ease of processing. Auvergniot et al. [149] studied the interfacial stability of  ${\rm Li_6PS_5Cl}$  against NMC-333, LMO and LCO by using Auger electron spectroscopy and XPS.  ${\rm Li_6PS_5Cl}$  was oxidised to form elemental sulfur, Li polysulfides, phosphates, LiCl and  ${\rm P_2S_x}$  (x > 5) (see Fig. 10c). By using ToF-SIMS, Walther et al. [166] observed the interfacial decomposition of NMC-622/Li<sub>6</sub>PS<sub>5</sub>Cl. A Cathode Electrolyte Interphase (CEI) layer of at most 10 nm thickness was observed to have formed by the interfacial reaction between NMC-622 and  ${\rm Li_6PS_5-Cl}$  electrolyte. This CEI layer consisted of phosphate- and sulfate like species. Surface coating of the PE materials with different protecting layers, such as  ${\rm LiNbO_3}$  [167,168],  ${\rm Al_2O_3}$  [169],  ${\rm Li_3PO_4}$  [170] and  ${\rm Li_{3-x}B_{1-x}C_xO_3}$  [171], was shown to effectively reduce the side reactions.

#### 3.4.3. Instability of carbon additives

Composite electrodes of solid-state batteries typically consist of AMs, solid electrolytes and carbon additives such as acetylene black. The electronically conductive carbon additives were shown to have both have positive and negative impacts on the rate performances and lifespan of solid-state batteries. Mizuno et al. [172] proposed that the addition of acetylene black was effective in decreasing the resistance of the LCO/LPS based solid-state cells. Many factors such as component proportion, morphology and specific surface of the carbon additives could affect the battery performances. Vapour-grown carbon fibre [173,174] and multiwalled-carbon-nanotubes [175] were found to enhance the capacity by constructing a continuous and long-range conducting path for electronic diffusion. Strauss et al. [176] investigated the specific surface of carbon additive and the relative battery performance. Low BET surface material such as Super C65 carbon black could enhance the cyclability of NMC-622/thiophosphate-based bulk type solid-state cells

compared to Ketjenblack and carbon nanofibers with a higher specific surface [176].

While conductive carbon additives improve the kinetics and rate capacity, side reactions such as electrolyte decomposition also occur and cause cell degradation (Table 2). Oh et al. [177] investigated the interfacial phenomena between LiNi<sub>0.5</sub>Mn<sub>1.5</sub>O<sub>4</sub> PEs and a sulfide electrolyte (LGPS). According to their research, electrochemical decompositions of LGPS continuously occur at the LGPS/acetylene black interface above 4.5V (vs. Li/Li<sup>+</sup>) that cause an irreversible capacity loss. A similar interfacial issue was also found in LCO/LGPS based solid-state batteries, in which both acetylene black and Super P were shown to aggravate the oxidation of LGPS by forming inactive species on the electrode/electrolyte interface. The inclusion of carbon additives was shown to produce faster electronic percolation paths in a composite PE. In the case of LGPS SE, carbon facilitates the oxidation from S<sup>2-</sup> to S<sup>0</sup> (insulating polysulfides), which accumulate at the interface and isolates the Li<sup>+</sup> conduction pathway (see Fig. 10d and Fig. 10e) [111]. A limited ionic transport in the composite PE ultimately causes an increasing interfacial resistance and a faster capacity fade [111,178]. Therefore, the development of more suitable carbon additives with an optimum balance between improving the rate performance and causing minimum degradation impacts are crucial to enhance the overall cell performances in different solid-state batteries.

#### 3.5. Surface voids and interfacial delamination

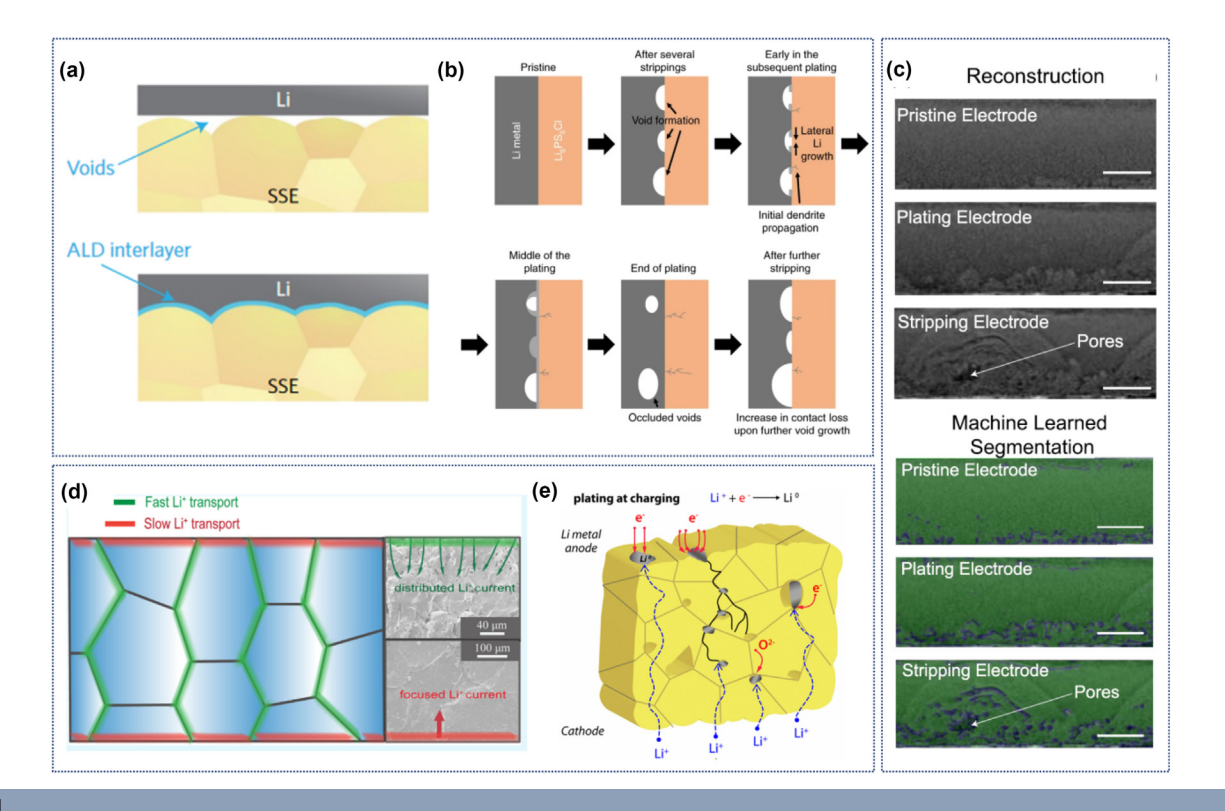
The rigid nature of the SE and the low wettability at both interfaces have been identified as primary reasons causing the formation of voids during the fabrication of cells (Fig. 11a) [9,179]. Beside the pre-existing surface flaws, voids could form in *operando* under high current densities during the Li stripping process [13]. Fig. 11 illustrates the mechanisms of voids formation at the SE-NE interface. If the applied current densities exceed CCD, the initial interfacial voids lead to the formation of occluded voids and the increase of contact loss after further stripping and plating (Fig. 11b) [13].

Han et al. [9] studied the interfacial resistance of the  $\text{Li}_7\text{La}_{2.75}\text{Ca}_{0.25}\text{Zr}_{1.75}\text{Nb}_{0.25}\text{O}_{12}$  (LLCZN)/Li metal electrode interface. The voids between the Li metal and the SEs were shown to reduce the surface contact and increase the resistance, creating a build-up of the overpotential and a drop in the cycle life. In addition to the poor contact, the flaws and voids at the interface also act as active sites, where localised high current density and mechanical pressure initiate, triggering the growth of Li filaments and short-circuit problems. For bulk SEs, microstructural features such as pores and grain boundaries cause an inhomogeneous contact at the interfaces and within the SE (Fig. 11e). As a result, the rate of Li migration across the SE becomes non-uniform, which further promotes the nucleation of Li filaments [7,15,32].

Based on the linear-elastic fracture mechanics

$$\sigma_{\rm st} \geqslant \frac{K_{\rm Ic}}{\gamma \sqrt{\pi a_{\rm c}}},$$
 (7)

Porz et al. [104] developed an analytical model to study the effects of surface flaws on the Li electrodeposition in the SEs. Due to a lower sur-



(a) Illustration of voids formation due to processing (Reprinted with permission from Ref. [9], Copyright (2017), Nature Materials) and (b) during electrochemical stripping and plating above CCD. Reprinted with permission from Ref. [13], Copyright (2019), Nature Materials. (c) A combined *In-situ* tomography imaging technique with machine learning computational method to track pores formation at the Li—SE interface. Deep convolution neural network was trained on 800 images from one electrode and tested on additional 200 images from the same electrode to achieve a high confidence segmented image. Reprinted with permission from Ref. [180], Copyright (2020), American Chemical Society. (d) Grain orientations and grain boundary distribution within LLZO. (Reprinted with permission from Ref. [7], Copyright (2015), American Chemical Society) (e) The reduction of the Li<sup>+</sup> to Li<sub>0</sub> owing to the electronic conductivity of the SEs (Reprinted with permission from Ref. [15], Copyright (2017), American Chemical Society).

face overpotential, they showed that Li deposits preferentially in the pores and cracks of the SE. In the presence of pre-existing flaws, they showed that the critical overpotential threshold is low for cracks to propagate in the SE. However, Swamy et al. [105] showed later that Li filaments initiate favourably at the edges of the working electrodes, even when more significant surface defects are present near the edges. By correlating the optical microscopy observations with an electrochemical model, they showed that a stronger electric field causes the preferential initiation of Li filaments at the working electrode perimeters.

Tian et al. [108] modelled the effects of imperfect contact areas in the film- and bulk-type solid-state cells. The exchange current density at the PE interface was modified to include a contact factor ( $\gamma_c = A_{\rm imp}/A_0$ ), where  $A_{\rm imp}$  is the imperfect contact area and  $A_0$  is the perfect contact area. They showed that the contact area loss causes local Li concentration accumulation at the interface and reduces the cell's accessible capacity. In another study, using the cohesive theory of fracture, Bucci et al. [22] formulated an analytical model to investigate the delamination of the electrode from the electrolyte. If the yield stress of the SE is lower than the interfacial cohesive strength, the plastic deformation of the SE occurs, which can prevent the delamination. Recently, Dixit et al. [180] used monochromatic, high-energy X-rays to capture low-density phases (voids and Li metal) in a Li-LLZO-Li model system. As quantification of the microstructural properties requires a consistent segmentation procedures and the conventional thresholding methods could not segment the phases reliably in this case (Fig. 11b), deep convolution neural network was employed to obtain a high confidence segmented image (Fig. 11c) [180]. To mitigate surface voids and interfacial delamination, applied stack pressure and surface engineering strategies such as polishing the electrolyte surface with physicochemical methods, optimising the electrode structure with different size of electrolyte, coating protection or wetting layers should be developed [7,9,10,13,32,136,151].

High pressure such as 25 MPa (often accompanied by an elevated temperature) can be applied during cell fabrication to initially contact all components in a Li metal-containing cell [37]. The initial pressure used depends on the mechanical properties of the SE and the AMs, as well as the interfacial wetting properties with the Li NE [136]. If the stack pressure is increased from 3 MPa to 5 MPa during cycling, a sufficient contact during the lithiation and delithiation can be achieved to ensure a stable stripping and plating [37,136,181]. Doux et al. [136] investigated the effects of stack pressure on the degradation mechanism of Li metal/Li<sub>6</sub>PS<sub>5</sub>Cl solid-state cells. High-resolution XCT was employed to monitor the structural evolution of Li filaments during cycling. The interfacial resistance decreases under high stack pressure due to improved contact. Wang et al. [56] demonstrated that the stack pressure has dynamic effects on the overpotential required to cycle Li at constant current densities. Critical stack pressure was correlated to the overpotential, below which a significant voltage loss was observed.

#### 3.6. Li filamentary nucleation and growth

Li metal undergoes significant volume changes and is prone to interfacial instability, resulting in Li filament growth and interfacial reaction/delamination during electrochemical cycling. The accumulation or depletion of surface concentration at the interfaces can create an excess charge and induce instabilities (e.g., Li filaments). By using operando video microscopy, Kazyak et al. [14] identified four different types of Li-filaments in LLZO: branching, straight, spalling and diffuse filaments. Many experimental and theoretical efforts had been devoted to revealing the causes leading to the Li-filaments formation, which include:

- (1) **Discontinuous interfacial contact and inhomogeneous ionic flux.** As discussed in Section 3.5, both the processing as well as the cycling conditions would introduce voids (see Fig. 11a and Fig. 11b) [9,13,14], increase the porosity [182], or cause surface defects [183]. In addition, the Li metal shows poor compatibility with some SEs. These physical properties introduced heterogeneous ionic flux and distribution within these limited spaces, which increase the local electric driving force and become the "hotspot" for preferential Li filamentary growth [183]. To further achieve a sufficient interfacial contact, different strategies such as cleaning the surface of Li metal and the SE [10,184], applying appropriate stack pressure [56] and introducing soft interlayers [9,159] have been proposed.
- (2) **Grain boundaries.** Grain boundaries were also reported as the preferential sites for the penetration of Li-filaments (Fig. 11d) [7,185,186]. The grain boundaries situation is far from simple and depends on numerous factors, including mechanical and transport properties.
  - The mechanical properties of the grain boundaries differ from the grain interior, which can lead to filament propagation if they have a lower elastic modulus than the grain interior. It is possible that stress can be alleviated in certain SEs as Li is deposited along grain boundaries, preventing cracking of the SE. Furthermore, as the grain boundaries have high surface energy, they can have a lower stiffness than the grain interior. They have been found to have a 50% lower shear modulus [187], which can mean they fall under the criteria for Li filaments formation according to the Monroe-Newman model [102]. Regarding the ionic conductivity of grain boundaries, in materials with a higher grain boundary conductivity, Li might be expected to accumulate more quickly in the grain boundaries than the grains, resulting in a limit for the CCD. However, it is mostly unclear whether the grain boundary conductivity exceeds that in the grains in many systems, in part due to difficulties in characterising the grain boundaries experimentally and potentially substantial differences in the conductivity depending on the synthesis and processing parameters. For example, in the case of LLZO, Ga-doped LLZO was shown to tolerate higher current densities than Al-doped LLZO, where Al-LLZO was shown by ToF-SIMS to contain both Al and Li, while Ga-LLZO contained only Li [188], even though the grain boundary conductivity was reported to be higher in Ga-LLZO. This report also

demonstrated a preferential growth of Li filaments along grain boundaries even when the grain boundary conductivity is lower than in the bulk material.

On a related note, the grain boundary reactivity may also play a role - the preferential reaction of grain boundaries in e.g., LLZO to form LiOH and Li<sub>2</sub>CO<sub>3</sub> [66] may further exacerbate an inhomogeneous contact of the surface of the SE with Li metal, altering the inherent mobility/flux of Li across this interface. There are contrary reports regarding the effect of grain size - Sharafi et al. [189] reported that the CCD increased with increasing grain size in LLZO - this was attributed to the increased effective contact area between Li metal and the grain instead of the grain boundaries. However, Cheng et al. [190] showed that the CCD increased as the grain size is reduced, which was attributed to the larger area fraction of grain boundaries. It is possible that differences in the grain boundary structure, orientation and composition as a result of different synthesis protocols even with the same nominal SE could be responsible for these different observations. In fact, it has been suggested that the difference in interfacial energies of grain boundaries and of the SE/Li interface will dictate the propensity for filaments to form preferentially along grain boundaries [33].

(3) **Electronic conductivities.** High electronic conductivities introduced Li filaments formation within the SEs. LLZO and Li<sub>3</sub>PS<sub>4</sub> have high electronic conductivities, thus electrons and negative charges could be trapped within the bulk SE, causing the reduction of Li<sup>+</sup> to Li<sup>0</sup> and initiating the formation of Li filaments within the SE (Fig. 11e) [12,15]. An empirical criterion was further demonstrated, which shows that the electronic conductivities of SEs should be lower than 10<sup>-10</sup> S cm<sup>-1</sup> and 10<sup>-12</sup> S cm<sup>-1</sup> for a filaments-free Li plating at 1 and 10 mA cm<sup>-2</sup>, respectively [12]

Barai et al. [191] studied the impacts of external pressure and electrolyte transport properties on the Li filamentary growth via an electrochemical-mechanical coupled model. By modifying the Butler-Volmer's expressions derived by Monroe and Newman [102], they showed that the minimum pressure required to suppress Li filaments' growth depends strongly on the current densities and elastic moduli of the SEs. They also found that increasing the electrolyte conductivity and transference number can reduce Li filamentary growth [191]. In a subsequent electrochemical-mechanical coupled model [185], they modelled the growth of Li filaments through the SE microstructure. Due to the lower Young's modulus of the grain boundaries versus the grain interiors by two orders of magnitude, they predicted higher effective stressinduced current density at the grain boundaries. The stress-induced current densities were shown to further cause an accumulation of strain energy that induces crack formation in the SE [185]. These studies show that filament growth can preferentially occur at the grain boundaries even when they have a lower ionic conductivity than the grain interior. Both microstructural and chemical inhomogeneities play a role in the electrochemical–mechanical formation of such Li filamentary growth (Table 2) [188]. While many efforts have been devoted to developing SEs with high ionic conductivity, the electronic conductivity should also be considered as another critical criterion for high-performing solid-state batteries. Surface engineering strategies such as doping and thin coatings have been developed to decrease the electronic conductivity [219,220]. The creation of compressive stress at the surface of the SE has been suggested to reduce stress-induced Li filament penetration by Qi et al. [106] with ion implantation.

Fundamental analysis of various materials behaviours and the multiphysical interactions between different cell components is essential to overcome the degradation challenges in solid-state batteries. The investigation of solidstate batteries involving multiscale and multiphysical material characterisations include: (1) intrinsic properties such as crystal structures, electronic conductivity, ionic conductivity and electrochemical windows; (2) morphological and structural evolution (e.g., grain boundaries evolution, volume change, particles cracking); (3) reaction between different cell components and the resulting chemical analysis of the elemental distribution; (4) gas formation; (5) thermal stability and runaway; (6) pores tracking and Li filaments formation. Different multiscale advanced characterisations techniques have been employed to gain insights into the complex multiphysical mechanism. Table 3 summarises diverse advanced characterisation methods, both in-situ and ex-situ, in solid-state battery research. As there have been several reviews discussing these working principles [37,221], we only outline the applications of these methods in solid-state batteries and list their limitations as well as challenges.

## 4. Solid-state physics and cell architecture engineering

There are three different types of solid-state cells in terms of cell architecture: planar thin-film, three-dimensional interdigitated and composite solid-state cells. Fig. 12a shows the schematic of the planar thin-film cell, in which the electrodes are fabricated into a thin, non-porous layer [48,222]. The electrochemical reactions take place at the planar surface between the SE and electrodes. However, the energy per unit area of planar thin-film cells is insufficient to meet the power demands of micromachined sensors and actuators [224]. Fig. 12b shows the SEM micrographs of the interdigitated three-dimensional solid-state cells, where the cell components are fabricated in an array of three-dimensional columns [223]. Due to a shorter mass transfer transport distance and a larger electrode surface area per footprint area, the interdigitated electrodes in the fully conformal three-dimensional configuration show promise to meet the required energy per unit area [224,225]. In contrast, a composite electrode is typically made of three components, which include AMs, SEs and electronic conductive agents such as carbon black [25,47,62]. The AMs and carbon black act as the electronic conducting phase whereas the SE in the composite cell is the ionic conducting phase [47]. The composite solid-state cell can use

either metallic Li or composite electrodes as the NEs, as shown in Fig. 12(c1) and Fig. 12(c2), respectively [5].

#### 4.1. Thin-film solid-state cell

In this section, we review the solid-state physics of different cell components such as the Li NE, SE, non-porous PE and the space-charge formation at both interfaces on the overall thin-film cell behaviour.

#### 4.1.1. Low melting temperature of Li metal

Thin-film solid-state cells have a low capacity in the range of µAh and mAh [48,226]. Potential low power density applications for these cells include micromachined sensors and actuators, implantable medical devices and smart cards [224]. Some of the electronic circuit boards are manufactured with the solder reflow assembly, in which the integrated circuits are heated to 250°C for a short time, and all the components are soldered simultaneously [226,227]. Under this solder reflow manufacturing condition, thin-film solid-state cells using pure metallic Li as the NEs fail due to the low melting temperature of metallic Li (180°C) [226,227]. The molten Li metal could penetrate through the grain boundaries of the SE and cause an internal short-circuit. As a result, compounds which alloy with Li have been proposed to replace the pure metallic film as the NE [223,228,229]. However, the delithiation of these compounds could cause a significant volume change up to 4.07 times of the initial volume and a significant irreversible capacity loss during the first cycle [228].

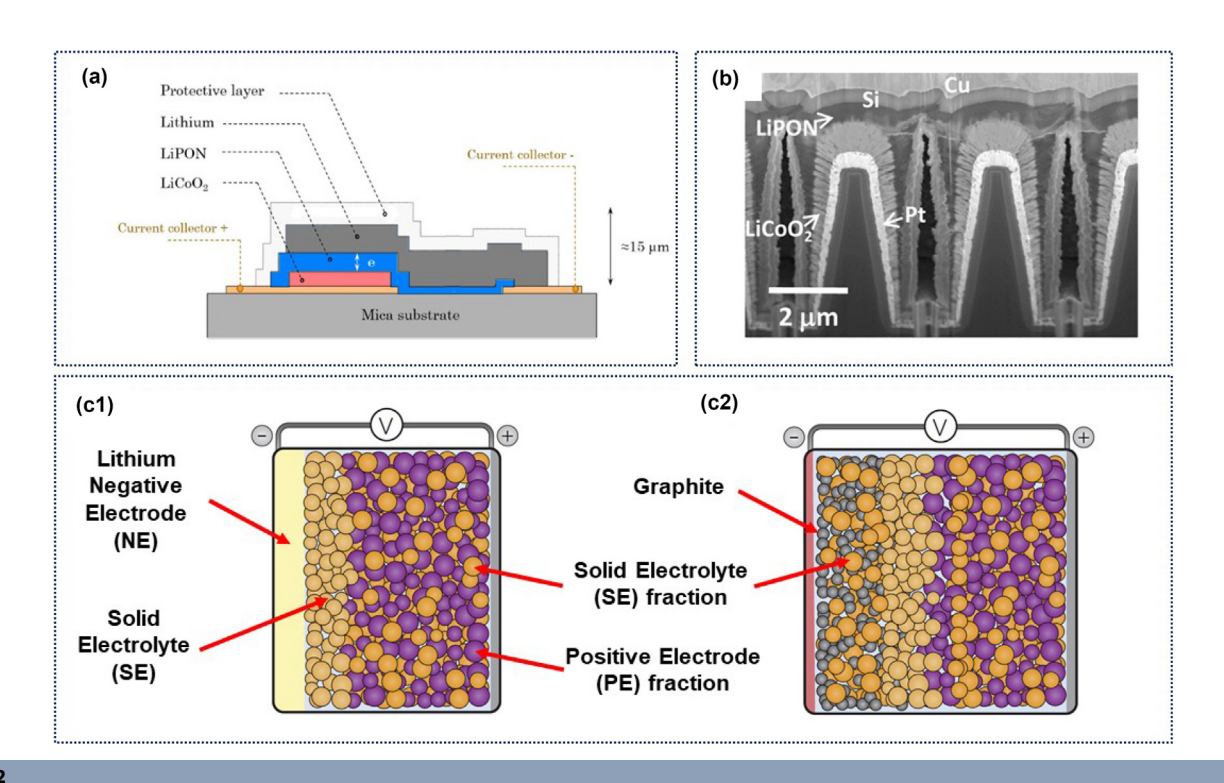
Another feasible solution to address the high solder reflow temperature is the fabrication of a NE-free thin-film cell (Cu—SE—LCO) [226,227]. In this configuration, a copper current collector is deposited over the electrolyte in place of the NE [226]. As a result, the NE-free cell can be soldered onto the Si wafers and integrated directly into the electronic circuit boards before the electrochemical cycling [227]. Li from the LCO is then plated between the copper current collector and SE on the initial charge [226]. One drawback of this cell configuration is that its cycle stability requires a gastight seal provided by an overlayer, such as parylene to reduce the partial pressure of oxygen and moisture. Without an overlayer, half of the reversible capacity was reported lost during the initial cycle due to the formation of Li<sub>2</sub>O and LiOH [227].

## 4.1.2. Conduction mechanism in the bulk solid electrolyte

For all types of cell architecture shown in Fig. 12, a thin-layer of bulk SE is used as the separator and ionic conductor between the NE and the PE. An inorganic SE can be considered as a single-cation ionic conductor when the mobility of the anion is negligible [230]. In the case of LiPON SE, Yu et al. [17] postulated that the oxygen, nitrogen and phosphorus atoms are rigidly bound in the framework structure of LiPON. The single-cation ionic conductance feature can be verified by the measurement of cationic transference number on a non-blocking symmetrical cell (Li—SE—Li) as follows [231]:

$$T^{+} = \frac{I^{s} (\Delta V - I^{0} R_{1}^{0})}{I^{0} (\Delta V - I^{s} R_{1}^{s})}.$$
 (8)

The transference number for the inorganic SE is often considered as near-unity [44,232]. Conventional liquid electrolytes such as those based on LiPF<sub>6</sub> salts have a transference number between 0.3-0.5



(a) Schematic of the planar thin-film solid-state cell. Reprinted with permission from Ref. [222], Copyright (2015), The Electrochemical Society. (b) Cross-sectional Scanning Electron Microscopy (SEM) image of the interdigitated three-dimensional solid-state cell. Reprinted with permission from Ref. [223], Copyright (2016), American Chemical Society. (c1) The composite solid-state cell with metallic Li film (light yellow) as the NE. (c2) The solid-state cell using composite electrodes as both the PE and NE: Grey circles in the NE represent graphite; dark orange circles denote the SE fractions in both composite electrodes and violet circles in the PE represent a layered transition metal oxide. Lighter orange circles in the electrolyte denotes a different SE than the SE used in the electrodes. Reprinted and adapted with permission from Ref. [5], Copyright (2016), Nature Energy.

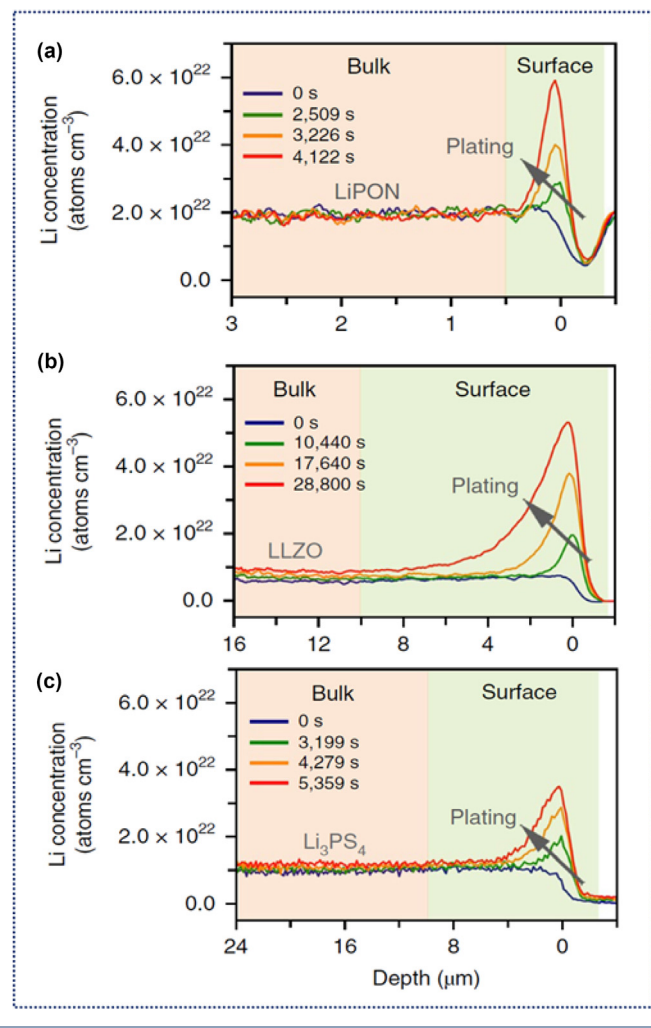
[233,234]. A low transference number implies that mobility of anions in the electrolyte and their accumulation at the electrode surface cause the concentration gradients of Li-ions in the SE, which creates a concentration overpotential that subsequently limits the cell performance [58,235]. While a near-unity transference number in the inorganic SE can reduce the amount of heat generated in the SE, all other processes described in Section 2.2 still generate a considerable amount of heat. Han et al. measured the concentration of Li-ions in the bulk SE for LiPON, LLZO and amorphous Li<sub>3</sub>PS<sub>4</sub> using the time-resolved *operando* NDP method. All three different SEs exhibit constant concentration profiles in the bulk electrolyte at different times during Li plating (Fig. 13) [12]. A near-zero concentration gradient shows that the migration of Li-ions due to the hopping of Li-ions from one site to the neighbouring site is the primary conduction mechanism in the bulk SE [58].

#### 4.1.3. Space-charge formation at the interface

At the interface between the electrode and the electrolyte, a space-charge region with two oppositely charged layers is formed due to the difference in the chemical potentials of the electrodes and the SE [71]. As illustrated by Fig. 13 and 14a, the accumulation or depletion of the charged species at the interface causes the surface concentration of the species to deviate from the bulk concentration and the formation of a local electric field at the interface [72]. Due to variations of surface concentration and local electric potential at the interfaces, the space-charge layers are non-electroneutral [72,236–238]. The characteristic length scale of the space-charge layers can be estimated from the Debye lengths. Wan and Ciucci showed that the Debye length of the NE

at the NE-SE interface is 9.66 nm, whereas the Debye length of the SE at the same interface is 0.63 nm. At the SE-PE interface, the Debye lengths of the electrolyte side and PE side are 0.71 nm and 0.49 nm respectively [72]. Different Debye lengths indicate different electric potential gradients at each side of the same interface. For instance, at the NE-SE interface, the maximum electric potential gradient is  $5.68 \times 10^5 \text{ V m}^{-1}$  in the NE side and  $3.42 \times 10^7 \,\mathrm{V m^{-1}}$  in the SE side [72]. The thickness of the Debye length does not only depend on the relative permittivity of the materials (see Section 2.1) [70], but also on the surface concentration and the potential difference of the electrode and the electrolyte during operation [71]. Fig. 14c1) and 14(c2) illustrate the electric potentials across the cell for the electroneutral model and the non-electroneutral model. In the electroneutral model, an instantaneous change of the concentration and electric potential are assumed at the interfaces, whereas the electric potential is continuous in the non-electroneutral model following Maxwell's first law [72]. The space-charge layers act as a shock absorber, which allows the electric potential to change gradually at the interfaces [239].

One should note that the formation of a space-charge layer is different from the formation of the passivating layers, though both mechanisms occur at the interface [71,72]. A passivating layer is formed as a result of the decomposition reactions whereas a space-charge layer is formed due to the non-homogeneous charge distribution at the interfaces [59,71,72]. Most solid-state relevant space-charge models proposed in the literature do not



A comparison in the distribution of the Li concentration across the bulk SE and at the electrode–electrolyte interfaces. The absence of concentration gradients across (a) LiPON, (b) LLZO and (c) Li $_3$ PS $_4$  SE implies a near-unity transference number in the bulk SE. However, the variation of Li concentrations at the interface indicates that the local space-charge layers are non-electroneutral. Reprinted with permission from Ref. [12], Copyright (2019), Nature Energy.

account for the effects of interfacial decomposition reactions [24,70–72,236,240]. The charge-transfer at both interfaces (NE-SE and SE-PE) can be represented by the Kröger-Vink notation as [72]

$$Li(NE) + V'_{Li}(SE) \rightleftharpoons Li^{X}_{Li}(SE) + e^{-}(NE),$$
 (9)

$$\operatorname{Li}_{i}^{X}(SE) + e^{-}(PE) \rightleftharpoons \operatorname{Li}_{i}^{X}(PE) + V'_{i}(SE), \tag{10}$$

where SE, PE and NE denote the solid electrolyte, positive electrode and negative electrode, respectively.

In general, the charge distributions at the interfaces can be described with the Helmholtz model, Gouy-Chapman's model or the Stern's model [241–245]. Different variations of these models have been proposed to account for the surface concentrations and potential drops at the interfaces [246]. Depending on the electrical forces between the electrodes and the charged species, specific adsorption of the charged species can also happen

[237,247]. In the context of solid-state batteries, the BV kinetic relation has been used to model the charge-transfer at the interfaces [44,58,248]:

$$i = i_{0,\text{neg}} \left[ \exp \left( \frac{\alpha_{\text{ox}} F \eta_{\text{neg}}^{\text{ct}}}{R_{\text{gas}} T} \right) - \exp \left( \frac{-\alpha_{\text{red}} F \eta_{\text{neg}}^{\text{ct}}}{R_{\text{gas}} T} \right) \right], \tag{11}$$

$$i = i_{0,pos} \left[ \exp \left( \frac{\alpha_{ox} F \eta_{pos}^{ct}}{R_{gas} T} \right) - \exp \left( \frac{-\alpha_{red} F \eta_{pos}^{ct}}{R_{gas} T} \right) \right].$$
 (12)

The BV model assumes a single-step reaction across the interfaces between the bulk electrode and the bulk SE without accounting for the space-charge effects. As a result, this kinetic model cannot reproduce the high-frequency semi-circles as observed by the impedance measurement. Only the low-frequency impedance model governed by the diffusion mechanisms can be described by the standard BV model [237,238].

To account for the effects of double-layers, the exponential term in the Butler-Volmer's kinetic model can be corrected to describe the potential difference across a Stern layer between the electrode and the electrolyte. This kinetic relation is known as the Frumkin-Butler-Volmer (FBV) model and was implemented by Landstorfer et al. and Rossi et al. to model an electrolyte membrane comprised of fixed anions and mobile cations [236,238,240]. The FBV model at the NE and electrolyte interface can be represented by [236]

$$j = k_{\rm ox} \exp\left(\frac{\alpha_{\rm ox} Fn}{R_{\rm eas} T} \Delta \phi_{\rm NE-SE}\right) - k_{\rm red} \frac{c_+}{c_{+,0}} \exp\left(\frac{-\alpha_{\rm red} Fn}{R_{\rm eas} T} \Delta \phi_{\rm NE-SE}\right), \quad (13)$$

whereas the FBV at the electrolyte and PE interface is given by [236]

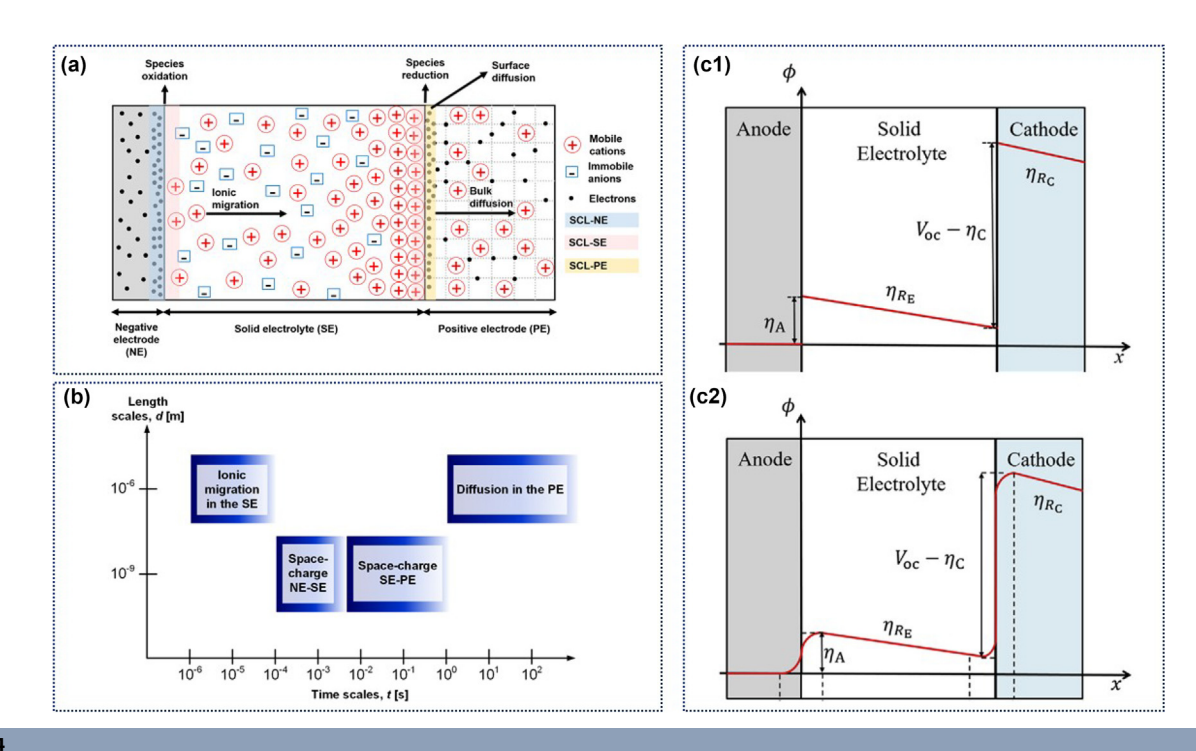
$$j = k_{\rm ox} \exp \left( \frac{\alpha_{\rm ox} F n}{R_{\rm gas} T} \Delta \phi_{\rm SE-PE} \right) - k_{\rm red} \frac{c_+}{c_{+,0}} \exp \left( \frac{-\alpha_{\rm red} F n}{R_{\rm gas} T} \Delta \phi_{\rm SE-PE} \right). \tag{14}$$

 $\Delta\phi_{\text{NE-SE}}$  and  $\Delta\phi_{\text{SE-PE}}$  are the correction terms that describe the linear potential drop between the electrodes and the reaction planes at each interface. The reaction plane was defined as the intersection between the Stern layer and the diffusive layer, where the Faradaic charge-transfers occur [236].

The capacitive contribution to the electrode reactions can also be modelled by modifying the interfacial current to include the faradaic current due to charge-transfers at the interfaces ( $i_{\rm ct}$ ) as well as the non-faradaic current due to charge/discharge of the double layers ( $i_{\rm DL}$ ) [24,239]. Therefore, the sum of interfacial current,  $i_{\rm int}$  becomes [24,238,239]

$$i_{\text{int}} = i_{\text{ct}} + \underbrace{C_{\text{int}} \frac{\partial (\phi_{\text{s}} - \phi_{\text{e}})}{\partial t}}.$$
 (15)

The academic discussions on the effects of the space-charge layers have been debatable. Klerk et al. [71] calculated the space-charge capacitance and resistance for the LLZO and the Li<sub>1.2</sub>Al<sub>0.2</sub>Ti<sub>1.8</sub>(PO<sub>4</sub>)<sub>3</sub> (LATP) SEs at both interfaces. The space-charge resistance and capacitance were shown to depend on the applied voltage. By accounting for the Coulomb interactions between charged defects, they concluded that the space-charge effects are negligible at the device level due to the small space-charge resistance and capacitance [71]. On the other hand, Wan and Ciucci [72] suggested that the accumulation or depletion of the charged species at the interface limits the charge-transfer reaction, which reduces the exchange current densities and increases the charge-transfer resistance. Although the maximum electric potential gradients at both interfaces reach a magnitude between  $10^5-10^{10}~{\rm V~m^{-1}}$ , the charge-transfer overpotential calculated from the non-electroneutral model is negligible at the NE-SE interface



(a) An illustration of different possible mechanisms occurring during discharge in the domains of space-charge layers, bulk SE and across the PE. (b) A mapping of the mechanisms in an ideal thin-film solid-state cell according to the time and length scales. The time scales were estimated from the EIS measurement [24,47,58], whereas the length scales of the space-charge layers were taken from the non-electroneutral model computed by Wan and Ciucci [72]. The length scales of the bulk electrolyte and the non-porous PE were given by their thickness [48]. The electric potential variation across the cell represented by the electroneutral model (c1) and the non-electroneutral model (c2). Reprinted with permission from Ref. [72], Copyright (2020), Elsevier.

and varies between  $\approx 0.02-0.12~V$  at the SE-PE interface [72]. However, these electric potential gradients can induce Maxwell stresses at the interfaces [72,249].

By comparing the electroneutral and non-electroneutral model, Wan and Ciucci showed that the space-charge layers affect the exchange current density term of the kinetic model [72]. The exchange current density can be defined as the current density at equilibrium, where both the forward and reverse reactions have the same rate [69]. It is also a model parameter that can be estimated from the EIS measurement, in which the space-charge effects are considered in the model implicitly [44]. Nevertheless, the EIS measurement of the exchange current density has one limitation due to the assumption of the linear current-voltage relationship. For a small perturbation amplitude (≤ 20mV), the current response to an applied potential can be approximated as linear [250]. As shown by the CV measurement of thin-film solid-state cells, the relationship between the current and voltage is highly non-linear [251]. This non-linearity can be attributed to interfacial reactions, current-strength dependent solid-state diffusion losses and strong concentration gradients in the electrode under load [47]. For an operating condition near equilibrium, the kinetic parameters estimated from the linear EIS is sufficient to describe the cell behaviour. If the operating conditions deviate significantly from the equilibrium such as under high current densities (≥ 7C), the assumption of a linear current-voltage relationship is no longer valid, and the non-linear losses must be taken into account [47]. In contrast to the linear EIS, the report of using the Non-Linear Electrochemical Impedance Spectroscopy (NLEIS) method is scarce due to the requirement of multiple instruments such as function generator and high-speed digitisers in addition to the different control, data acquisition and signal processing programs [250,252]. However, kinetic parameters estimated from the NLEIS measurements could provide valuable insights in choosing the most appropriate electrochemical kinetic model. The response at fundamental frequencies to large amplitude excitations can reveal additional mechanisms indistinguishable with the use of linear EIS [250,253].

In reality, the effects of space-charge at the interfaces are coupled with the charge-transfer and the surface diffusion [24,237,239]. The underlying physics governing the spacecharge behaviour is the time scales, during which the spacecharge effects are most dominant [24,47,58,239]. However, the time scales due to space-charge effects obtained by EIS frequency measurements are different from the time evolution in NDP measurements. While space-charge effects are usually shown to occur in short time scales corresponding to high-frequency and midfrequency regions (1 MHz - 1 Hz) from EIS measurements [24,47,58], Han et al. [12] demonstrated that the surface concentration continues to change above thousands of seconds in NDP measurements. Further works are required to study these differences in the future. Fig. 14(b) illustrates the mapping of the space-charge effects, the ionic conduction in the bulk SE and the Li diffusion in the PE according to their time and length scales. For an ideal solid-state cell without considering the interfacial decomposition reactions or the nucleation of Li filaments, the space-charge effects are most visible within the time scales between µs and ms, and the length scales are on the orders of

10 nm [58,72]. The ionic conduction in the bulk SE occurs on a short time scale (µs) but over a longer length scale (µm). On the other hand, the mass transport in the non-porous PE happens in a longer time scale ( $\geq 1$  s) and also a more extended length scale (µm) [48,58]. Comparing the length and time scales of the space-charge effects to the bulk ionic conduction or diffusion in the electrode does not imply the insignificance of the space-charge models. In contrast, the space-charge models are especially relevant when analysing the impacts of doping on the interfacial properties or the effects of charge accumulation/ depletion on the degradation behaviour [72,238]. Compared to a thin-film cell configuration, which only has one interface between the SE and the electrodes, a composite solid-state cell Li cell has multiple interfaces. Therefore, the effects of spacecharge may be more dominant in such cell architecture. Further studies are required to evaluate the impacts of space-charge and its interplay with surface diffusion on cell performance under different operating conditions.

### 4.1.4. Diffusion limitations in non-porous positive electrodes

One major feature differentiating the thin-film and the composite solid-state cell configuration is the PE. The PE in the thin-film configuration is non-porous. Therefore, the electrochemical oxidation and reduction occur only at the external surface between the bulk SE and the PE [44,58]. The crystalline LCO and nanocrystalline LiMn<sub>2</sub>O<sub>4</sub> (LMO) are the commonly studied PEs for the thin-film cell configuration [226]. Due to more phases and wider stoichiometry in the LMO PE, the hysteresis observed in the LMO film is more significant compared to that in the LCO films [226].

Bates and co-workers [254] measured the principal diffraction lines of LCO-films and found that the grain orientations are strongly dependent on the film thickness. Three types of grain orientations can be observed from the XRD analysis in the LCO films: (003)-oriented grains, (101)-oriented grains and (104)-oriented grains. The film with more percentages of (101) and (104)-orientations are more favourable to the Li diffusion compared to the (003)-grains due to the in-plane diffusion. For a film with (003)-orientation, Li must diffuse in the perpendicular direction through the close-packed oxygen layers. It should also be noted that the deposition temperature also affects the grain distribution significantly. The film deposition at higher temperatures causes the formation of larger grains and more void fraction, which subsequently increases the film resistance [254].

Other than the grain orientations, the phase transformation in the LCO film is another critical variable affecting the diffusion coefficient of Li<sup>+</sup>. The diffusion coefficient in the LCO film is not constant as commonly assumed but varies with the Li concentration upon lithiation and delithiation [44,58]. The diffusion coefficient can be measured with either the Galvanostatic Intermittent Titration Technique (GITT) or the PEIS method [44,58,255]. Matsuda et al. [200] measured the structural change of the LCO electrode with the *in-situ* Raman spectra and observed the formation of five phases in the film. Phase changes have two significant implications. Firstly, a thicker bulk PE was shown to demonstrate a higher percentage of capacity drop compared to a thinner PE at high current densities [256]. Secondly, the phase transformation in the PE causes large voltage change and con-

tributes to the reversible heat generation. For a cell with the LCO electrode, the rate of reversible heat generation due to the structural change can be as large as 700% of the irreversible heat generation in the operating regime of C/8 and 5-40% SOC [251].

#### 4.1.5. Overpotential analysis

In the absence of current flow, the cell potential is known as the equilibrium or Open-Circuit Potential (OCP), which denotes the maximum work achievable in batteries. During discharge, the current enters through the negative current collector and travels through the solid NE to the NE-SE interface, where oxidation occurs. Then, the current travels through the SE to the SE-PE interface, where the reduction occurs, and the current is transferred into the non-porous PE. Finally, the current travels through the PE until it reaches the positive current collector [257]. The passage of current through the cell causes different resistance and voltage losses. Therefore, the cell voltage, V, can be expressed by [24]

$$V = U_{PE}(c_s) + \eta_{PE}^{diff} + \eta_{PE}^{mt} + \eta_{PE-SE}^{ct} - \eta_{SE}^{mt} - \eta_{SE-NE}^{ct} - U_{NE},$$
 (16)

where  $\eta_{\rm PE}^{\rm diff}$  is the diffusion overpotential in the PE;  $\eta_{\rm PE}^{\rm mt}$  is the mass-transfer overpotential due to the electronic transport in the PE;  $\eta^{\rm ct}$  is the charge-transfer overpotential at the respective interface;  $\eta_{\rm SE}^{\rm mt}$  denote the ohmic losses in the SE and  $U_{\rm NE}$  is the OCP of the NE. In a solid-state cell, in which a metallic Li is used as the NE, the term  $U_{\rm NE}$  is zero.

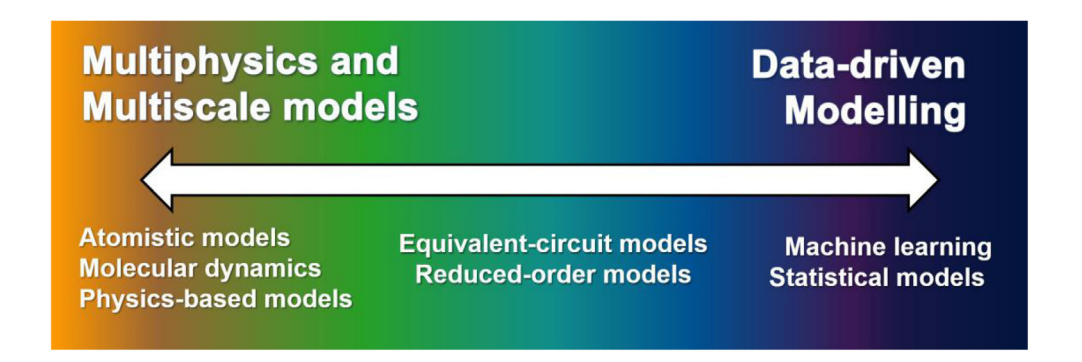
The analysis of overpotentials is often used in physics-based models to estimate the performance of solid-state batteries. For instance, Raijmakers et al. [24] and Wan and Ciucci [72] showed that the ohmic loss in the SE is the dominant overpotential during the low and high C-rate of constant-current discharge. Under pulse operating conditions, the diffusion overpotential in the PE was found to be dominant for long and short pulse durations [24,58]. During the interruption of external currents, the development of the local concentration gradients in the solid electrode causes the redistribution of material and the diffusion overpotential [258]. The voltage losses can be reduced by improving the ionic conductivity of the SE, reducing the thickness of the SE, decreasing the thickness of the PE or modifying the cell architecture altogether from a thin-film configuration to a three-dimensional composite configuration [47,58,225,259,260].

While physics-based models are useful in understanding the internal dynamics of a battery, this modelling approach requires the estimation of many parameters. The measurement of realworld parameters in battery research is challenging due to manufacturing defects, cell-to-cell variability, measurement uncertainties as well as the evolution of grain boundaries and interfaces over time (see Table 4) [261-264]. Recently, Wu et al. [265] proposed the fusion of multiphysical and multiscale modelling approaches with machine-learning methods as a possible solution to address the problems of inherent cell-to-cell variability. Fig. 15 shows a spectrum of battery modelling approaches, which consists of multiscale and multiphysics models on the left end and data-driven models such as machine learning models on the right end. Due to the extensive and even destructive characterisation experiments required for physics-based model parametrisation, it becomes impractical to measure all the parameters for every single cell [265]. By learning the battery

TABLE 4

A summary of modelling techniques with their applications and limitations in solid-state battery research.

| Modelling avenues             | Applications/Advantages  | Challenges and limitations  | Ref.                                 |
|-------------------------------|--|---|--------------------------------------|
| DFT models                    | <ul> <li>Investigate atomistic structure, interfacial stability, synthesisability and conductivity of SEs;</li> <li>Databases of DFT calculated energies of bulk structures, such as the Materials Project and the Open Quantum Materials Database, allow for the rapid calculation of grand potential phase diagrams and the assessment of interfacial stability of SE materials against both the NE and PE.</li> </ul> | <ul> <li>Expensive so only small systems can be used (&lt; 1000 atoms);</li> <li>Enumerating all possible interface orientations between two materials is computationally challenging. Many studies thus use a limited number of interfaces, chosen based on experimentally observed orientations of the materials or by joining two low energy surfaces of the two materials.</li> </ul> | [59–61]<br>[38,279,280]<br>[281–283] |
| Analytical<br>models          | <ul> <li>Low computational costs in modelling specific<br/>mechanisms;</li> </ul>  | <ul> <li>Interdependence and full coupling between solid-<br/>state electrochemistry and other mechanisms are<br/>often not represented by analytical models;</li> </ul>  | [22,85,104,126]                      |
| Physics-based<br>models       | <ul> <li>Analyse the internal dynamics of a cell (e.g. overpotentials and concentration gradients);</li> <li>Predict the battery behaviour under different operating conditions;</li> <li>Design prototype for next-generation solid-state batteries.</li> </ul>   | <ul> <li>Requires extensive and even destructive experiments to estimate the model parameters;</li> <li>Uncertainty and sensitivity of the parameters could affect the model predictions;</li> <li>High computational costs in solving coupled physics-based models.</li> </ul>   | [24,44,248]<br>[18,72]               |
| Microstructural<br>models     | <ul> <li>Models the effects due to particle sizes, composite electrode distributions, volume fractions and voids on the cell performance;</li> <li>Reconstructed microstructures using tomography resembles realistic electrode/SE compositions;</li> <li>Random packing of spherical particles in synthetic microstructural models;</li> </ul>  | <ul> <li>The choice of representative reconstructured microstructures could affect the model predictions;</li> <li>High computational costs to resolve the mesh and to solve coupled mechanisms;</li> <li>High computational costs to account for the effects of carbon additives.</li> </ul>   | [25,260,271]<br>[62,273]             |
| Transmission<br>line models   | <ul> <li>Estimate the internal resistance due to different<br/>components in a composite cell.</li> <li>Predict the cell discharge behaviour under different<br/>operating conditions.</li> </ul>  | <ul> <li>The model assumes an ideal RC impedance behaviour.</li> <li>The cell impedance must be converted into a time-dependent overpotential using a series of RC circuits.</li> </ul>   | [47]                                 |
| Machine<br>learning<br>models | <ul> <li>High throughput discovery and screening of potential materials for solid-state batteries;</li> <li>Can be combined with DFT models to predict structure–property relationships.</li> <li>Deep convolution neural network can be used to track pores formation at the Li—SE interface.</li> </ul>  | <ul> <li>Requires a large amount of training and test datasets<br/>to achieve a high confidence in model predictions.</li> </ul>  | [39,49,180]<br>[284,285]             |



An illustration of battery modelling spectrum: On the left end, multiscale and multiphysics models are typically constructed based on first-principles and fundamental physics of a battery. On the right end of the spectrum, data-driven models such as statistical and machine learning approaches are mechanisms-agnostic models that do not require prior knowledge of the battery chemistries. In the middle of the spectrum, equivalent-circuit models and reduced-order models are semi-empirical models developed based on experimental data.

behaviour and improving the performance from training data, machine learning approaches such as artificial neural networks and Gaussian/Bayesian regression have shown promise to adapt to the inherent variability in batteries [265]. However, this method requires a large amount of training data to produce an

accurate predictive model (Table 4). Therefore, high-fidelity multiphysical and multiscale models could be used to train machine-learning models, creating new opportunities for fusing the advantages of both modelling approaches [265]. By using these hybrid models to estimate the state-of-charge, state-of-

available-power and state-of-health, dynamic limits that account for real-world operating conditions can be used as a basis for intelligent solid-state battery management and diagnostics [265].

#### 4.2. Three-dimensional solid-state cells

For a thin-film cell configuration, increasing the electrode thickness is not proportional to the improvement in the cell's rate capability due to a longer diffusion distance of Li-ions into the PE [44,58,267]. One alternative to improving the energy and power density is the fabrication of a fully conformal three-

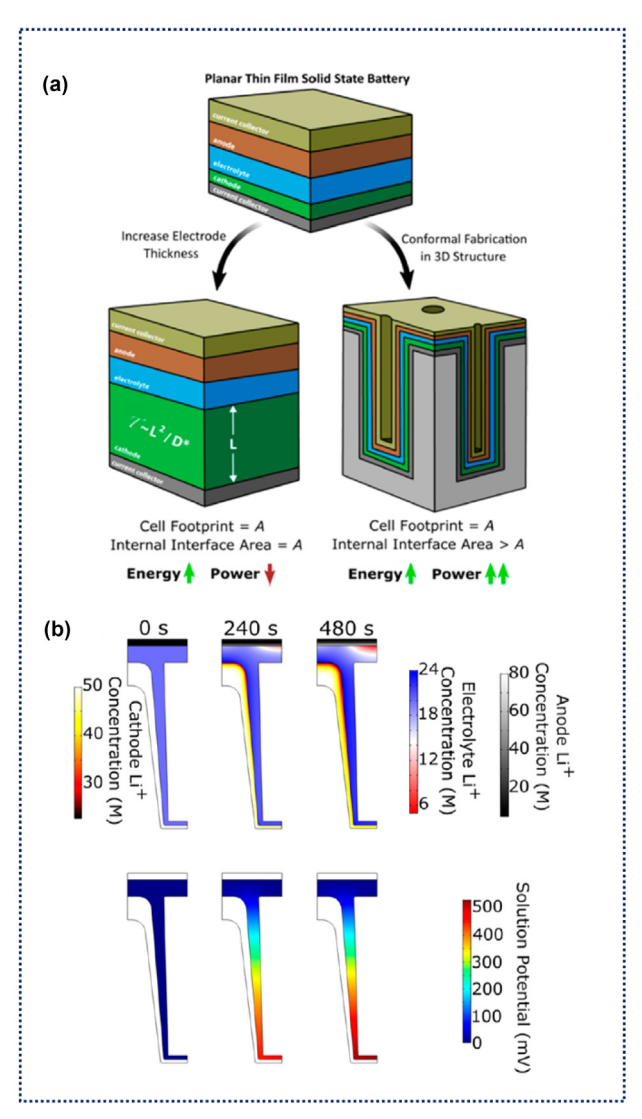


#### FIGURE 16

(a) A comparison of a thick planar thin-film cell with the 3D conformal solid-state cell. For the planar thin-film cell, an increase in the electrode thickness causes the drop in the power density due to the diffusion limitation across a thick electrode. By enlarging the internal surface area, a 3D structure improves the energy density without sacrificing the power density. Reprinted with permission from Ref. [225], Copyright (2018), American Chemical Society. (b) Physics-based model of a 3D solid-state cell: the inner column represents the concentration distribution of  ${\rm Li^+}$  in the PE, whereas the outer column depicts the concentration of  ${\rm Li^+}$  and potential gradients in the SE. The significant potential gradient towards the bottom of the microcolumns was attributed to the non-uniform electrode and electrolyte structures. Reprinted with permission from Ref. [223], Copyright (2016), American Chemical Society.

dimensional solid-state cell [223,225,268,269]. Fig. 16a shows the schematic of a planar thin-film cell and a three-dimensional solid-state cell. (See Fig. 17).

Talin et al. [223] fabricated a 3D solid-state cell (Si-LiPON-LCO) by using the Physical Vapour Deposition (PVD) and compared the performance of the 3D cells to planar thin-film cells. While the planar thin-film cells could deliver a specific capacity of approximately 20 μAh cm<sup>-2</sup> up to 3.3 C, the specific capacity achieved with the 3D solid-state cells was less than  $5\,\mu\text{Ah}\,\text{cm}^{-2}$ at 1.2 C. The lower specific capacity of the 3D solid-state cells was attributed to the non-uniform electrolyte thickness. As a result, the 3D solid-state cell had an inhomogeneous internal current distribution and a significant potential drop towards the bottom of the microcolumns. Pearse et al. [225] showed that the problem of non-uniform electrolyte thickness could be overcome by fabricating a fully conformal 3D solid-state cell using the Atomic Layer Deposition (ALD). They introduced a metric known as the Area Enhancement Factor (AEF) to quantify the performance of the 3D cell:

$$AEF = \frac{A_{\text{int}}}{A_{\text{f}}},\tag{17}$$

where  $A_{\rm int}$  is the true internal surface area and  $A_{\rm f}$  is the footprint area of the cell on the substrate. The AEF can be enlarged by increasing the depth of microcolumns. They demonstrated that the 3D conformal cell with AEF10 has a higher discharge capacity compared to AEF4 and AEF1 (planar cell) for all current densities ( $\leq 10000~\mu A~cm^{-2}$ ) up to 100 cycles [225]. This performance improvement was attributed to a shorter diffusion distance in the non-porous PE and a larger uniform interfacial area, which result in lower overpotentials [225].

#### 4.3. Composite solid-state cells

Unlike the thin-film cell architecture, the electrochemical oxidations and reductions occur at the various interfaces between the SE and AMs in a porous composite electrode [47]. Randomised orientations will also occur between crystal particles in the SE and electrode, which may have a mixture of 2-dimensional and 3-dimensional Li<sup>+</sup> diffusion pathways, leading to a mixture of favourable and unfavourable interfaces between the particles for fast Li<sup>+</sup> transport across all possible combinations of particle surface orientations. Therefore, an in-depth understanding of the microstructural morphology such as particle sizes, size distribution, porosity and tortuosity are essential in optimising the electrode composite design [25,62,270–272]. In general, there are three different approaches to study the microstructures of a composite electrode. The first approach involves the reconstruction of the microstructures from real electrodes and measurement of the microstructural parameters using SEM [112,270,272,273], Focussed- Ion-Beam Scanning Electron Microscopy (FIB-SEM) [260,271] or XCT [266,272]. The second approach is the numerical generation of synthetic electrode microstructures by ordered or disordered packing of spherical particles in a threedimensional simulation box [25,62]. In the third approach, the microstructural behaviour can be described based on an assumed average particle coordination number and the percolation theory [266,274].

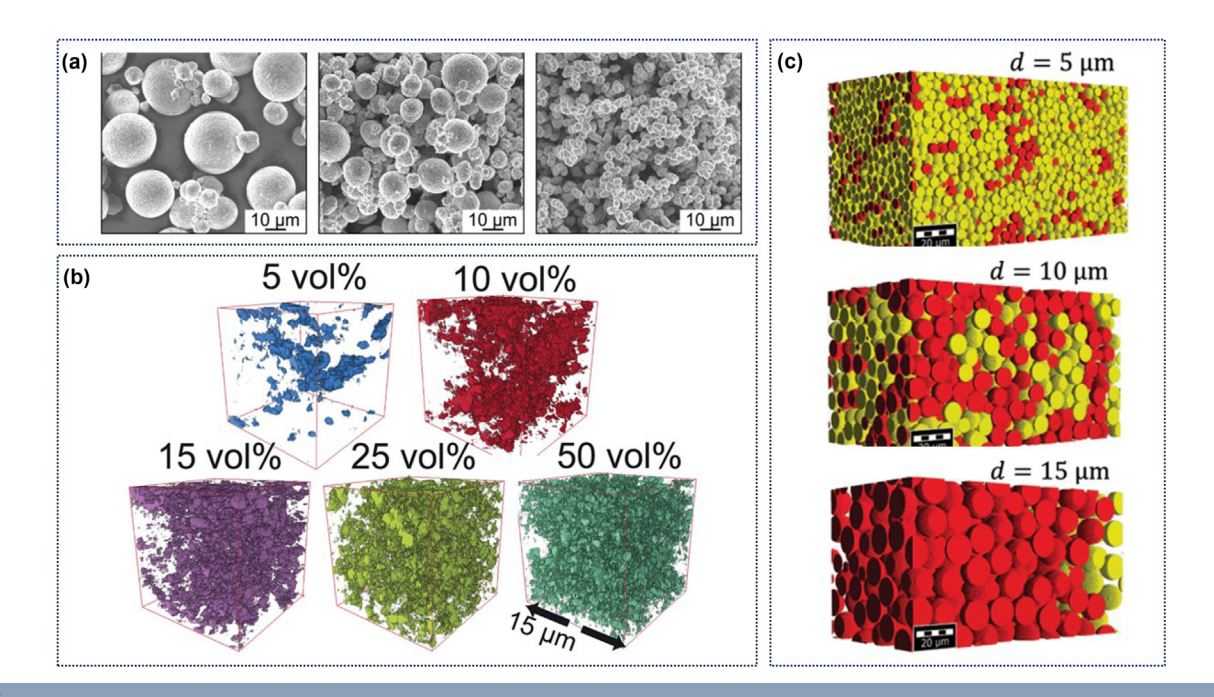


FIGURE 17

(a) Scanning Electron Microscopy (SEM) visualisation of the non-coated  $LiNi_{1-x-y}Mn_xCo_yO_2(NMC)$ -622 composite PE: NMC-Large, NMC-Medium and NMC-Small. Reprinted with permission from Ref. [112], Copyright (2018), American Chemical Society. (b) 3D reconstructed hybrid SE with different volume fraction of Al-LLZO (5-vol%, 10-vol%, 15-vol%, 25-vol%, 50-vol%) using the synchrotron nano-tomography. Reprinted with permission from Ref. [266], Copyright (2019), Royal Society of Chemistry. (c) Numerical generation of synthetic composite electrodes with different particle sizes  $(5\mu m, 10\mu m, 15\mu m)$ : the yellow particles denote percolated particles in the electronic conduction clusters whereas the red particles represent unconnected particles. Reprinted with permission from Ref. [25], Copyright (2019), American Chemical Society.

#### 4.3.1. Performance limiting mechanisms

Particle sizes of the composite electrode. The effects of the NMC particle sizes and LPS SE on the electrode performance were first investigated by Sakuda et al. [270]. The NMC particles had an average size of 9µm and 5µm, whereas the SE has an average size of 4µm and 16µm respectively. They showed that the reversible capacity obtained with the SE-4µm and NMC-5µm is larger than those using SE-16µm and NMC-9µm. Based on the complementary SEM results, the higher reversible capacity achieved with the smaller particles was attributed to the homogeneous distribution of SE particles and smaller void volume in the composite electrode [270]. This conclusion can be corroborated with the results obtained by Ito and co-workers [273], who fabricated all-solid-state composite cells (In-LPS-LCO) by coldpressing LPS coated LCO particles without the sintering process. Smaller particle sizes and narrower size distribution are often correlated to better rate performance due to shorter diffusion pathways of Li<sup>+</sup> and larger surface-to-volume ratio to enhance the interfacial kinetics [275–278].

**Effects of electronic conductivity.** Strauss et al. [112] further studied the effects of non-coated NMC particles sizes on the capacity of the cells and categorised the particle sizes into three groups: NMC-Large ( $d_{50}=15.6 \mu m, d_{90}=26.1 \mu m$ ), NMC-Medium ( $d_{50}=8.3 \mu m, d_{90}=13.0 \mu m$ ) and NMC-Small ( $d_{50}=4.0 \mu m, d_{90}=4.8 \mu m$ ). The loss in the specific capacities for NMC-M and NMC-L was correlated to the fraction of inactive materials. Based on the results obtained from the *ex-situ* XRD analysis, they showed that the fraction of inactive material increases from 2% for NMC-S to 27% for NMC-M and 31% for NMC-L. By measuring the mean

ionic and electronic partial conductivity using ion or electron-blocking electrodes, the loss of inactive NMC is shown to be dominated by the electronic conductivity of NMC particles. The electronic conductivity of NMC particles decreases from  $10^{-3}$  S cm<sup>-1</sup> for NMC-S to  $10^{-6}$  S cm<sup>-1</sup> for NMC-L [112].

The conclusions obtained by Ref. [112] are different from the experimental results shown in Ref. [62]. Shi et al. [62] studied the effects of particle size on the specific capacity of the all-solid-state cell using NMC ( $d_s = 5\mu m, d_L = 12\mu m$ ) as the AMs and LPS (1.5μm - 8μm) as the SE. They showed that the cell with larger NMC particle size has a higher specific capacity than the cell with smaller particle size. It should be noted that the NMC particles were coated with Li<sub>2</sub>O-ZrO<sub>2</sub> in Ref. [62] but no coating was applied to the AMs in Ref. [112]. The contradiction was attributed to the carbon additives in the composite material [62]. While carbon nanofibers were included in the composite PE in Ref. [62], no carbon additives were used in the experimental cells of Ref. [112] due to the severe degradation effects of the additives [111]. The use of carbon additives mitigates the electronic percolation limitation in the composite PE and therefore larger NMC particles were shown to deliver higher capacity compared to smaller NMC particles.

**Effects of composite electrode composition.** Wenbo et al. [272] showed that a composite electrode composition can affect the electrode utilisation as either a high-energy or a high-power cell. The composite PE comprised of  $LiNb_{0.5}Ta_{0.5}O_{3}$ -coated LCO mixed with  $Li_{10}GeP_{2}S_{12}$  and were made in different mass ratios (LCO:LGPS in 40:60, 50:50, 60:40, 70:30 and 80:20). The accessible capacities of the composite cell increase with a

higher mass ratio of LCO for low operating current densities (< 2C). For a high discharge C-rate (10C), they showed that the composite cell with 70% and 80% of LCO has no specific capacity compared to the composite cell with 50% and 60% of LCO loading. This result implies that a sufficient electrolyte fraction in the composite cell is necessary to facilitate fast transport of Li<sup>+</sup>. The capacity retention of the composite cells was also analysed after 100 cycles. The cell with 70% of LCO was shown to retain 80% of the initial capacity [272]. This conclusion agrees very well with the experimental and modelling analysis by Shi and co-workers [62], where they showed that an optimum electrode utilisation and high specific capacities could be achieved with 60-70 wt.% of NMC particles. The performance of a solidstate composite cell depends on optimising the electronic and ionic paths within the composite electrode: Too much of SE fractions prevent sufficient electronic pathways in the AMs, whereas too high of AM mass ratios limit the ionic transport within the network of electrode particles [272].

#### 4.3.2. Microstructural modelling of the composite electrode.

Reconstruction of the microstructural electrodes. From the reconstructed composite electrode based on FIB-SEM, Hlushkou et al. [271] proposed in their studies that the void phase could occupy up to 13.2% in the composite PE. Due to the void phase, the ionic transport in a composite electrode is reduced compared to that in an ideal composite electrode, where the ions migrate along the straight and uniform pathway. The reduction in ionic transport can be described with the parameter known as tortuosity. The simulated tortuosity in the reconstructed composite electrode is 1.74, which is close to the tortuosity estimated from the EIS measurement (1.6  $\pm$  0.1). By replacing the void space with the SE in the model, they showed that the SE volume fraction could increase from 53.7% to 66.9%, and the tortuosity of the SE phase could be reduced from 1.74 to 1.27 [271]. Finsterbusch et al. [260] have also fabricated a fully inorganic, garnet-based all-solid-state cell and performed a 3D microstructure resolved continuum simulations of the composite cell (Li-LLZ:Ta-LLZ:Ta-LCO). The model predictions show a reasonable agreement with the experimental measurement at 100°C but a significant deviation of 98% can be observed at room temperature [260]. While the choice of the representative reconstructed microstructures could be one possible reason causing this deviation (Table 4), further works are necessary to identify whether the significant deviation is caused by physical phenomena not captured in the model or estimation of the model parameters at the room temperature.

Numerical generation of synthetic microstructure. Ito et al. [273] modelled the microstructural behaviour by placing the spherical particles randomly in a simulation box. The phase-field method was further used to obtain a smooth interface and to construct the 3D electrode microstructure. Bielefeld et al. [25] generated synthetic 3D microstructures with particle sizes ranging from  $3\mu m$  to  $15\mu m$  to study the effects of particle size, volume fractions of AMs, composition, porosity and electrode thickness on the utilisation level and specific surface area of the composite electrode. The model accounts for the ionic conducting phase due to the SE and the electronic conducting phase due to the AMs. Smaller particles were shown to

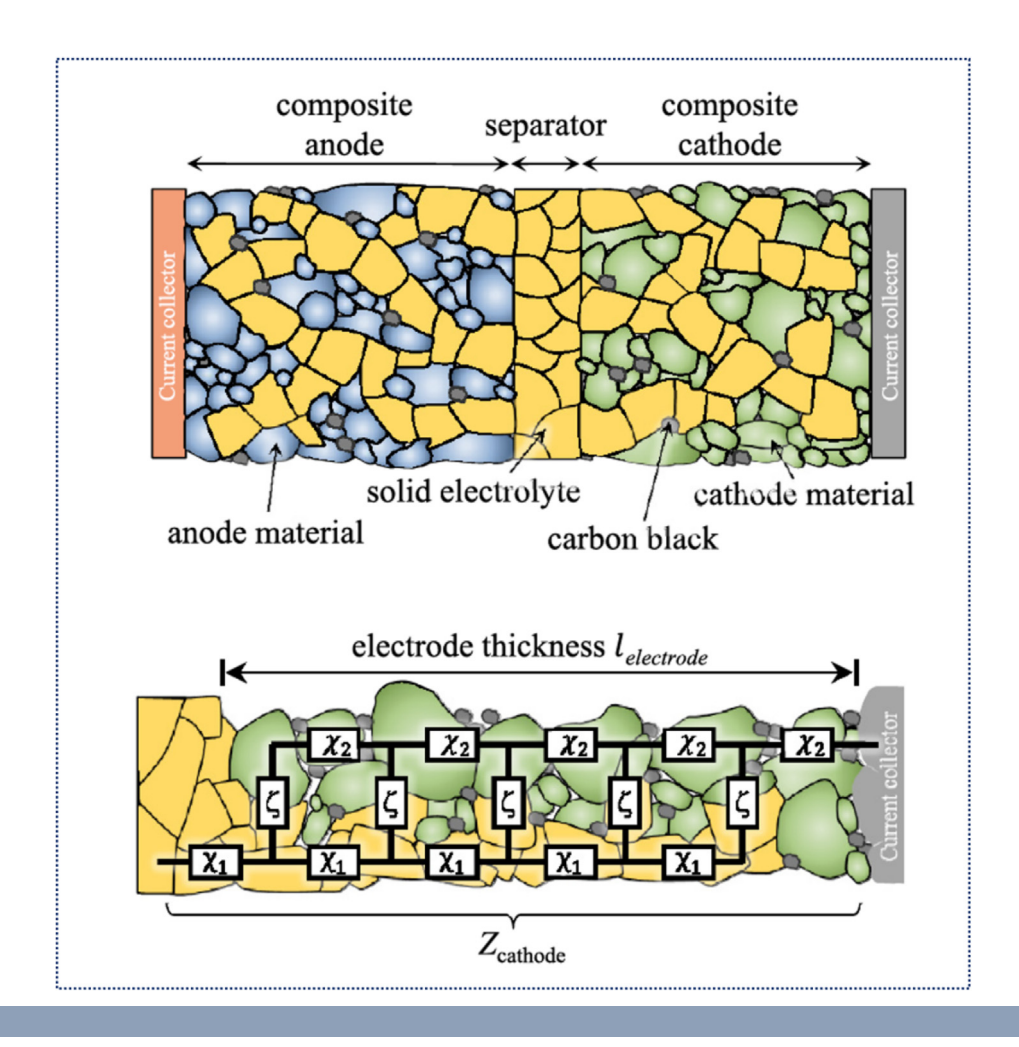
have higher electronic percolation and lower percolation threshold. The model prediction also demonstrated that the specific active interfacial area increases with smaller porosities, indicating that a denser composite electrode could form better conduction clusters. However, the conclusions shown in Ref. [25] differ from the recent modelling works reported in Ref. [62]. In Ref. [62], it was shown that a large ratio of  $d_{\rm AM}/d_{\rm SEdAM}/d_{\rm SE}$  yields a high utilisation of the composite PE, whereas Ref. [25] showed that the electronic percolation decreases for larger electrode particles. Due to the computational limitation ( $10^{10}$  number of particles) [62], both models did not account for the carbon additives explicitly. Therefore, more modelling works that include carbon additives are required in the future to examine the overall effects of particle sizes and electronic conductivity on the performance of composite PE.

Transmission line model. Braun et al. [47] developed a one-dimensional homogenised transmission line model to estimate the internal resistance due to the ionic conducting phase of the SE and the electronic conducting phase of the AMs in the composite cell (Fig. 18). While the model predicts the cell discharge behaviour of LCO-Li $_{10}$ GeP $_2$ S $_{12}$ —Li $_{10}$ GeP $_2$ S $_{12}$ —Li $_4$ Ti $_5$ O $_{12}$ - $Li_{10}GeP_2S_{12}$  at near equilibrium and for low C-rate (< 7C) relatively well (with a maximum deviation of 13%), the model prediction deviates from the experimental measurement by 150% for high C-rates (> 45C) [47]. The difference between experimental measurements and model predictions can be attributed to two possible reasons. Firstly, the 1D transmission line model assumes an ideal RC behaviour, whereas the experimental impedance measurements often exhibit a non-ideal RQ behaviour [32,45,24]. Secondly, the large deviation under high-current load could be caused by non-linear losses (see the description of NLEIS in Section 4.1.3) [47]. It is also worth noting that the cell impedance estimated from the transmission line model must be first converted into a time-dependent overpotential using a series of RC circuits. Therefore, transient cell behaviours cannot be predicted directly with the proposed model (see Table 4) [47].

#### 5. Conclusions and perspectives

5.1. Review conclusions

Multiphysical properties of solid-state batteries. We have taken a holistic approach to describing the multiphysical behaviour of solid-state cells, including their electrochemical, chemical, thermal and mechanical properties. Although sulfidebased SEs have better electrochemical properties (e.g. ionic conductivities and critical current densities) than oxide-based SEs, their mechanical properties such as shear modulus are much lower than that of oxide-based SEs. According to the linear elasticity analysis from Monroe and Newman [102], the mechanical strength of sulfide-based SEs is just sufficiently compliant to suppress the Li filaments propagation. Nevertheless, the compounded effects of the shear modulus and critical current densities should be a subject of further investigation to understand the susceptibility of SEs to Li filamentary nucleation and penetration. On the other hand, oxide-based SEs were predicted via first-principles modelling to generate oxygen gas at higher voltages, which could react with the Li NE to cause adverse decompositions. Most importantly, we highlight that all SEs



The 1D transmission line model represents the microstructure of a composite positive electrode ( $\text{Li}_{10}\text{GeP}_2\text{S}_{12}\text{-Li}_4\text{Ti}_5\text{O}_{12}$ ). The yellow particles depict the SE fractions and are modelled by  $\chi_1$ . The green particles denote the PE fractions and are modelled by  $\chi_2$  in the transmission line model.  $\zeta$  describes the charge transfer at the interface and the solid-state diffusion in the AM. Reprinted with permission from Ref. [47], Copyright (2018), Elsevier.

should be manufactured and assembled under an inert environment. On exposure to air, LiPON generates PH<sub>3</sub> and NH<sub>3</sub> gas, whereas Li<sub>7</sub>La<sub>3</sub>Zr<sub>2</sub>O<sub>12</sub> reacts to form LiOH and Li<sub>2</sub>CO<sub>3</sub>; Li<sub>2</sub>S-P<sub>2</sub>S<sub>5</sub> are hygroscopic and form H<sub>2</sub>S gas. Whether the release of these gases also poses a safety hazard if batteries are mechanically damaged during operation should also be established.

Multiphysical degradation mechanisms. This review also summarises the impacts of multi-physics mechanisms on various degradation modes under different operating conditions. Beside the intercalation-induced stresses and SEs cracking, other degradation mechanisms include phase change and structural disordering, temperature and pressure-dependent Li creep, electrode-electrolyte interfacial decompositions, instability of carbon additives, surface voids, interfacial delamination, Li filamentary nucleation and current collector fracture. As summarised by Table 2, different operating conditions trigger significantly different degradation mechanisms. High operating temperatures reduce the electrolyte resistance and increase the critical current densities but accelerate the interfacial decomposition and Li creep. Although operating at high current densities could achieve higher power densities, but compared to low Crates, high C-rates also cause more electrolyte and electrode particle cracking, the formation of surface voids and Li filaments.

**Solid-state physics and cell architechture engineering.** It is crucial to understand the impacts of solid-state physics such as melting points and diffusivities occurring in different cell architectures. For example, solid-state Li-metal cells fail during the solder reflow manufacturing due to the low melting temperature of Li metal. As a result, Li metal alloys and NE-free configurations have been suggested to replace the Li NE. The sluggish diffusion in the non-porous PE implies that a higher electrode utilisation and better cell performance can be achieved with a composite PE.

## 5.2. Perspectives

By reviewing the recent progress on experimental investigation and computational modelling, future pathways for investigation are summarised as follows:

**Experimental characterisation and model parametrisation.** Many pioneering experimental works have characterised the cell under ideal or near-equilibrium conditions, using the techniques summarised in Table 3. For instance, the electrochemical stability of SEs was often measured with the cyclic voltammetry technique on a blocking cell configuration, which deviates from a real cell configuration that has both electrodes and additives. Besides, many model parameters used for

continuum cell modelling were estimated from EIS measurements, thus only valid where the battery response is linear. At high current densities, non-linear losses may be significant and should, therefore, be analysed along with the non-linear EIS measurements. Due to the strong dependence of relative permittivity on temperature and frequency, future parametrisation works should assess the impacts of different operating conditions on the space-charge formation.

Direct experimental observation of buried solid/solid interfaces is challenging. Non-destructive measurement protocols such as ultrasonic scanning, thermal imaging and photoacoustic imaging methods could be employed to probe internal mechanisms of a cell without destroying its structural integrity [286,287]. The ability to combine multiple aspects of experimental characterisation of chemical, mechanical and (micro) structural information and their transformations at SE/electrode interfaces in solid-state batteries could be an important step to understand these often coupled phenomena. For example, it has been shown that Li filaments formation depends on electro-chemo-mechanical behaviours, highlighting the importance of simultaneously studying physical and chemical properties. Probing several length scales at once by employing synchrotron techniques (e.g., X-ray microscopy and XANES) and measuring cells away from equilibrium conditions (such as in-operando cell cycling) will also aid in obtaining a holistic understanding of these systems under close-to operating conditions. In addition, in-situ or in-operando techniques studying a range of length scales from cell-level (i.e., in-situ FIB or NMR-MRI) and atomistic-level (i.e. in-situ TEM) will be helpful in studying phenomena which may be difficult to see in traditional post-mortem analyses (such as buried interfaces which are airsensitive or susceptible to mechanical interference, when a cell is dismantled).

**Optimising conductive additives.** The optimisation of the composite PEs is essential, particularly through the use of conductive additives that do not react with the electrolytes and electrode to limit cycle life.

Interface engineering. Electrode/electrolyte interfacial stability is a critical factor in determining the performance of solid-state batteries. In particular, using a highly reducing Li metal NE can lead to degradation of the electrolyte and formation of secondary phases, contact loss, current hotspots and eventually Li filament formation on the application of current during operation. Computational methods have contributed to the understanding and prediction of decomposition pathways, and much work has been carried out to experimentally determine the reaction products and chemical and structural changes occurring. While cutting edge characterisation techniques continue to be developed, probing the materials chemistry of buried interfaces continues to be a significant challenge experimentally, particularly at the atomistic level. The use of coupled computational methods and experimental characterisation will aid this progress, which is necessary to resolve and engineer successful solutions to the problems at the interfaces in solid-state batteries.

**Thermal management**. Even if the transference number of the inorganic SEs is near-unity, solid-state batteries still generate a considerable amount of heat due to other processes such as activation overpotentials at the interface, solid diffusion overpo-

tential in the electrode and joule heating from the current collectors and tabs. Significant heat generations cause temperature gradients in large-format solid-state batteries and a mismatch in thermal expansion coefficients of different cell components, and subsequently thermal stresses and cracks. Hence, the thermal management's role in optimising the lifetime performance of solid-state batteries cannot be neglected in future works.

**Novel hybrid solid-state batteries.** Aside from conventional single-phase solid electrolytes, hybrid systems such as solid-liquid or polymer-ceramic composites can be adopted, resulting in a hybrid membrane with tunable properties. In the polymer combined with a ceramic electrolyte, the ceramic provides a high mechanical modulus and high ionic conductivity whilst the polymer makes processing and scale-up easier and improves adhesion with electrodes [288–290]. Conductive polymer binders can improve mechanical flexibility as well as wet the interface.

By adding a few drops of liquid electrolytes, an atomically-wetted interface is thought to be obtained at the PE side, for example with  ${\rm Li_7La_3Zr_2O_{12}/LiCoO_2}$  (where there is a high surface energy mismatch between the two components), whilst the solid electrolyte acts as a protective barrier between the Li metal and the reactive liquid electrolyte [37]. However, several problems are associated with the use of a liquid electrolyte including compromising the energy density; fabrication difficulties relating to handling liquid electrolytes, metal dissolution into the liquid electrolytes from the PE, and also a large impedance at the solid–liquid interface, caused by the formation of a solid–liquid electrolyte interphase due to chemical and electrochemical reactions between phases, which should be addressed if these quasi-solid-state systems are adopted.

Solid-state lithium-sulfur batteries. While this review focuses on solid-state Li-ion batteries, it is also worth noting that significant recent progress has been made to solid-state Li-S batteries, in which the PE is a sulfur-carbon composite instead of an intercalating electrode [291,292]. Li-S batteries could achieve much higher specific energy than Li-ion batteries due to the high specific sulfur capacity. However, they suffer from continuous loss of active materials in a process known as the shuttle, where sulfur dissolves into liquid electrolyte and moves towards NE. Sulfide- and oxide-based SEs have been shown to inhibit shuttle effectively, therefore is a promising route to improving the cyclability of Li-S batteries [293,294]. However, they face many of the same challenges discussed in this paper for solid-state Li-ion batteries such as poor thermodynamic interfacial stability and mechanical stress and fracture induced by the large volumetric change of PE during charge/discharge [295,296]. Latest efforts for solid-state Li-S batteries have been focused on hybrid and composite electrolytes, which seek to combine solid electrolytes' effective inhibition of shuttle and Li filaments growth with liquid or polymer electrolytes' better interfacial properties with the PE [297,298]. To further optimise the performance of these hybrid- and composite-electrolyte Li-S batteries, further mechanistic investigations are required to understand the electrochemical stability and interfacial properties between solid and liquid electrolytes [299].

**Hybrid modelling.** While physics-based models could provide valuable insights into the internal states of solid-state

batteries, this approach requires the estimation of different parameters for the electrodes and the SEs. It is not feasible to measure all these parameters for every cell in real-world battery diagnostics, especially when the model parametrisation challenge is further aggravated by the inherent cell-to-cell variability and the impacts of different operating conditions on the internal states. Therefore, future modelling studies could consider a fusion of physics-based models with machine learning approaches to address the inherent cell-to-cell variability in batteries. The outcome of such hybrid modelling approaches could be used as the basis of advanced state estimation for a smart solid-state battery management and diagnostics.

Advanced simulations and high-throughput calculations. Conventional screening of high-performing SEs is time-consuming and costly. With the development of advanced simulation and computational technologies, new paradigms of material research such as material genomics [300–302], machine learning [39,49,284,285], high-throughput cell designs [303,304] and data mining [305] could open up a new route to exploring new SEs or modifying existing SEs with a high efficiency.

**Intelligent solid-state battery management system.** As discussed in this review, the degradation mechanisms of solid-state batteries are sensitive to different operating conditions such as voltage limits, operating and storage temperatures, stack pressures, critical plating and stripping current densities. However, these operating conditions are often defined individually, which deviate from real-world coupled scenarios. Future works could develop multi-conditional controls, where variable real-world operating conditions could be considered to establish the dynamic limits for smart solid-state battery management system. The CHAIN framework [306], which incorporates multistage real-time prognostics into cell design and manufacturing *via* cloud-based servers, is especially relevant to developing futuristic, intelligent solid-state battery management system.

**Holistic performance evaluation.** This review has highlighted the influence of different mechanisms in solid-state batteries and showed that it is insufficient to consider only one aspect of cell design. To date, most reports have focussed on improving the ionic conductivity in the SE. However, a high ionic conductivity does not necessarily mean a performance

boost, especially when some solid electrolytes such as  $\text{Li}_2\text{S-P}_2\text{S}_5$  have a low chemical stability in air and low electrochemical stability against Li-metal and high voltage PEs. Therefore, future works should include an overall performance evaluation considering electrochemistry, chemical stability, thermal considerations, mechanical effects and their interplay to accelerate the process of upscaling solid-state batteries for practical applications.

## **Acknowledgements**

Mei-Chin Pang and Kai Yang contributed equally to this work. Shichun Yang and Xinhua Liu acknowledge funding from the National Key R&D Program of China (2018YFB0104400) and National Natural Science Foundation of China (No. U1864213). Mei-Chin Pang and Gregory J. Offer acknowledge funding from the Beijing Institute of Aeronautical Materials (BIAM) and the Faraday Institution (EP/S003053/1, Grant No. FIRG003). Kai Yang and Feng Pan acknowledge funding from the National Key R&D Program of China (2016YFB0700600). Rowena Brugge would like to acknowledge the EPSRC for funding from Grant Nos. EP/R024006/1 and EP/P003532/1, and the support of JSPS/EPSRC (EP/P026478/1) Core-to-Core Program (Advanced Research Net- works) 'Solid Oxide Interfaces for Faster Ion Transport (SOIFIT)'. Ainara Aguadero would like to acknowledge the EPSRC for funding for grant projects EP/R024006/1 and EP/ P026478/1 and the support of JSPS/EPSRC EP/P026478//1 project. Ainara Aguadero also wishes to acknowledge the EU commission for the HORIZON 2020 FETPROACT 2018-2020 project 824072. Huizhi Wang acknowledges funding from the Engineering and Physical Sciences Research Council (EP/ S000933/1), Monica Marinescu and Billy Wu acknowledge funding from the Faraday Institution (EP/S003053/1, Grant No. FIRG003).

The authors would like to thank Alexander Hoggan Bergsmo for helpful discussions.

The authors would also like to thank the publishing and typesetting team at Materials Today for improving the final version of this work.

## Appendix A. Definition of general performance metrics

TABLE A.1

| Metrics  | Definitions   | Equation  |
|--|---|---|
| Ionic conductivity, $\sigma_{ m elec}~[{ m S}~{ m cm}^{-1}]$         | The electrolyte resistance to the transport of Li-ions in the SE. $d_{\rm elec}$ is the electrolyte thickness, $A_{\rm elec}$ is the active surface area and $R_{\rm elec}$ is the electrolyte resistance.  | $\sigma_{ m elec} = rac{d_{ m elec}}{A_{ m elec}R_{ m elec}}$  |
| Electronic conductivity, $\sigma_{e^-}$ [S cm <sup>-1</sup> ]        | The electrolyte resistance to the transport of electrons in the SE. $I_{\rm res}$ is the residual current and $\Delta V$ is the applied voltage.  | $\sigma_{\mathrm{e^{-}}} = rac{d_{\mathrm{elec}}I_{\mathrm{res}}}{A_{\mathrm{elec}}\Delta V}$  |
| Relative permittivity, $\epsilon_{ m r}$ [-]                         | The ratio of the absolute permittivity of the medium, $\epsilon$ , to the absolute permittivity of the vacuum, $\epsilon_0$ .   | $\epsilon_{ m f}=rac{\epsilon}{\epsilon_0}$  |
| Specific heat capacity, $C_{ m p}~[{ m J}~{ m kg}^{-1}~{ m K}^{-1}]$ | The amount of heat energy required to raise one unit of temperature of a material per unit of mass.   | Effective specific heat capacity of a cell: $C_{\text{p,eff}} = \frac{\sum_{i} (C_{\text{p,i}} m_i)}{m_{\text{cell}}}$                      |
| Thermal conductivity, $k \text{ [W m}^{-1} \text{ K}^{-1} \text{]}$  | The ability of a material to conduct heat.  | Effective cross-plane thermal conductivity, where $l_i$ and $k_i$ are the thickness and thermal conductivity o each cell component [82,83]: |
|  |   | $k_{	ext{eff},\perp} = rac{l_{	ext{cell}}}{\sum_i (l_i/k_i)}$  |
|  |   | Effective in-plane thermal conductivity [83]: $\sum_{i=1}^{n} a_{i} b_{i}$  |
|  |   | $k_{	ext{eff},\parallel} = rac{\sum_i (l_i k_i)}{l_{	ext{cell}}}$  |
| Young's modulus,<br>E [GPa]  | For a uniaxial deformation ( <i>i.e.</i> , the applied stresses are normal the cross-sectional areas), the coefficient of linear proportionality is known as the Young's modulus. $\sigma_{\rm st}$ denote the applied stress and $\epsilon$ is the strain.   | $E = rac{\sigma_{ m st}}{\epsilon}$  |
| Poisson's ratio,<br>ν [-]  | The tensile stresses cause an axial extension but a transverse contraction, whereas the compressive stress causes an axial contraction but a transverse extension. The relationship of transverse to axial strain can be described by the Poisson's ratio, in which $\Delta x$ , $\Delta y$ and $\Delta z$ are the change of length in the corresponding $xyz$ -coordinate; $x_0$ , $y_0$ and $z_0$ are the original lengths. | $v = \frac{\Delta y/\gamma_0}{\Delta x/x_0} = \frac{\Delta z/z_0}{\Delta x/x_0}$  |
| Shear modulus,<br>G [GPa]  | If the applied stresses are tangential to the cross-sectional areas, the elastic modulus can be described by the shear modulus and the resulting deformation will be a tangent strain $(\gamma = \Delta x/y_0)$ .   | $G = \frac{E}{2(1+v)}$  |
| Bulk modulus,<br>K [GPa]   | If a uniform pressure is applied on all of the surfaces of the solid material, the coefficient that relates the stress and strain in the linear elastic regime is known as the bulk modulus and the deformation is given by the volume strain $(\theta_v = \Delta V/V_0)$ .   | $K = \frac{E}{3(1-2\nu)}$   |
| Hardness, $H_{ m v}$ [GPa]   | The resistance of the material to the plastic deformation, which can be measured with the Vickers indentation. $P_{\rm v}$ is the indentation force and $2a_{\rm v}$ is the indentation diagonal size [94].   | $H_{\rm v} = \frac{1.854 P_{ m v}}{(2 a_{ m v})^2}$   |
| Fracture toughness,  | Critical stress threshold, above which cracks initiate. Fracture  | Mode I (opening mode) fracture toughness:   |
| $K_{\rm c}$ [MPa m <sup>1/2</sup> ]                                  | toughness can be measured using the indentation technique [93]. $k_{\rm V}$ is the Vickers-probe geometry constant ( $k_{\rm V}=0.016$ ) and $c_{\rm V}$ is the crack length.   | $K_{\mathrm{lc}} = k_{\mathrm{v}} \left( \frac{E}{H_{\mathrm{v}}} \right)^{1/2} \left( \frac{P_{\mathrm{v}}}{c_{\mathrm{v}}^{3/2}} \right)$ |

## Appendix B. Acronyms:

| SE              | Solid Electrolyte  |
|-----------------|--|
| PE              | Positive Electrode   |
| NE NE           | Negative Electrode   |
| AM              | Active Materials   |
| SOC             | State-of-Charge  |
| OCP             | Open-Circuit Potential   |
| Li <sup>+</sup> | lithium-ions   |
| PDE             | Partial Differential Equations   |
| AEF             | Area Enhancement Factor  |
| PNP             | Poisson-Nernst-Planck  |
| BV              | Butler-Volmer  |
| FBV<br>DFT      | Frumkin-Butler–Volmer  |
| MD              | Density Functional Theory Molecular Dynamics   |
| LiPON           | Lithium Phosphorus OxyNitride  |
| LLZO            | Li <sub>7</sub> La <sub>3</sub> Zr <sub>2</sub> O <sub>12</sub>                            |
| LATP            | Li <sub>1.2</sub> Al <sub>0.2</sub> Ti <sub>1.8</sub> (PO <sub>4</sub> ) <sub>3</sub>      |
| LPS             | Li <sub>2</sub> S-P <sub>2</sub> S <sub>5</sub>  |
| LSS             | Li <sub>4</sub> SnS <sub>4</sub>   |
| LGPS            | Li <sub>10</sub> GeP <sub>2</sub> S <sub>12</sub>  |
| CCD             | Critical Current Density   |
| LAGP            | $\operatorname{Li}_{1+x}\operatorname{Al}_x\operatorname{Ge}_{2-x}(\operatorname{PO}_4)_3$ |
| SPE             | Solid Polymer Electrolytes   |
| GPE             | Gel Polymer Electrolytes   |
| DME             | 1,2-DiMethoxyEthane  |
| DOL             | 1,3-DiOxoLane  |
| EC/DMC          | Ethylene Carbonate/DiMethyl Carbonate  |
| PEO             | Poly(Ethylene Oxide)   |
| LCO             | LiCoO <sub>2</sub>   |
| LMO             | LiMn <sub>2</sub> O <sub>4</sub>   |
| NMC             | $LiNi_{1-x-y}Mn_xCo_yO_2$  |
| NCA             | $LiNi_{1-x-y}Co_xAl_yO_2$  |
| Li-S<br>CEI     | Lithium-Sulfur Cathode Electrolyte Interphase  |
| SEI             | Solid Electrolyte Interphase   |
| EIS             | Electrochemical Impedance Spectroscopy   |
| DRT             | Distribution Function of Relaxation Times  |
| NLEIS           | Non-Linear Electrochemical Impedance Spectroscopy  |
| GIΠ             | Galvanostatic Intermittent Titration Technique   |
| PEIS            | Potentiostatic Electrochemical Impedance Spectroscopy                                      |
| GEIS            | Galvanostatic Electrochemical Impedance Spectroscopy                                       |
| MTRM            | Modulated Thermoreflectance Microscopy   |
| SRXTM           | Synchrotron Radiation X-ray Tomographic Microscopy   |
| NDP             | Neutron Depth Profiling  |
| SEM             | Scanning Electron Microscopy   |
| TEM             | Transmission Electron Microscopy   |
| EELS<br>STEM    | Electron Energy Loss Spectroscopy  |
| XPS             | Scanning Transmission Electron Microscopy X-ray Photoelectron Spectroscopy                 |
| XRD             | X-ray Diffraction  |
| ToF-SIMS        | Time of Flight - Secondary Ion Mass Spectrometry   |
| SIMS            | Secondary Ion Mass Spectrometry  |
| ALD             | Atomic Layer Deposition  |
| PVD             | Physical Vapour Deposition   |
| USV             | Ultrasonic Sound Velocity  |
| RUS             | Resonant Ultrasound Spectroscopy   |
| PUS             | Picosecond Ultrasonic Spectroscopy   |
| DSC             | Differential Scanning Calorimetry  |
| ARC             | Accelerating Rate Calorimeter  |
| CV              | Cyclic Voltammetry   |
| DEMS            | Differential Electrochemical Mass Spectrometry   |
| NMR             | Nuclear Magnetic Resonance   |
| FIB-SEM         | Focussed-Ion-Beam Scanning Electron Microscopy   |
| XCT<br>EDV      | X-ray Tomography   |
| EDX<br>CRSS     | Energy-Dispersive X-ray spectroscopy Critical Resolved Shear Stress                        |
| CIO             | Chilical Nesolived Shear Stress  |
|                 |  |

#### References

- [1] N. Kamaya et al., Nature Mater. 10 (2011) 682-686.
- [2] Y. Kato et al., Nature Energy 1 (2016) 16030, https://doi.org/10.1038/ nenergy.2016.30.
- [3] A. Varzi et al., J. Mater. Chem. A 4 (2016) 17251-17259.
- [4] T.B. Reddy, D. Linden, D.H.O.B. Linden, Linden's handbook of batteries, 4th edn,., McGraw-Hill, New York and London, 2011. https://www.worldcat.org/ title/lindens-handbook-of-batteries/oclc/692762479.
- [5] J. Janek, W.G. Zeier, Nature Energy 1 (2016) 16141, https://doi.org/10.1038/ nenergy.2016.141.
- [6] D. Rettenwander et al., Chem. Materials 28 (2016) 2384-2392.
- [7] L. Cheng et al., ACS Appl. Mater. Interfaces 7 (2015) 2073-2081.
- [8] J.B. Bates et al., J. Power Sources 43 (1993) 103-110.
- [9] X. Han et al., Nature Mater. 16 (2017) 572-579.
- [10] A. Sharafi et al., Chem. Mater. 29 (2017) 7961-7968.
- [11] F. Han et al., Advanced Energy Materials 8 (2018) 1703644, https://doi.org/ 10.1038/nenergy.2016.141.
- [12] F. Han et al., Nature Energy 4 (2019) 187–196.
- [13] J. Kasemchainan et al., Nature Mater. 18 (2019) 1105-1111.
- [14] E. Kazyak et al., Matter 2 (2020) 1025-1048.
- [15] F. Aguesse et al., ACS Appl. Mater. Interfaces 9 (2017) 3808–3816, https://doi. org/10.1021/acsami.6b13925.
- [16] J.A. Lewis et al., ACS Energy Lett. 4 (2019) 591–599, https://doi.org/10.1021/acsenergylett.9b00093.
- [17] X. Yu et al., J. Electrochem. Soc. 144 (1997) 524, https://doi.org/10.1149/ 1.1837443.
- [18] M.-C. Pang et al., J. Electrochem. Soc. (2020), https://doi.org/10.1149/1945-7111/abd493.
- [19] H.-C. Yu et al., J. Power Sources 440 (2019) 227116, https://doi.org/10.1016/j. jpowsour.2019.227116.
- [20] J. Tippens et al., ACS Energy Lett. 4 (2019) 1475–1483, https://doi.org/ 10.1021/acsenergylett.9b00816.
- [21] A. Masias et al., J. Mater. Sci. 54 (2019) 2585–2600, https://doi.org/10.1007/ s10853-018-2971-3.
- [22] G. Bucci et al., Phys. Rev. Mater. 2 (2018) 1–11, https://doi.org/10.1103/ PhysRevMaterials.2.105407.
- [23] S. Yu et al., Chem. Mater. 28 (2016) 197–206, https://doi.org/10.1021/acs. chemmater.5b03854.
- [24] L. Raijmakers et al., Electrochim. Acta 330 (2020) 135147, https://doi.org/ 10.1016/j.electacta.2019.135147.
- [25] A. Bielefeld, D.A. Weber, J. Janek, J. Phys. Chem. C 123 (2019) 1626–1634, https://doi.org/10.1021/acs.jpcc.8b11043.
- [26] Ö.U. Kudu et al., J. Power Sources 407 (2018) 31–43, https://doi.org/10.1016/j. ipowsour.2018.10.037.
- [27] J. Lau et al., Adv. Energy Mater. 8 (2018) 1800933, https://doi.org/10.1002/aenm.201800933.
- [28] T. Baba, Y. Kawamura, Front. Energy Res. 4 (2016) 665, https://doi.org/ 10.3389/fenrg.2016.00022.
- [29] A. Kato et al., ACS Appl. Energy Mater. 1 (2018) 1002–1007, https://doi.org/ 10.1021/acsaem.7b00140.
- [30] W. Fitzhugh, L. Ye, X. Li, J. Mater. Chem. A 7 (2019) 23604–23627, https://doi. org/10.1039/C9TA05248H.
- [31] R. Raj, J. Wolfenstine, J. Power Sources 343 (2017) 119–126, https://doi.org/ 10.1016/j.jpowsour.2017.01.037.
- [32] C.-L. Tsai et al., ACS Appl. Mater. Interfaces 8 (2016) 10617–10626, https://doi. org/10.1021/acsami.6b00831.
- [33] G. Li, C.W. Monroe, PCCP 21 (2019) 20354–20359, https://doi.org/10.1039/ C9CP03884A.
- [34] J.C. Bachman et al., Chem. Rev. 116 (2016) 140–162, https://doi.org/10.1021/acs.chemrev.5b00563.
- [35] X.-B. Cheng et al., Chem. Rev. 117 (2017) 10403–10473, https://doi.org/ 10.1021/acs.chemrev.7b00115.
- [36] T. Famprikis et al., Nature Mater. 18 (2019) 1278–1291, https://doi.org/ 10.1038/s41563-019-0431-3.
- [37] A. Banerjee et al., Chem. Rev. 120 (2020) 6878–6933. https://pubs.acs.org/doi/abs/10.1021/acs.chemrev.0c00101.
- [38] Y. Xiao et al., Nature Rev. Mater. 5 (2020) 105–126, https://doi.org/10.1038/ s41578-019-0157-5.
- [39] A.D. Sendek et al., Chemistry of materials: a publication of the American Chemical Society 31 (2019) 342–352, https://doi.org/10.1021/acs. chemmater.8b03272.

- [40] Y.-H. Chiang et al., J. Power Sources 196 (2011) 3921–3932, https://doi.org/ 10.1016/j.jpowsour.2011.01.005.
- [41] T. Momma et al., J. Power Sources 216 (2012) 304–307, https://doi.org/ 10.1016/j.jpowsour.2012.05.095.
- [42] R.R. Richardson, P.T. Ireland, D.A. Howey, J. Power Sources 265 (2014) 254–261, https://doi.org/10.1016/j.jpowsour.2014.04.129.
- [43] S. Alavi, C.R. Birkl, D.A. Howey, J. Power Sources 288 (2015) 345–352, https://doi.org/10.1016/j.jpowsour.2015.04.099.
- [44] S.D. Fabre et al., J. Electrochem. Soc. 159 (2012) A104, https://doi.org/10.1149/ 2.041202jes.
- [45] R. Garcia-Mendez et al., Electrochim. Acta 237 (2017) 144–151, https://doi.org/ 10.1016/j.electacta.2017.03.200.
- [46] C. Loho et al., J. Electrochem. Soc. 164 (2017) A6131–A6139, https://doi.org/ 10.1149/2.0201701jes.
- [47] P. Braun et al., J. Power Sources 393 (2018) 119–127, https://doi.org/10.1016/j. jpowsour.2018.04.111.
- [48] S. Larfaillou et al., J. Power Sources 319 (2016) 139–146, https://doi.org/ 10.1016/j.jpowsour.2016.04.057.
- [49] A.D. Sendek et al., Energy Environ. Sci. 10 (2017) 306–320, https://doi.org/ 10.1039/C6EE02697D.
- [50] K.B. Hatzell et al., ACS Energy Lett. 5 (2020) 922-934.
- [51] A.S. Westover et al., ACS Energy Lett. 4 (2019) 651–655, https://doi.org/ 10.1021/acsenergylett.8b02542.
- [52] E. Markevich et al., ACS Energy Lett. 2 (2017) 1321–1326, https://doi.org/ 10.1021/acsenergylett.7b00300.
- [53] C.S. Nimisha et al., Solid State Ionics 185 (2011) 47–51, https://doi.org/ 10.1016/j.ssi.2011.01.001.
- [54] H. Muramatsu et al., Solid State Ionics 182 (2011) 116–119, https://doi.org/ 10.1016/j.ssi.2010.10.013.
- [55] A. Sharafi et al., J. Mater. Chem. A 5 (2017) 13475–13487, https://doi.org/ 10.1039/C7TA03162A.
- [56] M.J. Wang, R. Choudhury, J. Sakamoto, Joule 3 (2019) 2165–2178, https://doi. org/10.1016/j.joule.2019.06.017.
- [57] F. Han et al., Adv. Energy Mater. 6 (2016) 1501590, https://doi.org/10.1002/aenm.201501590.
- [58] M.-C. Pang et al., PCCP 21 (2019) 22740–22755, https://doi.org/10.1039/ C9CP03886H.
- [59] Y. Zhu, X. He, Y. Mo, ACS Appl. Mater. Interfaces 7 (2015) 23685–23693.
- [60] Y. Zhu, X. He, Y. Mo, J. Mater. Chem. A 4 (2016) 3253-3266.
- [61] W.D. Richards et al., Chem. Mater. 28 (2016) 266–273, https://doi.org/ 10.1021/acs.chemmater.5b04082.
- [62] T. Shi et al., Adv. Energy Mater. 10 (2020) 1902881.
- [63] R. Chen et al., Joule 4 (2020) 812–821. https://www.sciencedirect.com/science/article/pii/S2542435120301276.
- [64] L. Cheng et al., PCCP 16 (2014) 18294.
- [65] Y. Zhu et al., Adv. Energy Mater. 9 (2019) 1803440.
- [66] R.H. Brugge et al., Chem. Mater. 30 (2018) 3704–3713, https://doi.org/ 10.1021/acs.chemmater.8b00486.
- [67] R. Brugge et al., J. Mater. Chem. A (2020).
- [68] J. Maier, Prog. Solid St. Chem. 23 (1995) 171–263. https://www.sciencedirect.com/science/article/pii/007967869500004E.
- [69] J.S. Newman, K.E. Thomas-Alyea, Electrochemical systems, Wiley, Hoboken, N. J. and Chichester, 3rd edn, 2004. .
- [70] S. Braun, C. Yada, A. Latz, J. Phys. Chem. C 119 (2015) 22281–22288.
- [71] N.J.J. Klerk, M. Wagemaker, ACS Appl. Energy Mater. 1 (2018) 5609–5618.
- [72] T.H. Wan, F. Ciucci, Electrochim. Acta 331 (2020) 135355.
- [73] W. Bucheli et al., PCCP 16 (2014) 15346-15354.
- [74] Z. Wang et al., J. Power Sources 324 (2016) 342–348. https://www.sciencedirect.com/science/article/pii/S0925838816323672.
- [75] I.D. Campbell et al., J. Electrochem. Soc. 166 (2019) A725, https://doi.org/ 10.1149/2.0821904jes.
- [76] J. Li et al., Adv. Energy Mater. 5 (2015) 1401408.
- [77] H. Tsukasaki et al., J. Power Sources 434 (2019) 226714.
- [78] H. Tsukasaki et al., J. Power Sources 479 (2020) 228827.
- [79] T.M. Bandhauer, S. Garimella, T.F. Fuller, J. Power Sources 158 (2011) R1, https://doi.org/10.1149/1.3515880.
- [80] F. Xu et al., J. Appl. Phys. 113 (2013) 244304.
- [81] E.A. Il'ina, A.A. Raskovalov, O.G. Reznitskikh, J. Chem. Thermodyn. 128 (2019) 68–73.
- [82] C.R. Pals, J. Newman, J. Electrochem. Soc. 142 (1995) 3274, https://doi.org/ 10.1149/1.2049974.
- [83] L. Song, J.W. Evans, J. Electrochem. Soc. 147 (2000) 2086–2095.

- [84] H. Maleki et al., J. Electrochem. Soc. 146 (1999) 947-954.
- [85] R. Bock et al., Energies 13 (2020) 253.
- [86] H. Yang et al., J. Phys. Chem. Lett. 10 (2019) 5552–5556, https://doi.org/ 10.1021/acs.jpclett.9b02073.
- [87] G. Offer et al., Nature 582 (2020) 485–487. https://www.nature.com/articles/d41586-020-01813-8.
- [88] Y. Zhao et al., J. Electrochem. Soc. 166 (2019) A2849–A2859. https://iopscience.iop.org/article/10.1149/2.0501913jes.
- [89] A.A. Hubaud et al., J. Alloy. Compd. 644 (2015) 804–807. https://www.sciencedirect.com/science/article/pii/S0925838815013602.
- [90] A. Shużalec, Introduction to Nonlinear Thermomechanics, Springer London, London, 1992.
- [91] E.G. Herbert et al., Thin Solid Films 520 (2011) 413–418. https://www.sciencedirect.com/science/article/pii/S0040609011014556.
- [92] E.J. Cheng et al., J. Asian Ceramic Soc. 5 (2017) 113–117. https://www.sciencedirect.com/science/article/pii/S2187076417300271.
- [93] F.P. McGrogan et al., Adv. Energy Mater. 7 (2017) 1602011.
- [94] J.E. Ni et al., J. Mater. Sci. 47 (2012) 7978–7985. https://link.springer.com/ article/10.1007%2Fs10853-012-6687-5.
- [95] C. Xu et al., Proc. National Acad. Sci. USA 114 (2017) 57–61. https://www.sciencedirect.com/science/article/pii/S0042207X17300854.
- [96] K. Minami et al., Solid State Ionics 178 (2007) 837-841.
- [97] T. Wang et al., J. Mater. Chem. A 7 (2019) 17008-17013.
- [98] C. Dietrich et al., J. Mater. Chem. A 5 (2017) 18111–18119. https://pubs.rsc. org/en/content/articlelanding/2017/TA/C7TA06067J#!divAbstract.
- [99] A. Sakuda et al., J. Ceramic Society Japan 121 (2013) 946–949. https://www.jstage.jst.go.jp/article/jcersj2/121/1419/121\_JCSJ-P13125/\_article.
- [100] J. Wolfenstine et al., Mater. Lett. 96 (2013) 117–120. https://www.sciencedirect.com/science/article/pii/S0167577X13000402.
- [101] W.S. LePage et al., J. Electrochem. Soc. 166 (2019) A89-A97.
- [102] C. Monroe, J. Newman, Electrochim. Acta 152 (2005) A396.
- [103] E.J. Cheng, A. Sharafi, J. Sakamoto, Electrochim. Acta 223 (2017) 85-91.
- [104] L. Porz et al., Advanced Energy Materials 7 (2017) 1701003.
- [105] T. Swamy et al., J. Electrochem. Soc. 165 (2018) A3648-A3655.
- [106] Y. Qi, C. Ban, S.J. Harris, Joule (2020) 2599–2608.
- [107] M.W. Barsoum, Fundamentals of ceramics, McIOP, Bristol, 2003.
- [108] H.-K. Tian, Y. Qi, J. Electrochem. Soc. 164 (2017) E3512–E3521.
- [109] S.F. Pugh, Science 45 (1954) 823-843.
- [110] M. Song, X. Liu, L. Liu, Materials (Basel, Switzerland), 2017, 10, 1-18. .
- [111] W. Zhang et al., ACS Appl. Mater. Interfaces 9 (2017) 35888-35896.
- [112] F. Strauss et al., ACS Energy Lett. 3 (2018) 992–996.
- [113] R. Koerver et al., J. Mater. Chem. A 5 (2017) 22750–22760. https://pubs.rsc. org/en/content/articlelanding/2017/TA/C7TA07641J#!divAbstract.
- [114] S.H. Jung et al., Adv. Energy Mater. 10 (2020) 1903360.
- [115] A. Mukhopadhyay, B.W. Sheldon, Prog. Mater Sci. 63 (2014) 58–116. https://www.sciencedirect.com/science/article/pii/S0079642514000139.
- [116] R. Koerver et al., Energy Environ. Sci. 11 (2018) 2142–2158.
- [117] M. Otoyama et al., J. Phys. Chem. Letters 11 (2020) 900–904, https://doi.org/ 10.1021/acs.jpclett.9b03456.
- [118] C. Chen et al., Adv. Energy Mater. 8 (2018) 1801430.
- [119] G. Bucci et al., J. Mater. Chem. A 5 (2017) 19422–19430. https://pubs.rsc.org/en/content/articlelanding/2017/TA/C7TA03199H#!divAbstract.
- [120] T. Liu et al., Electrochem. Commun. 79 (2017) 1-4.
- [121] R. Behrou, K. Maute, J. Electrochem. Soc. 164 (2017) A2573–A2589. https://iopscience.iop.org/article/10.1149/2.1101712jes.
- [122] R. Chen et al., Chem. Rev. (2019) 6820–6877, https://doi.org/10.1021/acs. chemrev.9b00268.
- [123] N. Sun et al., Angew. Chem. Int. Ed. 58 (2019) 18647–18653, https://doi.org/ 10.1002/anie.201910993.
- $\boldsymbol{[124]}\,$  X. Wu et al., Advanced Energy Materials 9 (2019) 1901547.
- [125] Q. Li et al., Nano Energy 63 (2019) 103895.
- [126] M. Klinsmann et al., J. Power Sources 442 (2019) 227226 . https://www.scopus.com/record/display.uri?eid=2-s2.0-85106252818&origin=inward.
- [127] Q. Xia et al., Small 14 (2018) 1804149.
- [128] T. Ohsaki et al., J. Power Sources 146 (2005) 97–100. https:// www.sciencedirect.com/science/article/pii/S0378775305005112.
- [129] J. Chen, C. Buhrmester, J.R. Dahn, Electrochem. Solid-State Lett. 8 (2005) A59.
- [130] C. Qi et al., J. Electrochem. Soc. 165 (2018) A3985–A3992. https://iopscience.iop.org/article/10.1149/2.0911816jes.
- [131] C.-H. Doh et al., J. Power Sources 175 (2008) 881–885. https:// www.sciencedirect.com/science/article/pii/S0378775307020290.
- [132] J. Shu et al., J. Solid State Electrochem. 16 (2012) 819–824. https://link. springer.com/article/10.1007%2Fs10008-011-1484-7.

- [133] J. Nelson Weker et al., Electrochim. Acta 247 (2017) 977-982.
- [134] F. Strauss et al., ACS Appl. Mater. Interfaces 12 (2020) 20462–20468, https://doi.org/10.1021/acsami.0c02872.
- [135] T. Bartsch et al., ACS Energy Lett. 3 (2018) 2539–2543, https://doi.org/ 10.1021/acsenergylett.8b01457.
- [136] J.-M. Doux et al., Adv. Energy Mater. 10 (2020) 1903253. https://pubs.rsc.org/en/content/articlelanding/2020/TA/C9TA12889A#ldivAbstract.
- [137] J.-M. Doux et al., J. Mater. Chem. A 8 (2020) 5049-5055.
- [138] A.J. Samson et al., Energy Environ. Sci. 12 (2019) 2957–2975. https://pubs.rsc. org/en/content/articlelanding/2019/EE/C9EE01548E#ldivAbstract.
- [139] K. Park et al., Chem. Mater. 28 (2016) 8051–8059, https://doi.org/10.1021/acs. chemmater.6b03870.
- [140] E.G. Herbert et al., J. Mater. Res. 34 (2019) 3593–3616. https://link. springer.com/article/10.1557%2Fjmr.2019.313.
- [141] M. Wang, J. Sakamoto, J. Power Sources 377 (2018) 7–11. https:// www.sciencedirect.com/science/article/pii/S0378775317315616.
- [142] H. Chung, B. Kang, Chem. Mater. 29 (2017) 8611–8619, https://doi.org/ 10.1021/acs.chemmater.7b02301.
- [143] D. Spencer Jolly et al., ACS Appl. Mater. Interfaces 12 (2020) 678–685.
- [144] F. Sun et al., J. Mater. Chem. A 6 (2018) 22489–22496. https://pubs.rsc.org/en/content/articlelanding/2018/TA/C8TA08821G#!divAbstract.
- [145] F. Mo et al., Advanced Energy Materials 9 (2019) 1902123.
- [146] P. Hartmann et al., J. Phys. Chem. C 117 (2013) 21064–21074, https://doi.org/ 10.1021/jp4051275.
- [147] S. Wenzel et al., Chem. Mater. 28 (2016) 2400–2407, https://doi.org/10.1021/
- [148] C. Ma et al., Nano letters 16 (2016) 7030–7036, https://doi.org/10.1021/ acs.nanolett.6b03223.
- [149] J. Auvergniot et al., Chem. Mater. 29 (2017) 3883–3890, https://doi.org/ 10.1021/acs.chemmater.6b04990.
- [150] A. Schwöbel, R. Hausbrand, W. Jaegermann, Solid State Ionics 273 (2015) 51–54.
- [151] H. Xu et al., Nano letters 18 (2018) 7414–7418, https://doi.org/10.1021/ acs.nanolett.8b03902.
- [152] T. Lapp, S. Skaarup, A. Hooper, Solid State Ionics 11 (1983) 97–103. https://www.sciencedirect.com/science/article/abs/pii/0167273883900450.
- [153] W. Li et al., Energy & Environmental Science 3 (2010) 1524. https://pubs.rsc. org/en/content/articlelanding/2010/EE/c0ee00052c#!divAbstract.
- [154] M. Aydinol et al., Physical Review B Condensed Matter and Materials Physics 56 (1997) 1354–1365.
- [155] A. Urban, D.H. Seo, G. Ceder, NPJ Comput. Mater. 2 (2016) 1-13.
- [156] M. Du et al., Energy Environ. Sci. 12 (2019) 1780. https://pubs.rsc.org/en/content/articlelanding/2019/EE/C9EE00515C#!divAbstract.
- [157] T. Krauskopf et al., Advanced Energy Materials 9 (2019) 1902568. https://www.scopus.com/record/display.uri?eid=2-s2.0-85088708197&origin=inward.
- [158] A.L. Santhosha et al., Batteries Supercaps 2 (2019) 524–529, https://doi.org/ 10.1002/batt.201800149.
- [159] Y. Li et al., Angewandte Chemie International Edition 56 (2017) 753–756. https://www.sciencedirect.com/science/article/pii/S0045653517309578.
- [160] W. Luo et al., Adv. Mater. 29 (2017) 1606042. https://www.scopus.com/record/display.uri?eid=2-s2.0-85067044606&origin=inward.
- [161] L. Yang et al., Small Methods 4 (2020) 1900751, https://doi.org/10.1145/ 3393691.3394207.
- [162] Y. Gao et al., Angew. Chem. Int. Ed. Engl. 57 (2018) 13608–13612, https://doi. org/10.1002/anie.201807304.
- [163] R. Xu et al., Nano Energy 53 (2018) 958–966. https:// www.sciencedirect.com/science/article/pii/S2211285518307067.
- [164] N.W. Li et al., Angewandte Chemie International Edition 57 (2018) 1505– 1509. https://www.scopus.com/record/display.uri?eid=2-s2.0-85040001982&origin=inward.
- [165] A. Sakuda, A. Hayashi, M. Tatsumisago, Chem. Mater. 22 (2010) 949–956, https://doi.org/10.1021/cm901819c.
- [166] F. Walther et al., Chem. Mater. 31 (2019) 3745–3755, https://doi.org/10.1021/acs.chemmater.9b00770.
- [167] A.-Y. Kim et al., Chem. Mater. 31 (2019) 9664–9672, https://doi.org/10.1021/acs.chemmater.9b02947.
- [168] C. Wang et al., Small Methods 3 (2019) 1900261.
- [169] J.H. Woo et al., J. Electrochem. Soc. 159 (2012) A1120. https://iopscience.iop. org/article/10.1149/2.085207jes.
- [170] S. Yubuchi et al., Solid State Ionics 285 (2016) 79–82. https:// www.sciencedirect.com/science/article/pii/S0167273815002982.
- [171] S.H. Jung et al., Chem. Mater. 30 (2018) 8190–8200, https://doi.org/10.1021/acs.chemmater.8b03321.

- [172] F. Mizuno et al., J. Electrochem. Soc. 152 (2005) A1499. https://iopscience.iop. org/article/10.1149/1.1939633.
- [173] F. Mizuno et al., J. Power Sources 146 (2005) 711–714. https:// www.sciencedirect.com/science/article/pii/S0378775305004623.
- [174] S. Hong et al., Ceram. Int. 41 (2015) 5066–5071. https:// www.sciencedirect.com/science/article/pii/S027288421401997X.
- [175] J.E. Trevey et al., Electrochem. Solid-State Lett. 13 (2010) A154. https://iopscience.iop.org/article/10.1149/1.3479551.
- [176] F. Strauss et al., RSC Adv. 10 (2020) 1114–1119. https://pubs.rsc.org/en/content/articlelanding/2020/RA/C9RA10253A#ldivAbstract.
- [177] G. Oh et al., Chem. Mater. 28 (2016) 2634–2640, https://doi.org/10.1021/acs. chemmater.5b04940.
- [178] K. Yoon et al., Sci. Rep. 8 (2018) 8066. https://www.scopus.com/record/display.uri?eid=2-s2.0-85106210463&origin=inward.
- [179] H. Koshikawa et al., J. Power Sources 376 (2018) 147–151. https://www.sciencedirect.com/science/article/pii/S0378775317315653.
- [180] M.B. Dixit et al., ACS Appl. Energy Mater. (2020) 9534–9542, https://doi.org/ 10.1021/acsaem.0c02053.
- [181] T. Krauskopf et al., ACS Appl. Mater. Interfaces 11 (2019) 14463–14477.
- [182] F. Shen et al., ACS Energy Lett. 3 (2018) 1056–1061, https://doi.org/10.1021/acsenergylett.8b00249.
- [183] S. Kim et al., Adv. Energy Mater. 10 (2020) 1903993.
- [184] H. Zheng et al., Adv. Funct. Mater. 30 (2020) 1906189.
- [185] P. Barai et al., J. Electrochem. Soc. 166 (2019) A1752–A1762. https://iopscience.iop.org/article/10.1149/2.0321910jes.
- [186] Y. Ren et al., Electrochem. Commun. 57 (2015) 27-30.
- [187] S. Yu, D.J. Siegel, ACS Appl. Mater. Interfaces 10 (2018) 38151–38158, https://doi.org/10.1021/acsami.8b17223.
- [188] F.M. Pesci et al., J. Mater. Chem. A 6 (2018) 19817–19827. https://pubs.rsc.org/en/content/articlelanding/2018/TA/C8TA08366E#!divAbstract.
- [189] A. Sharafi et al., J. Mater. Chem. A 5 (2017) 21491–21504. https://www.
- scopus.com/record/display.uri?eid=2-s2.0-85031672201&origin=inward.
  [190] L. Cheng et al., ACS Appl. Mater. Interfaces 7 (2015) 17649–17655, https://doi.
- org/10.1021/acsami.5b02528.
  [191] P. Barai, K. Higa, V. Srinivasan, J. Electrochem. Soc. 165 (2018) A2654–A2666.
- www.sciencedirect.com/science/article/pii/S0378775313007830.

  [193] B.R. Shin et al., Electrochim. Acta 146 (2014) 395–402. https://
- www.sciencedirect.com/science/article/pii/S0013468614018337.
  [194] T. Inoue, K. Mukai, ACS Appl. Mater. Interfaces 9 (2017) 1507–1515, https://
- doi.org/10.1021/acsami.6b13224.
- [195] Y. Iriyama et al., Solid State Ionics 176 (2005) 2371–2376. https:// www.sciencedirect.com/science/article/pii/S0167273805002857.
- [196] P. Bron, B. Roling, S. Dehnen, J. Power Sources 352 (2017) 127–134. https://www.sciencedirect.com/science/article/pii/S037877531730410X.
- [197] Q. Li et al., Nano Energy 63 (2019) 103895.
- [198] L.E. Marbella et al., Chem. Mater. 31 (2019) 2762–2769, https://doi.org/ 10.1021/acs.chemmater.8b04875.
- [199] Y.-X. Song et al., Energy Environ. Sci. 12 (2019) 2496–2506.
- [200] Y. Matsuda et al., Solid State Ionics 335 (2019) 7–14. https:// www.sciencedirect.com/science/article/pii/S0167273818310579.
- [201] L. Sang et al., Chem. Mater. 29 (2017) 3029–3037, https://doi.org/10.1021/acs. chemmater.7b00034.
- [202] M. Otoyama et al., Chem. Lett. 45 (2016) 810–812, https://doi.org/10.1246/ cl.160299.
- [203] M. Otoyama et al., J. Power Sources 302 (2016) 419–425. https:// www.sciencedirect.com/science/article/pii/S0378775315304274.
- [204] C.L. Tsai et al., Sustainable Energy and Fuels 3 (2019) 280–291. https://pubs.rsc.org/en/content/articlelanding/2019/SE/C8SE00436F#!divAbstract.
- [205] F. Sagane et al., J. Power Sources 233 (2013) 34–42. https://www.sciencedirect.com/science/article/pii/S0378775313000888.
- [206] H. Tllez et al., J. Anal. At. Spectrom. 29 (2014) 1361.
- [207] G. Vardar et al., Chem. Mater. 30 (2018) 6259–6276, https://doi.org/10.1021/acs.chemmater.8b01713.
- [208] S. Wang et al., J. Am. Chem. Soc. 140 (2018) 250–257, https://doi.org/ 10.1021/jacs.7b09531.
- [209] M.F. Groh et al., Chem. Mater. 30 (2018) 5886–5895, https://doi.org/10.1021/acs.chemmater.8b01746.
- [210] C. Yu et al., J. Am. Chem. Soc. 138 (2016) 11192–11201, https://doi.org/ 10.1021/jacs.6b05066.
- [211] P.-H. Chien et al., J. Phys. Chem. Letters 9 (2018) 1990-1998.

- [212] Z. Wang et al., Nano letters 16 (2016) 3760–3767, https://doi.org/10.1021/acs.nanolett.6b01119.
- [213] A. Sakuda, A. Hayashi, M. Tatsumisago, Chem. Mater. 22 (2010) 949-956.
- [214] S. Wenzel et al., Solid State Ionics 278 (2015) 98–105. https:// www.sciencedirect.com/science/article/pii/S0167273815002349.
- [215] W. Zhang et al., J. Mater. Chem. A 5 (2017) 9929–9936. https://pubs.rsc.org/en/content/articlelanding/2017/TA/C7TA02730C#!divAbstract.
- [216] L. Miara et al., ACS Applied Materials and Interfaces 8 (2016) 26842–26850, https://doi.org/10.1021/acsami.6b09059.
- [217] M. Donders et al., J. Electrochem. Soc. 160 (2013) A3066–A3071. https://iopscience.iop.org/article/10.1149/2.011305jes.
- [218] M. Chen, S. Adams, J. Solid State Electrochem. 19 (2015) 697-702.
- [219] J. Gao et al., Adv. Funct. Mater. 2020 (1918) 200.
- [220] Y. Song et al., Advanced Energy Materials 9 (2019) 1900671.
- [221] Y. Li et al., Small Methods 4 (2020) 2000111.
- [222] N. Grillon et al., J. Electrochem. Soc. 162 (2015) A2847–A2853. https://iopscience.iop.org/article/10.1149/2.0971514jes.
- [223] A.A. Talin et al., ACS Appl. Mater. Interfaces 8 (2016) 32385–32391, https://doi.org/10.1021/acsami.6b12244.
- [224] J.W. Long et al., Chem. Rev. 104 (2004) 4463–4492. https://www.scopus.com/record/display.uri?eid=2-s2.0-7644220430&origin=inward.
- [225] A. Pearse et al., ACS nano 12 (2018) 4286–4294, https://doi.org/10.1021/acsnano.7b08751.
- [226] J.B. Bates et al., Solid State Ionics 135 (2000) 33–45. https://www.sciencedirect.com/science/article/pii/S0167273800003271.
- [227] B.J. Neudecker, N.J. Dudney, J.B. Bates, J. Electrochem. Soc. 147 (2000) 517–523. https://www.scopus.com/record/display.uri?eid=2-s2.0-0034140118&origin=inward.
- [228] T. Brousse et al., Ionics 3 (1997) 332–337. https://www.scopus.com/record/display.uri?eid=2-s2.0-0000223451&origin=inward.
- [229] I.A. Courtney, J.R. Dahn, J. Electrochem. Soc. 144 (1997) 2045. https://iopscience.iop.org/article/10.1149/1.1837740.
- [230] M. Doyle, T.F. Fuller, J. Newman, Electrochim. Acta 39 (1994) 2073–2081. https://www.sciencedirect.com/science/article/abs/pii/0013468694850917.
- [231] J. Evans, C.A. Vincent, P.G. Bruce, Polymer 28 (1987) 2324–2328. https://www.sciencedirect.com/science/article/abs/pii/0032386187903946.
- [232] K.E. Thomas-Alyea, J. Electrochem. Soc. 165 (2018) A1523–A1528. https://iopscience.iop.org/article/10.1149/2.1151807jes.
- [233] K. Smith, C.-Y. Wang, J. Power Sources 160 (2006) 662–673. https://www.sciencedirect.com/science/article/pii/S0378775306001017.
- [234] S. Zugmann et al., Electrochim. Acta 56 (2011) 3926–3933. https:// www.sciencedirect.com/science/article/pii/S0013468611002374.
- [235] K.M. Diederichsen, E.J. McShane, B.D. McCloskey, ACS Energy Lett. 2 (2017) 2563–2575, https://doi.org/10.1021/acsenergylett.7b00792.
- [236] M. Rossi et al., Electrochim. Acta 258 (2017) 241–254. https://www.sciencedirect.com/science/article/pii/S001346861732145X.
- [237] J. Lück, A. Latz, PCCP 20 (2018) 27804–27821. https://www.scopus.com/record/display.uri?eid=2-s2.0-85106324035&origin=inward.
- [238] J. Lück, A. Latz, PCCP 21 (2019) 14753–14765. https://www.scopus.com/record/display.uri?eid=2-s2.0-85106205775&origin=inward.
- [239] I.J. Ong, J. Newman, J. Electrochem. Soc. 146 (1999) 4360. https://www.scopus.com/record/display.uri?eid=2-s2.0-0000280681&origin=inward.
- [240] M. Landstorfer, S. Funken, T. Jacob, PCCP 13 (2011) 12817–12825. https://
- pubs.rsc.org/en/content/articlelanding/2011/CP/c0cp02473b#!divAbstract. [241] H. Helmholtz, Annalen der Physik und Chemie 165 (1853) 211–233.
- [242] H. Helmholtz, Annalen der Physik und Chemie 243 (1879) 337-382.
- [243] M. Gouy, Journal de Physique Théorique et Appliquée 9 (1910) 457-468.
- [244] D.L. Chapman, Science 25 (1913) 475–481, https://doi.org/10.1080/ 14786440408634187.
- [245] Otto Stern, Zeitschrift für Elektrochemie und angewandte physikalische Chemie 30 (1924) 508–516. https://www.scopus.com/record/display.uri? eid=2-s2.0-25144442940&origin=inward.
- [246] D. Henderson, Prog. Surf. Sci. 13 (1983) 197–224. https:// www.sciencedirect.com/science/article/pii/0079681683900047.
- [247] S. Srinivasan, Fuel cells: From fundamentals to applications, Springer Science +Business Media. LLC. New York. 2006.
- [248] D. Danilov, R.A.H. Niessen, P.H.L. Notten, J. Electrochem. Soc. 158 (2011) A215.
- [249] G. Li, C.W. Monroe, Annual review of chemical and biomolecular engineering, 2020, 21.1–21.34.
- [250] F. Fasmin, R. Srinivasan, J. Electrochem. Soc. 164 (2017) H443–H455. https://iopscience.iop.org/article/10.1149/2.0391707jes.

- [251] X.-F. Zhang et al., PCCP 19 (2017) 9833–9842. https://pubs.rsc.org/en/content/articlelanding/2017/cp/c6cp08505a#!divAbstract.
- [252] J.R. Wilson, D.T. Schwartz, S.B. Adler, Electrochim. Acta 51 (2006) 1389–1402. https://www.sciencedirect.com/science/article/pii/S0013468605008017.
- [253] J.R. Wilson et al., Solid State Ionics 10 (2007) B81.
- [254] J.B. Bates et al., J. Electrochem. Soc. 147 (2000) 59–70. https://www.scopus.com/record/display.uri?eid=2-s2.0-0033903042&origin=inward.
- [255] A. Neumann et al., ACS Appl. Mater. Interfaces 12 (2020) 9277–9291, https://doi.org/10.1021/acsami.9b21404.
- [256] Y. Matsuda, N. Kuwata, J. Kawamura, Solid State Ionics 320 (2018) 38-44.
- [257] S.G. Marquis et al., J. Electrochem. Soc. 166 (2019) A3693–A3706. https://iopscience.iop.org/article/10.1149/2.0341915jes.
- [258] T.F. Fuller, M. Doyle, J. Newman, J. Electrochem. Soc. 141 (1994) 982. https://iopscience.iop.org/article/10.1149/1.2054868.
- [259] R. Xu et al., ACS Energy Lett. 4 (2019) 1073–1079, https://doi.org/10.1021/acsenergylett.9b00430.
- [260] M. Finsterbusch et al., ACS Appl. Mater. Interfaces 10 (2018) 22329–22339, https://doi.org/10.1021/acsami.8b06705.
- [261] F. An et al., Scientific reports 6 (2016) 35051. https://www.scopus.com/record/display.uri?eid=2-s2.0-85106257370&origin=inward.
- [262] S. Santhanagopalan, R.E. White, Int. J. Electrochemistry 2012 (2012) 1–10. https://www.scopus.com/record/display.uri?eid=2-s2.0-85106232469&origin=inward.
- [263] S. Ohno et al., ACS Energy Lett. 5 (2020) 910–915, https://doi.org/10.1021/acsenergylett.9b02764.
- [264] S.F. Gorman, T.S. Pathan, E. Kendrick, Philos Trans. Series A, Math., Phys. Eng. Sci. 377 (2019) 20180299. https://www.scopus.com/record/display.uri?eid=2-s2.0-85106271306&origin=inward.
- [265] B. Wu et al., Energy and AI 1 (2020). https://www.sciencedirect.com/science/ article/pii/S2666546820300161 100016.
- [266] W. Zaman et al., J. Mater. Chem. A 7 (2019) 23914–23921. https://pubs.rsc. org/en/content/articlelanding/2019/TA/C9TA05118J#!divAbstract.
- [267] N.J. Dudney, Y.-I. Jang, J. Power Sources 119–121 (2003) 300–304.
- [268] P.H.L. Notten et al., Adv. Mater. 19 (2007) 4564-4567.
- [269] L. Baggetto et al., Adv. Funct. Mater. 18 (2008) 1057-1066.
- [270] A. Sakuda, T. Takeuchi, H. Kobayashi, Solid State Ionics 285 (2016) 112–117. https://www.sciencedirect.com/science/article/pii/S0167273815003501.

- [271] D. Hlushkou et al., J. Power Sources 396 (2018) 363-370.
- [272] W. Zhang et al., ACS Appl. Mater. Interfaces 9 (2017) 17835-17845.
- [273] Y. Ito et al., J. Mater. Chem. A 5 (2017) 10658-10668.
- [274] A. Bertei, C. Nicolella, J. Power Sources 196 (2011) 9429–9436.
- [275] T. Drezen et al., J. Power Sources 174 (2007) 949–953.
- [276] N. Zhao et al., J. Alloy. Compd. 683 (2016) 123-132.
- [277] Y. Wang et al., Adv. Mater. 27 (2015) 3915-3920.
- [278] J. Yoshida et al., Journal of power sources 226 (2013) 122-126.
- [279] H. Tang et al., Chem. Mater. 30 (2018) 163-173.
- [280] Y. Wang et al., Nature Mater. 14 (2015) 1026-1031.
- [281] N.D. Lepley, N.A.W. Holzwarth, Phys. Rev. B 92 (2015) 214201.
- [282] S.P. Ong et al., Chem. Mater. 20 (2008) 1798–1807.
- [283] J.E. Saal et al., JOM 65 (2013) 1501-1509.
- [284] B. Liu et al., J. Mater. Chem. A 7 (2019) 19961–19969.
- [285] Z. Ahmad et al., ACS Central Sci. 4 (2018) 996-1006.
- [286] Z. Deng et al., Joule 4 (2020) 2017-2029.
- [287] S.T. Lee et al., Physical Review B 76 (2007) 115112.
- [288] L. Chen et al., Nano Energy 46 (2018) 176-184.
- [289] X. Zhang et al., J. Am. Chem. Soc. 139 (2017) 13779-13785.
- [290] M. Keller, A. Varzi, S. Passerini, J. Power Sources 392 (2018) 206–225.
- [291] H. Wang et al., Front. Energy Res. 7 (2019) 112.
- [292] X. Yang, J. Luo, X. Sun, Chem. Soc. Rev. 49 (2020) 2140–2195.
- [293] Y. Zhang et al., Solid State Ionics 305 (2017) 1-6.
- [294] Y. Hao et al., ACS Appl. Mater. Interfaces 9 (2017) 33735-33739.
- [295] S. Wang et al., ACS Energy Lett. 1 (2016) 1080-1085.
- [296] Pallab Barai, Aashutosh Mistry, Partha P. Mukherjee, Extreme Mech. Letters 9 (2016) 359–370.
- [297] X. Tao et al., Nano Lett. 17 (2017) 2967-2972.
- [298] X. Yu et al., Advanced Energy Materials 6 (2016) 1601392.
- [299] M. Weiss et al., Electrochem. Energy Rev. 3 (2020) 221-238.
- [300] S.P. Ong et al., Comput. Mater. Sci. 68 (2013) 314–319.
- [301] B. Zhang et al., Small 16 (2020) 1906374.
- [302] B. Zhang et al., ACS Appl. Mater. Interfaces 12 (2020) 6007-6014.
- [303] D. Chen et al., J. Mater. Chem. A 7 (2019) 1300-1306.
- [304] R. Xiao, H. Li, L. Chen, Sci. Rep. 5 (2015) 1-11.
- [305] C. Chen, Z. Lu, F. Ciucci, Sci. Rep. 7 (2017) 40769.
- [306] S. Yang et al., Matter (2020) 27-41.